

THESE POUR OBTENIR LE GRADE DE DOCTEUR DE L'ECOLE NATIONALE SUPERIEURE DE CHIMIE DE MONTPELLIER

En Chimie et physico-chimie des matériaux

Ecole Doctorale Science Chimie Balard

Unités de recherche IEM UMR 5635 et CIRIMAT UMR 5085

A fine physical chemical study of plasma polymerized organosilicon thin films for VOCs BTX selective gas sensing

Ghadi DAKROUB

Sous la direction de **Vincent ROUESSAC** et **Corinne LACAZE-DUFAURE**

Présentée le 25 novembre 2021 devant le jury composé de

Patrice RAYNAUD, Directeur de recherche, CNRS, LAPLACE, Toulouse	Rapporteur
Vincent JOUSSEAUME, Ingénieur de recherche, CEAtch-LETI, Grenoble	Rapporteur
Vincent ROUESSAC, Chargé de recherche, CNRS, IEM, Montpellier	Directeur de thèse
Corinne LACAZE-DUFAURE, Professeur d'université, ENSIACET, CIRIMAT, Toulouse	Co-directrice
Mikhael BECHELANY, Directeur de recherche, CNRS, IEM, Montpellier	Président
David FARRUSSENG, Directeur de recherche, CNRS, IRCELYON, Villeurbanne	Examineur
Stéphanie ROUALDES, Maître de conférence, Univ. de Montpellier, IEM, Montpellier	Co-encadrante
Thomas DUGUET, Chargé de recherche, CNRS	Co-encadrant



Table of content

Acknowledgments

General introduction

Chapter 1: Generalities

1 Volatiles organic compounds (VOCs)	7
2 Gas detection	11
2.1 Gas/solid interaction.....	11
2.1.1 Gas adsorption.....	11
2.1.2 Gas absorption and diffusion.....	18
2.2 Gas sensors 19	
2.2.1 Gas sensors types	19
2.2.2 Materials used for gravimetrical sensors.....	24
3 The PECVD for thin films preparation	27
3.1 The PECVD process principle	27
3.1.1 The definition of Plasma	27
3.1.2 The PECVD deposition mechanism.....	28
3.1.3 Plasma parameters influencing the deposition	30
4 Organosilicon materials.....	34
4.1 Conventional organosilicon polymers.....	34
4.2 Plasma polymerized organosilicons	35
4.2.1 HMDSO Plasma polymerization.....	36
4.2.2 Plasma polymerized HMDSO structure	38
4.2.3 The PP-HMDSO different applications	43
5 Theoretical section: DFT Calculations and XPS spectra simulation.....	46
5.1 The Schrödinger equation	46
5.2 Density Functional Theory.....	47
5.2.1 The Kohn-Sham approach.....	47

5.2.2 Approximation of <i>EXCp</i>	49
5.3 XPS spectra simulation	50
6 Conclusion.....	53

Chapter 2: Materials and methods

1 Sample preparation.....	56
1.1 Films deposition	56
1.2 Films thermal treatment	58
2 Characterization methods.....	59
2.1 Bulk characterization.....	59
2.1.1 Fourier Transform InfraRed spectroscopy	59
2.1.2 ²⁹ Si Solid- state Nuclear magnetic resonance	59
2.1.3 Energy dispersive X-ray spectroscopy	60
2.2 Surface characterization	61
2.2.1 X-ray photoelectron spectroscopy	61
2.2.2 Water Contact Angle	62
2.3 Physical properties	63
2.3.1 X-ray reflectometry analysis	63
2.3.2 Ellipsometry	64
2.4 Thermal properties	66
2.4.1 Thermogravimetric analysis	66
2.5 Sorption characterization.....	66
2.5.1 Ellipsometry coupled to sorption	66
2.5.2 QCM coupled to sorption.....	68
3 DFT computational details	70
4 Conclusion.....	71

Chapter 3: Comparative study of bulk and surface compositions of plasma polymerized organosilicon thin films

75

Chapter 4: Plasma polymerized organosilicon thin films for Volatile Organic Compounds (VOCs) detection

105

Chapter 5: Plasma polymerized organosilicon thin films for BTEX sensors applications	127
General conclusion.....	151
References	155

Acknowledgments

Here I am after three years, writing my last words in this manuscript. It was difficult for me to pack my things and leave behind the wonderful time I had with all of you. The wholesome of this report would not be possible without many contributors who helped me carry out my research. For those, I offer my acknowledgments:

First of all, I would like to express my sincere gratitude to the “Chimie Balard Cirimat” Carnot Institute for funding this project and for giving me the chance to pursue my education with this PhD degree.

I wish to acknowledge also the “Ecole Nationale Supérieure de Chimie de Montpellier” (ENSCM) that welcomed me during these three years of PhD.

This PhD thesis was done in collaboration between two laboratories: “Institut Européen des Membranes” (IEM) and “Centre Inter-universitaire de Recherche et d'Ingénierie des Matériaux” (CIRIMAT). I would like to express my special thanks to the two laboratories management for welcoming me and for providing me a great work environment during my PhD.

Certainly, I would like to thank Michael Bechelany, CNRS Senior Researcher at IEM, for chairing my PhD defence jury. Special thanks to Patrice Raynaud, CNRS Senior Researcher at LAPLACE-Toulouse and Vincent Jousseume, CEA Senior Researcher at Leti-Grenoble, for accepting to report and evaluate my PhD work. I wish also to thank David Farrusseng, CNRS Senior Researcher at IRCELYON-Villeurbanne, for examining my work.

I would like to express my deep gratitude to my two supervisors Vincent Rouessac (IEM) and Thomas Duguet (CIRIMAT) for the first 2 years, thanks to their consistent support, availability and guidance during these years, this project was accomplished. I wish also to express my thanks to Corinne Lacaze-Dufaure (CIRIMAT) who co-supervised me during my last year of PhD along with Vincent. Thank you for your support, availability and thoughtful advices. As well, I would like to thank my co-supervisor Stephanie Roualdes for her help and

support. Finally, I wish to point out that I learned a lot from all of you on both personal and scientific scales.

Special thanks to all of my colleagues and friends in IEM and CIRIMAT. Your presence made my journey delightful and I am glad to have met each one of you.

Warmest thanks to the one who always supported me and was there through thick and thin, Yara. I am beyond grateful for your presence by my side.

Finally yet importantly, I will always be indebted to the most important people in my life, my Family: Dad, Mom, my brother Jad and my sister Tala. You were the reason and the motivation behind this work. Thank you all for being always there for me.

General introduction

Air pollution is one of the most severe problems nowadays that threatens human health and environment. The air pollution is mainly a consequence of the uncontrolled pollutant emissions derived initially from human activities and/or natural resources [1,2]. Some of the major air and water pollutants are the volatile organic compounds (VOCs), specifically BTEX (Benzene, Toluene, Ethylbenzene and Xylene) vapours. These pollutants are well-known for their hazardous effects on environment and human health by causing harmful diseases such as cancer and mutagenic diseases [3]. These severe problems force some countries to restrict emissions of such vapours. For example, France in 2016 set a limit value of 0.6 ppb for benzene in public buildings [4]. All of these risks impose the necessity of fast and on-site BTEX sensors to increase the efficiency of air/water quality control and monitoring.

The most powerful technique used for BTEX detection is the gas chromatography (GC) which allows to detect BTEX vapours down to ppt levels. Nevertheless, the main problem of this technique is its huge size that limits its utilization to samples collecting and off-site analysis. Several other sensing techniques such as optical, electrical, and gravimetric techniques, using different materials (semi-conductors, zeolites, polymers...), have been tested for the detection of BTEX vapours. However, until nowadays there is lack of attempts to manufacture a BTEX portable sensor. For the fabrication of miniaturized gas sensors, one of the most competitive technology is the gravimetric sensing technique, requiring a functionalized thin film deposited on a quartz of a micro-balance to ensure the selectivity of the sensor.

Conventional organosilicon polymers are the best candidates for VOCs mainly BTEX gravimetric sensing applications due to their flexible Si-O-Si chain and their hydrophobic character [5–7]. However, the main problem of the conventional polymers is their large thickness that reduce their sensitivity. As an alternative, the plasma enhanced chemical vapour deposition (PECVD) is capable to elaborate thin, adherent and uniform polymer-like films on a flat support. This process is widely used in microelectronics [8], mechanics as anti-corrosion layers [9] and optics for the preparation of anti-reflection layers [10].

Accordingly, the objective of this thesis is to elaborate plasma organosilicon thin films for BTEX gravimetric sensing applications and to understand the BTEX sorption mechanisms and the organosilicons behavior towards the BTEX vapors.

The first chapter of this manuscript gives general notions on the different subjects covered in this thesis. As well, this chapter presents a state of the art related to the themes addressed in our study. In the first section, an overview on the VOCs is presented and specifically BTEX vapors. In the second section, models of gas/solid interactions are described as well as the gas sensing techniques and the materials used for gravimetric sensing. The third section concerns the plasma deposition process (PECVD), the deposition mechanism and the influencing parameters. In the fourth section, the organosilicon materials are presented focusing on the plasma organosilicons. As well, a state of the art concerning the application of plasma organosilicons in the fields of hydrocarbons gas sensing and permeation is given. Finally, in the last section of this chapter, a theoretical review on the DFT-based simulation of XPS spectra is presented as well as a state of the art concerning the attempts found in the literature to simulate BE energies shifts for polymers.

The second chapter of this thesis is devoted to the materials and methods used during this work. First, the characteristics of the PECVD reactor used for the preparation of materials are presented. Then, the characterization techniques used which concern the physicochemical characterizations and the sorption performances are presented as well as the DFT computational details.

The third chapter concerns the results presented in our first published article that deals with a fine investigation of the bulk and surface chemical composition of the plasma organosilicon materials function of the plasma energetic character. Also a comparison between the surface and bulk chemical composition is presented. In this study, several analytic techniques were used such as ^{29}Si quantitative solid state NMR to depict the bulk chemical composition. However, for the surface chemical composition investigation a special methodology was applied by combining experimental XPS and DFT calculations. This article has been submitted to *Surface and Interfaces*, reviewed, accepted and published (DOI: 10.1016/j.surfin.2021.101256).

In the fourth chapter, a second article is presented and describes the VOCs sorption performances of the synthesized organosilicon materials. The sorption study was performed using the quartz crystal microbalance (QCM) and function of the chemical composition as well the physical properties of the organosilicon films. This study aims to point out the ideal

organosilicon film for gas sensing applications. This article has been submitted to *Sensors and Actuators B: Chemical*.

The last chapter contains the third article which aims to improve the sorption performances of the chosen material after a thermal treatment in order to integrate an optimized organosilicon thin film in a BTEX gravimetric gas sensor. As well, this article investigates the sorption mechanism of the BTEX vapors into the organosilicon film using QCM and ellipsometry coupled to sorption. This article will be submitted before the PhD defense.

Chapter 1: Generalities

In this chapter, generalities over the main subjects involved in this PhD thesis will be presented. First, an overview on the VOCs specifically BTEX vapours and their contributions in air pollution will be presented in section 1.

Second, the theory behind the gas/solid interactions and the existing VOCs gas sensors will be presented in section 2. In the same section, a state of the art concerning the materials integrated in the BTEX sensors will be discussed.

In section 3, the plasma deposition process (PECVD) and its different parameters will be detailed.

Afterwards, organosilicon materials, and specifically plasma organosilicons, will be introduced in section 4 in terms of structure, chemical composition and applications. In this section, a state of the art concerning the integration of organosilicons in gas sorption applications will be argued.

Finally, the theoretical methods for XPS spectra simulation and approaches to simulate XPS core levels using quantum calculations presented in the literature will be discussed in section 5.

1 Volatiles organic compounds (VOCs)

In this section, an overview on the VOCs and more precisely BTEX vapours as well as their negative effects on environments and human health will be displayed bringing up the thesis problematic.

Air pollution becomes one of the most serious problems recently due to the uncontrolled pollutant emissions that are derived from different sectors such as industrial and transport sectors. This severe problem poses threats to health and climate by causing hazardous disease such as heart disease, chronic obstructive pulmonary disease, lung cancer and acute respiratory [1][11]. The world health organization (WHO) has estimated that every year, air pollution kills around seven million people worldwide [12]. Therefore, the detection of the pollutant gases becomes a serious task in large number of application fields. Table 1 illustrates the different applications fields that require toxic effluents detection [13].

Table 1: Examples of gas detection application fields that was illustrated in reference [13].

Application field	Function	Detected gases
Environment	Monitoring of toxic gases present in atmosphere due to industrial emissions	VOCs, CO, CH ₄ , CO ₂ , NO _x , SO _x , H ₂ S, NH ₃ , humidity
Home security	Toxic gas detection inside homes emitted by fires or explosions. Quality air control, kitchen control	VOCs, CO, CH ₄ , CO ₂ , humidity
Public security	Detection of dangerous pollutants. Indoor air quality control	Toxic gases, O ₂ , explosive gases
Motor/electrical engines	Control of the gas concentration in the motors in order to optimise the combustion cycle	CO, CO ₂ , NO _x , SO _x , H ₂ , hydrocarbons
Industries: <ul style="list-style-type: none"> – Petrochemical – Steel – Water treatment – Semi-conductors 	Air quality control, leaks detection	Hydrocarbons, O ₂ , O ₃ , CO, CO ₂ , H ₂ , H ₂ S, CH ₄ , Cl ₂ , HCl, AsH ₃ , BCl ₃ , PH ₃ , HF, H ₂ Cl ₂ Si, TEOS, C ₄ F ₆ , C ₅ F ₈ , GeH ₄ , NH ₃ , NO ₂

Well-known pollutants are the volatile organic compounds (VOCs). These compounds are carbon-based chemicals with high vapour pressure and low water solubility. They can easily propagate far from their emission area and can cause hazardous problems to human health and environment. The world health organization (WHO) classifies the organic volatile compounds into three groups:

- Very Volatile organic compounds (VVOCs)
- Volatile organic compounds (VOCs)
- Semi Volatile organic compounds (SVOCs)

This classification is based on the boiling point of each chemical. The lower boiling point corresponds to the higher volatility, which means the more the compound will be emitted into the air. The volatile organic compounds, (VOCs), such as toluene, ethanol or acetone are found in air and they are also strongly present in solids or liquids or on materials surfaces.

VOCs are emitted from solids or liquids as gases and can modify the chemical composition of the ambient air. They are naturally produced by forest fires for example, but mainly they are human-sourced. Several human activities are the origin of VOCs production such as engine combustion, the industrial sector or domestic products. For example, the manufacturing of paints and pharmaceuticals are responsible of VOCs emission. In addition, the chlorination in water treatment produces VOCs such as chloroform. VOCs are also present in petroleum fuels, hydraulic fluids, paints, cosmetic and dry cleaning agents [14,15]

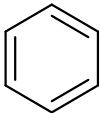
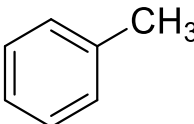
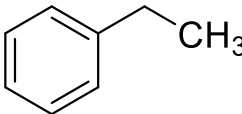
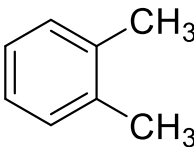
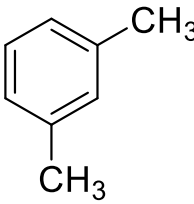
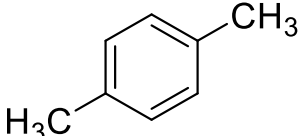
The EPA's Office of Research and Development's (Total Exposure Assessment Methodology (TEAM) study) found that the concentration of organic pollutants is two to five times higher inside homes than outside. Also, their study shows that the elevated concentrations of organic compounds remain for several hours after the activity in the inside air.

VOCs contain a large range of chemicals; some of them can provoke short- and long-term health problems. These toxic organic compounds cause harm diseases such as damage to the liver and central nervous system and skin/eyes irritation [16]. Besides, VOCs are known as environment pollutant due to their contribution in climate change and the ozone layer destruction [17].

Some of the most harmful VOCs vapours are the BTEX vapours: Benzene, Toluene, Ethylbenzene, and Xylenes. BTEX molecules shown in Table 2 belong to the aromatic hydrocarbons group. Their molecular structure is based on a particular ring possessing six carbon atoms denoted as benzene ring which is the simplest aromatic hydrocarbon molecule.

The other three BTEX compounds are benzene derivatives. They consist of a phenyl ring substituted by methyl or ethyl groups.

Table 2: BTEX chemical structure

Benzene		
Toluene		
Ethylbenzene		
Xylene	Ortho-xylene	
	Meta-xylene	
	Para-xylene	

Road traffic is one of the most important BTEX vapours source. In fact, BTEX mixtures are elaborated in oil industries to manufacture fuels for motor vehicles [14]. Toluene for example is added to fuels to improve their octane index which makes the engine more efficient and xylene is emitted by motor vehicles due to a reaction occurring inside the vehicle engine. In addition, BTEX vapours are emitted by industrial sectors such as pharmaceutical, cosmetics or paint industries. Besides, these vapours can be produced naturally from volcanoes and forest fires.

Table 3: Estimated intakes of BTEX by a person daily. All values are in $\mu\text{g/day}$. With ^a Assuming 5 cigarettes/d; ^b Assuming 2 L/d; and NA: Not applicable illustrated from [18]

	Benzene	Toluene	Ethylbenzene	Xylene
Air breathing	90 – 1300	2 – 12000	2 – 3600	70 – 2000
Cigarette smoking	1800	2000	40 ^a	Up to 190 ^a
Food	Up to 250	Up to 64	NA	NA
Drinking water	Up to 10 ^b	Up to 43	Up to 20 ^b	Up to 24 ^b

BTEX vapours are well-known for their high toxicity and for their carcinogenic effects [17,19]. They can threat human health by short-term risk such as respiratory disorders, allergic reactions, liver, kidneys and lungs diseases and long-term risks such as reproductive toxicity, carcinogen, decrease in the white blood cells, leukaemia and risk on the nervous system [20]. Several countries apply specifications for BTEX emission, for example, the Australian Drinking Water Guidelines (ADWG) specifies that the benzene concentration should not exceed 1 part per billion (ppb) in the drinking water. Similarly, the Environmental Protection (Air) Policy 2019 specifies that the objectives are to reduce the concentration of benzene to 3 ppb, toluene to 100 ppb and xylene to 200 ppb in ambient air to protect human health and environment.

All these risks provoked by the exposure to BTEX vapours imposes a real necessity to detect and monitor the emission of these pollutants to protect human and environmental health. In the following section, the most common gas/solid interactions phenomena will be mentioned in order to describe the detection processes of analytes such as VOCs.

2 Gas detection

This section is divided into two parts. First part presents generalities about the interaction between solid and gas. In this part, the sorption mechanism will be detailed. Furthermore, analytical models describing the gas adsorption on solids such as porous materials will be described. Finally, analytical models describing the dissolution of gas into polymers, which is the subject that concerns our work, will be pointed out.

In the second part, the different types of gas sensors will be presented focusing on the gravimetric gas sensors, which is the type used in this work. Afterwards, there will be a state of the art concerning the different materials used for VOCs gravimetric sensors, their advantages and limitations.

2.1 Gas/solid interaction

One of the main phenomena concerning the gas/solid interaction is the sorption of gas into solids such as porous materials or polymers. This process can be divided into three phenomena: gas adsorption on the solid surface, gas absorption and diffusion in the solid bulk. In this part, we will present these phenomena and explain the theoretical model behind each one in order to understand the gas (such as BTEX vapours) interactions with solids.

2.1.1 Gas adsorption

Adsorption is a surface-based process in which molecules (adsorbates) in a gas or a liquid are accumulated on the surface of a material (adsorbent) [21]. So, gas adsorption occurs when a solid surface is exposed to molecules in a gaseous phase. This phenomenon is usually defined by the increase of the gas concentration on the solid external surface [21]. The term adsorption indicates a surface phenomenon only, and it should not be confused with the term absorption that indicates the gas penetration into the mass of the solid. Generally, the adsorption phenomenon can be categorized as physical or chemical and in the following paragraph the difference between these two categories will be explained.

2.1.1.1 Physical and chemical adsorption

As mentioned above, the gas adsorption is usually divided in physical or chemical adsorption. In fact, when a gas is in contact with a solid surface, the interactions involved in the adsorption process allow distinguishing them.

The physical adsorption or “*physisorption*” results from weak physical interactions, such as van der Waals forces, between the gas molecules (adsorbate) and the solid (adsorbent

or substrate). Since, physical interactions in physisorption are similar to those responsible for vapour condensation, therefore this adsorption can be assimilated to the condensation of vapour into liquid [21].

The chemical sorption or “*chimisorption*” results from a chemical bonding between the solid and the adsorbed gas. In this process, the adsorbate and the adsorbent form covalent or ionic bonds that modify or strongly disturb their electronic structures [22,23]. Several criteria differentiate the physical and chemical sorptions [23–25]:

- The physical sorption is a phenomenon that occurs with any solid-gas without any chemical reaction. On the other hand, the chemical sorption occurs only if gas molecules and the solid atoms form strong bonds (covalent or ionic bonds).
- Physical sorption is reversible and the adsorbed molecules undergo a condensation phenomenon after sorption. The sorbed molecules can be easily desorbed using only a pumping system or coupled with a heating system. However, the desorption of chemically sorbed molecules is more complicated (energetically demanding) and sometimes this process can be irreversible which is the case for the desorption of oxygen from coal that produces CO and CO₂ instead of oxygen.
- Generally, the adsorption of a gas is an exothermic phenomenon. The heat emitted during a physical sorption is less than the heat emitted during a chemical sorption.
- Physical adsorption is faster than chemical adsorption. In addition, the physical adsorption usually leads to the formation of a multilayer on the surface, while chemical adsorption usually involves the formation of a monomolecular layer (monolayer) on the adsorbent surface (see Figure 1).

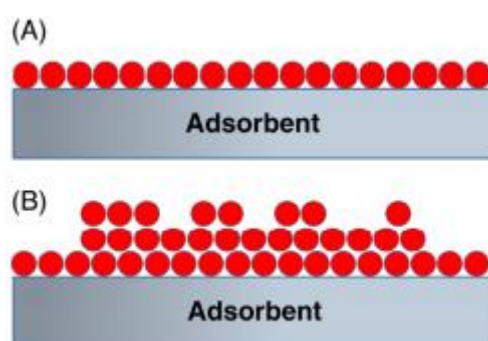


Figure 1: (A) Monolayer and (B) Multilayer adsorption (issued from [24])

One of the well-known solution to ameliorate the adsorption phenomenon on a material surface is to increase the specific area by introducing porosity in the material. This process will

be later tested in the last chapter. Meanwhile, in the following paragraph, the porosity term will be explained.

2.1.1.2 Porosity

The “specific area” term refers to the accessible surface per unit of mass of a material by the targeted molecules (measured in $\text{m}^2.\text{g}^{-1}$). The most used method for measuring this parameter is nitrogen or argon adsorption at 77 Kelvin. The measurement of this parameter using these techniques is difficult to carry out for thin films due to the necessity of an important mass quantity. Thus, the term porosity can be an alternative representation [13]; this parameter is defined as the ratio between the free volume and the solid volume present within the material. The size of the free volumes (also denoted pores) present in the material classifies the porous materials into three groups identified by the IUPAC:

- Microporous materials, for pore diameters less than 2 nm.
- Mesoporous materials, for pore diameters between 2 nm and 50 nm.
- Macroporous materials, for pore diameters greater than 50 nm.

The open porosity of the materials is usually deduced from graphs called “isotherms” that allows the identification of the pores size and shape. In the next paragraph we will present the most used adsorption isotherms.

2.1.1.3 Adsorption isotherms

An adsorption isotherm is the set of equilibrium states corresponding to the mass of adsorbed molecules as a function of the ratio between the equilibrium pressure P of the adsorbed gas to its saturated vapour pressure P_0 , at a constant temperature. This P/P_0 ratio is called the relative equilibrium pressure [26].

The adsorption isotherm shape leads to the characterization of the porous materials pores structure and size. In fact, such isotherm can give several information on the structure of the porosity of the material. Thus, six types of isotherms were identified by the IUPAC and are presented in Figure 2 [27,28].

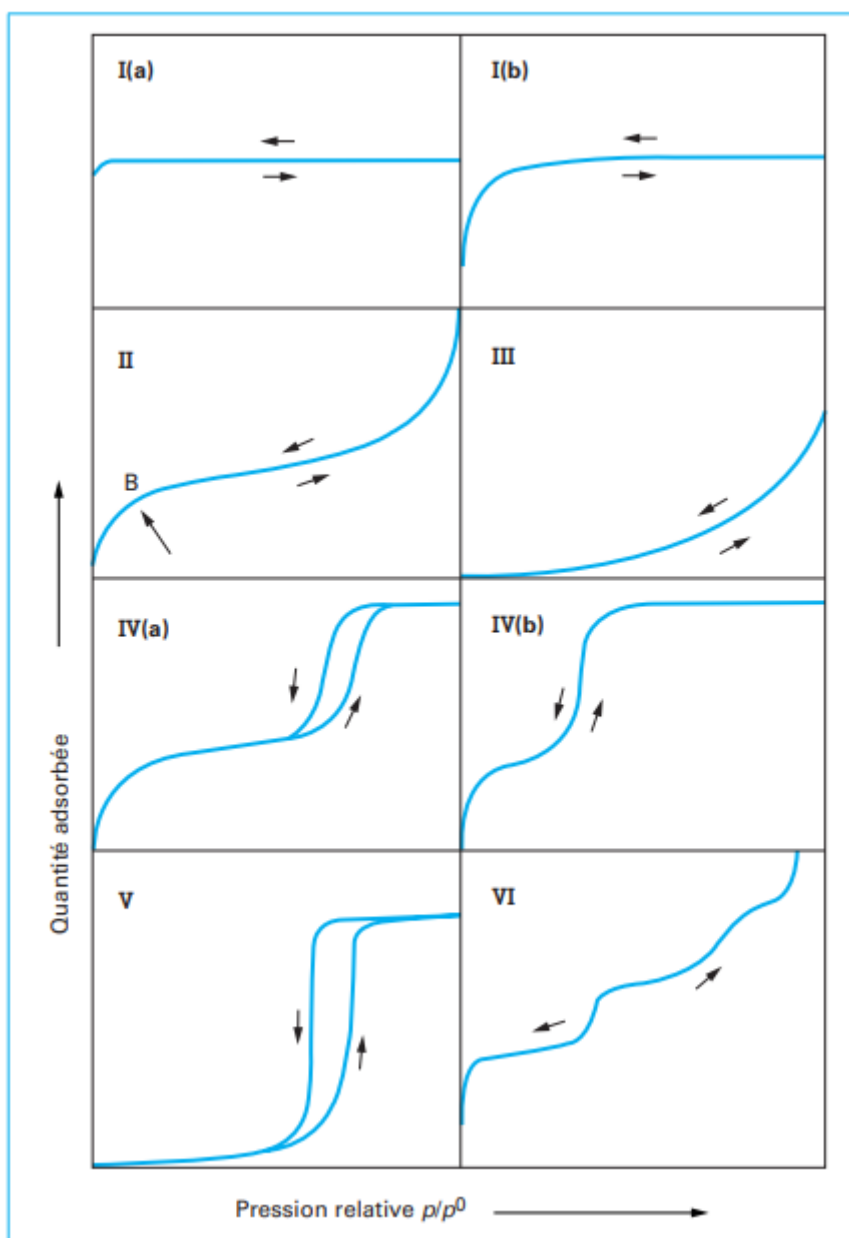


Figure 2: The six adsorption isotherms identified by the IUPAC illustrated from [28]

The I(a) and I(b) adsorption isotherm types are characterized by their strong rise and the existence of a plateau indicating the saturation of the adsorbent. These isotherms are obtained with adsorbents having only micro pores that are filled up at low pressures. Isotherm I(a) reveals an adsorbent with micropores lower than 1 nm width, while isotherm I(b) reveals a wider micropores size distribution [28]. The “type II” adsorption isotherm is characterized by a gradual increase of the adsorbed quantity. This isotherm is obtained with non-porous or macroporous adsorbents. The “type IV” adsorption isotherm is obtained with mesoporous adsorbents in which capillary condensation occurs. In the type IV (a) isotherm, the capillary condensation generates a hysteresis between the adsorption and desorption isotherms.

However, when the mesopores size is less than a critical value (depending on several parameters such as the adsorbate, the shape of the pores and the temperature), no hysteresis is observed and the adsorption isotherm is type IV(b). “Type III and V” adsorption isotherms are less frequent; they are characterized by a very slow increase of the adsorbed quantity due to the weak interactions between the adsorbent and the adsorbate. As an example, these types are observed in the adsorption of water vapour on a hydrophobic surface. The “type VI” adsorption isotherm is observed mainly in the adsorption on energetically homogenous surfaces where the adsorbed layers are formed gradually one after the other [28].

A large panel of analytic models was developed to describe the interactions between the surface of the adsorbents and the adsorbed molecule. In the following paragraph, we will introduce the most used ones for the characterization of the porous materials (specific area and pores size distribution).

2.1.1.4 Adsorption analytic models

Among the large number of surface adsorption models that are developed, Henry, Langmuir and Brunauer, Emmett and Teller (BET) models will be presented in this section.

The Henry Model

The Henry model is one of the simplest models for describing surface adsorption. It predicts a linear increase of the adsorbed gas quantity with the relative pressure of the adsorbed gas. Equation (1) reveals a linear relation representing the Henry regime with n being the quantity of the adsorbed gas, K_H is the constant of Henry and p is the relative pressure.

$$n = K_H p \quad (1)$$

This equation is valid as long as the concentration range considered is low enough. So, the adsorbed quantity in this case is generally weak. Therefore, the Henry model is not adequate to describe the adsorption isotherms presented in Figure 2. Indeed, this model cannot explain the curve of an isotherm nor the saturation phenomena. Other models have therefore been developed and will be discussed [29].

The Langmuir model

In 1932, Irving Langmuir proposed the Langmuir adsorption model [30]. Despite its simplicity, this model provides a first interpretation of the adsorption phenomena in equilibrium and under time depending conditions. In fact, the Langmuir model is the starting point for most of the approaches in surface chemistry [31]. In addition, the concept of monomolecular layer formation on a flat surface is attributed to Langmuir [32], who developed it from chemical

adsorption. Accordingly, Langmuir model does not take into consideration the existence of porosity or the physical sorption in the solid volume [33].

Langmuir considers that all the atoms on the surface of a solid can react chemically and independently with the adsorbed molecules. In fact, he considered that the molecules adsorption occurs on adsorption sites which are present on the surface and possess identical energy. Based on the kinetic theory of gases, Langmuir proposed his equation (equation (2)) indicating that the fraction of filled adsorption sites θ at a given temperature varies with the pressure of the gas phase P according to the relation:

$$\theta = \frac{bP}{(1 + bP)} = \frac{N_a}{N_s} \quad (2)$$

With N_a the number of adsorbed molecules, N_s the number of adsorption sites and b being a characteristic constant of the adsorbent / adsorbate studied couple and linked to the adsorption activation energy.

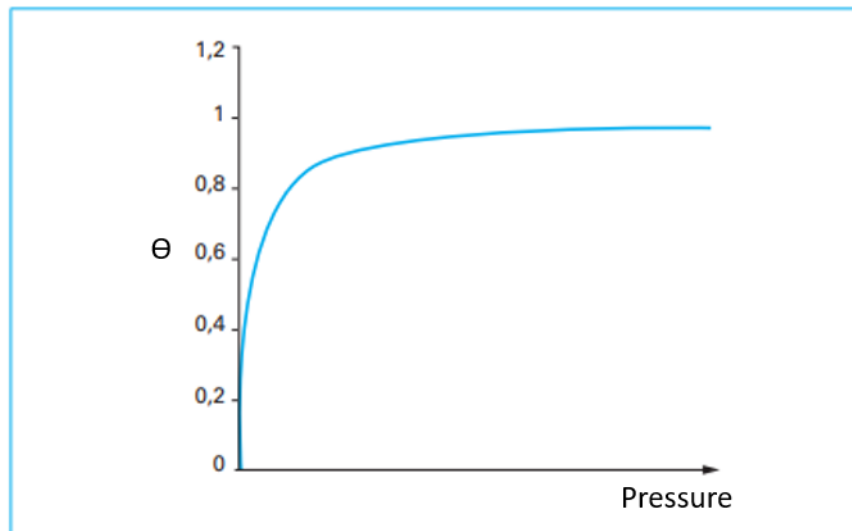


Figure 3: Langmuir adsorption isotherm issued from [34]

Figure 3 shows a graphical representation of the Langmuir isotherm in which θ varies as a function of the pressure P . This isotherm reveals that the adsorption phenomenon is complete ($\theta = 1$) at a certain pressure value. Beyond this value, it is considered that all the surface atoms are covered by a monomolecular layer and cannot be used anymore for a subsequent adsorption. This Langmuir isotherm should not be confused with a type I physical adsorption isotherm which looks the same but does not correspond to the same phenomenon.

The Brunauer, Emmett and Teller (BET) model

In 1938, Brunauer, Emmett and Teller [35] proposed an adsorption model based on Langmuir theory and allowed the description of the type II and type III physical adsorptions, characteristic of the multilayer adsorption. According to this model, the adsorbed molecules forming the first monolayer on the adsorbent surface can as well serve as adsorption sites for a next adsorbed monolayer, which allows the formation of many adsorbed layers as shown in Figure 4.

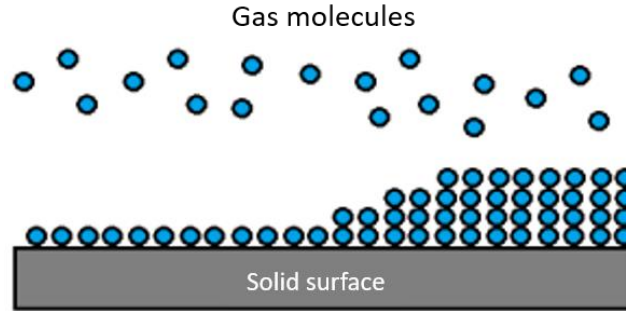


Figure 4: Multilayer adsorption scheme based on BET theory, illustrated from [13]

In addition to Langmuir's assumptions (only one type of independent adsorption site and absence of interactions between the adsorbed molecules), Brunauer, Emmett and Teller consider that from the second layer, the adsorption energy (E_2) is equal to the gas liquefaction energy (E_L). Furthermore, they considered that the adsorption takes place in a form of an infinite number of monolayers. Therefore, they proposed the following equation (3) relating the adsorbed quantity n_A to the relative pressure P/P_0 when the number of adsorbed layers tends to infinity:

$$\frac{n_A}{n_0} = \frac{C_{BET} \left(\frac{P}{P_0} \right)}{\left(1 - \frac{P}{P_0} \right) \left(1 - \frac{P}{P_0} + C_{BET} \left(\frac{P}{P_0} \right) \right)} \quad (3)$$

Where n_0 is the amount of adsorbed molecules quantity necessary to cover the surface of the adsorbent with a monomolecular layer while C_{BET} is a constant related to the difference between the adsorption and liquefaction energies of the gas.

The C_{BET} constant affects the shape of the BET produced isotherms. For example, a C_{BET} higher than 2 ($C_{BET} > 2$) generates a type II isotherm, while a C_{BET} between 0 and 2 ($0 < C_{BET} < 2$) produces a type III isotherm [36].

Besides the description of the analytes adsorption on porous surfaces, it is interesting to present the theory behind the interaction of analytes with polymers. In the next paragraph, we

will explain the theories that describe the absorption and diffusion of analytes into solids such as polymers.

2.1.2 Gas absorption and diffusion

The adsorption phenomena presented earlier are characteristic of the rigid porous solids that can adsorb molecules on the wall of the pores. However, flexible materials such as polymers are also characterized by gas absorption and diffusion into the material network. These phenomena present a great interest in our work because they describe the penetration of molecules into a polymer-type network such as that synthesized in this work.

Flory-Huggins theory

The Flory-Huggins theory proposes to calculate the contributions of some thermodynamic parameters, such as entropy and enthalpy, during the penetration of solvent molecules into a polymer [37,38]. In fact, the entropy parameter is linked to the disorder occurring in the polymer/gas mixture and the enthalpy parameter is linked to the polymer/solvent mixture heat.

The sum of the enthalpy and entropy parameters leads to the calculation of the Gibbs free energy change resulting from the mixing of the polymer and the solvent. Therefore, the Flory-Huggins equation which is derived from the free energy change is expressed by the following equation (4):

$$\ln(a) = \ln(\Phi) + (1 - \Phi) + \chi(1 - \Phi^2) \quad (4)$$

This equation relates the equilibrium fraction volume (Φ) of a gas probe into a polymer to the solvent activity (a) using the binary interaction parameter (χ). The χ parameter represents the affinity between the solvent and the polymer; a zero value (non-thermal mixture) signifies an ideal polymer / solvent mixture while an increase of the χ parameter indicates a lower affinity between the solvent and the polymer.

The Flory – Huggins equation does not take into account the elastic contribution to the free energy change due to the deformation of the polymer network. Thus, Flory – Rehner [38] modified the Flory – Huggins equation by adding an elastic energy term (Ω) in order to take into consideration the cross-linked networks. The elastic energy term (Ω) is expressed by equation (5):

$$\Omega = \left(1 - \frac{2M_c}{M}\right) \frac{V_s E}{3RT} \left(\frac{1}{\alpha} - \frac{1}{2\alpha^3}\right) \quad (5)$$

Where M_c is the average molecular weight of the polymer between the crosslinks in the polymer network, M is the polymer molecular weight, V_s is the solvent molar volume, R and T are the gas constant and the temperature respectively, E is the polymer Young's modulus and α is the swelling factor. This factor (α) is defined by t_{sp}/t_{dp} , t_{sp} and t_{dp} being the thicknesses of the swollen and dry polymers respectively.

This equation is used for the films deposited on substrates where the film swelling occurs only in the perpendicular direction to the substrate. The addition of the elastic term (Ω) is very important for the cross-linked films deposited on substrates and cannot be neglected due to the strong swelling rate of these films. In fact, since the swelling can only occur in one direction due to the presence of the substrate, the polymer network deformation is much stronger than in the case of a three dimensional swelling. This case will be pointed out during the BTEX sorption into the polymer network in the last chapter.

2.2 Gas sensors

In this second part of section 2, we will present a detailed description of the different gas sensors types, together with their advantages and disadvantages. In particular, we will focus on the gravimetric sensors that will be used during this work. In addition, in this part, we will present a state of the art concerning the materials involved in the gravimetric sensor. Note that a reduced state of the art concerning the gravimetric sensor materials is found also in the introduction of the second article (chapter 4 of this thesis manuscript).

2.2.1 Gas sensors types

In general, a detector that quantifies the presence of an analyte in the environment is composed of three principal elements [39]:

- A sensing element that will allow the detection (the elaborated material).
- A transducer element converting the recognition into a detectable signal (piezoelectric device, pH meter, electrode, photon counter....).
- A part dedicated for the signal treatment (amplifier and recorder).

The interaction between the sensing element (or recognition element) and molecules in its environment can induce a variation of its parameters such as enthalpy or mass, as it is the

case for a material exposed to a gas. Thus, these parameters modifications reflect the analyte/material interaction and confirm the presence of species on/into the material. The role of the transduction element is to transform this information into an interpretable and quantifiable signal that will be treated by the last element dedicated for signal treatment.

Consequently, a wide range of sensors based on different principles has been developed for gas detection. In order to classify the different sensors types, six general categories of sensors based on the transduction mechanisms have been suggested by the International Union for Pure and Applied Chemistry (IUPAC) [39]: optical sensors, electrochemical sensors, electrical sensors, calorimetric sensors, magnetic sensors and mass-sensitive (gravimetric) sensors.

2.2.1.1 *Electrochemical sensors*

The electrochemical gas sensors are based on the diffusion of the targeted gas through a porous membrane to an electrode where, electrochemical oxidation or reduction of the gas takes place at the surface of the working electrode [40,41]. Thus, the reaction produces a small current which is proportional to the concentration of the gas [42]. Electrochemical sensors are inexpensive and present a good sensitivity and selectivity. However, these sensors present major problems such as the volatility properties and the wide potential window of the aqueous electrolytes (AEs) in electrochemical sensors using (AEs) [43]. For electrochemical sensors using ionic liquids (ILs) electrolytes, and despite their great performance, the liquid leakage from the sensor and the slow gas diffusion caused by the liquid filling of the membrane pores limit their use [44]. In the case of electrochemical sensors using solid electrolytes (SEs), the high working temperatures needed for the oxidation reaction and the potential degradation of the electrolyte limit their use [45].

2.2.1.2 *Electrical sensors*

A wide range of electrical sensors are used for gas detection such as capacitance sensors, Schottky type barriers or the ones based on variation of the electrical conductivity which is the case of semiconducting metal oxide, metal, conducting polymer sensors [39]. One of the most used electrical sensor is the semiconducting metal oxide (SMO). These sensors detect species due to the oxidation and reduction reactions occurring between the metal oxide (MO) and the target gases. The gas of interest penetrates onto the active sensing MO, causing a change in the electrical resistance, from which the gas concentration can be determined [46]. SMO sensors are inexpensive compared to other sensing technologies, easily miniaturizable and robust.

However, this sensors type reveals serious problems such as poor selectivity, high sensitivity to humidity and high operational temperature [10,47,48].

2.2.1.3 *Calorimetric sensors*

Calorimetric sensors are based on the variation of the temperature generated by chemical reactions or by the thermal conductivity change in the presence of analytes. These evolutions are converted into electrical signals such as changes of the resistance, current and voltage. Calorimetric gas sensors are easy to manufacture [49], portable and show good selectivity for volatile hydrocarbons [50]. However, they might present a weak performance and inaccurate detection if a variation in the enthalpy occurs due to a change in the analyte concentration. In addition, these types of sensors require a high power consumption, elevated temperatures and are incapable to operate for a long-term.

2.2.1.4 *Magnetic sensors*

Magnetic sensors are based on changes in the paramagnetic properties of the gas being analyzed. Usually, these sensors are used to detect oxygen due to its high magnetic susceptibility compared to other gases such as nitrogen, helium, and argon [51,52].

2.2.1.5 *Optical sensors*

Optical sensors are based on detecting changes in visible light or in other electromagnetic waves resulting from its interaction with the analytes [39]. Measuring mechanisms such as fluorescence, emissions or absorption can be used to detect different gases depending on a defined optical wavelength [53]. One of the most common optical gas sensors is the infrared (IR) gas sensor, where the wavelength and the absorption intensity of mid-IR light are measured to identify the existent species [54].

Gas sensing using optical methods could achieve high sensitivity, selectivity and stability and their response time is relatively short. However, applications of optical sensors are restricted due their miniaturization difficulty and their high cost.

In this work, we used ellipsometry coupled with gas sorption which can be considered as a lab-scale optical sensor. The progressive introduction of a gas in the deposited layer by ad/absorption changes the reflected light polarization. Such analyses will be detailed in the materials and methods chapter and results will be presented in chapters 4 and 5.

2.2.1.6 *Mass sensitive or gravimetric sensors*

Gravimetric sensors are based on mass variations occurring at the surface of the sensor [55]. The mass variation is caused by the incorporation of molecules into a sensing layer

deposited on the mechanical resonator. This type of sensors is based on a piezoelectric material whose function is to assess the frequency characteristics of a resonating structure or a propagating acoustic wave caused by mass loading. Examples of mass sensitive sensors are shown in Figure 5. A wide variety of gravimetric sensors exist but the most known categories are:

- Volume wave acoustic sensors (BAW for Bulk Acoustic Wave).
- Surface wave acoustic sensors (SAW for Surface Acoustic Wave).
- Resonant Micro/Nano cantilever.

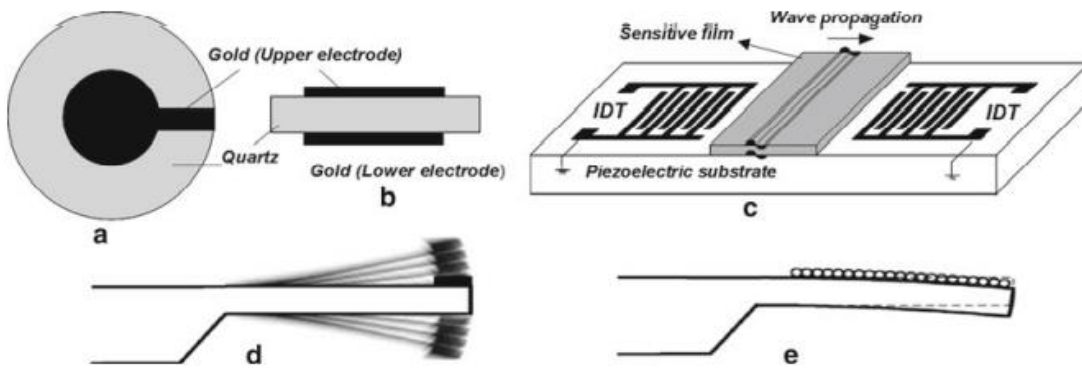


Figure 5: Schematic diagrams of mass-sensitive gas sensors: (a , b) quartz crystal microbalance (QCM) device; (c) surface acoustic wave (SAW) device; (d , e) microcantilever – (d) dynamic mode and (e) static mode. Illustrated from [39,56]

The BAW sensors such as the quartz crystal microbalance (QCM) or the film bulk acoustic resonator (FBAR) contain a piezoelectric material resonant between two metal electrodes. In this work we will focus on the QCM technic. The QCM setup is composed of a piezoelectric quartz crystal wafer coated with metal electrodes (gold) as represented in Figure 5a and 5b, a quartz wafer metal holder, an oscillator, a digital counter measuring the frequency changes, and a computer for data registration and plotting.

Basically, the detection is based on measuring the frequency shift of the resonant mechanical oscillator (Figure 6). This frequency shift Δf is directly related to the mass of the analytes sorbed on the surface of the microbalance and was interpreted by Sauerbrey (1959) with the following theoretical linear equation:

$$\Delta m = - \frac{\sqrt{\rho_q \mu_q}}{2f_0^2} S \Delta f \quad (6)$$

Where S is the surface of the electrode (in m^2), f_0 is the actuation frequency (Hz), ρ_q and μ_q are the density and the Young's modulus of the quartz respectively.

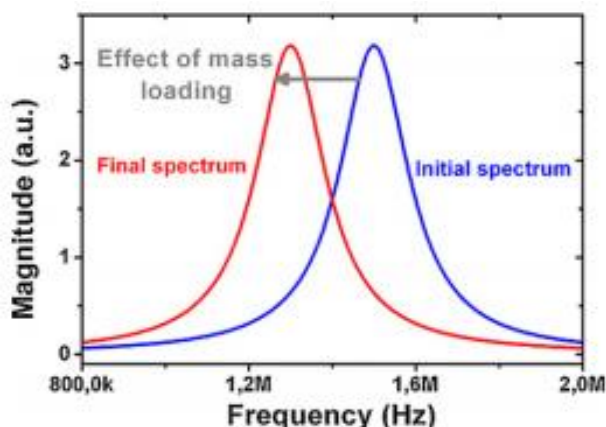


Figure 6: Principle of function of a gravimetric sensor based on frequency-shift measurement [55]

This relationship is valid for rigid and sufficiently thin films (in the sense that the frequency difference due to the deposited layer is negligible compared to the vibration frequency of the quartz). In addition, this result is the basis of QCM microgravimetry measurements in vacuum and air that can be used to detect chemicals such as volatile organic compounds (VOCs) based on the chemical layer deposited on the surface of the quartz [57].

The SAW devices also use piezoelectric crystal resonators to generate acoustic waves. These devices are more sensitive than BAWs and have a different structure, consisting of a piezoelectric substrate where two metal electrodes are deposited on its surface. An example of this geometry is represented in Figure 5c. An acoustic wave is generated by a metal electrode and then is propagated on the surface of the sensitive material. Once this acoustic wave reaches the other electrode, a potential difference appears and can be measured. The measurement of the propagated wave speed variation allows the determination of the adsorbed mass on the sensitive layer. The SAW sensor is sensitive towards any specific analyte depending on the coated chemical layer that can collect and distinguish between diverse molecules. It should be noted that the operation of the SAW and QCM sensors requires a temperature and humidity control because these parameters affect the QC resonant frequency shift during gas molecule collection.

Micro/nanocantilevers devices are another type of mass-sensitive sensors. These sensors can operate at higher resonance frequencies and both in dynamic and static conditions as shown in Figure 5d and Figure 5e. The micro/nanocantilever movement changes when a mass of analyte is adsorbed on its surface. In other words, when molecules adsorb on the micro/nanocantilever surface, they cause modifications in its frequency (dynamic mode) or changes in the stress at the surface that leads to an inclination of the micro/nanocantilever (static

mode). Micro/nanocantilevers have presented a significant importance in recent years due to their ability to measure very low adsorbed masses [55].

The gravimetric sensors are great candidates for the gas detection due to their high sensitivity, low cost and ability to be miniaturized. However, the most important drawback of these sensors is their lack of selectivity. In fact, the mass-sensitive sensors detect the mass change whatever the species. Therefore, there is a necessity of a chemical thin film deposited on the quartz crystal (in the case of QCMs) in order to insure the selectivity of these sensors. The QCM coupled to sorption will be one of the main techniques used for VOCs detection during this work. The analysis process will be detailed in chapter 2 dedicated to the materials and methods and the sorption results will be presented in chapters 4 and 5. Meanwhile, in the following section, we will be focusing on the materials that can be developed for the gravimetric detection of VOCs and especially BTEX.

2.2.2 Materials used for gravimetric sensors

As mentioned before, a gravimetric sensing device usually needs a chemical thin film to insure its selectivity and sensitivity [58]. A large number of materials have been developed for gravimetric sensing applications especially for VOCs. We can mention materials such as metal oxide nanostructures, zeolites, and polymers. In this section, a state of the art about the materials involved in the gravimetric sensing will be detailed in order to justify the chosen material elaborated for BTEX sensing.

2.2.2.1 *Metal oxide nanostructures*

Metal oxide have been widely studied for VOCs gas sensing especially in the manufacturing of semiconductor sensors type due to their low cost, high sensitivity, potential for miniaturization and operation simplicity [59–61]. However, there was numerous attempts to integrate metal oxide nanostructures in the gravimetric sensing of VOCs [62,63]. We can mention the recent work of Diltemiz et al. who elaborated nanofibers of copper(II) oxide and zinc oxide by electrospinning for formaldehyde detection using a QCM system; they succeeded to detect up to 41 ppb of analytes [64]. In the work of Xie et al., they used also zinc oxide but as nanospheres in order to detect methanol, ethanol, and isopropanol on their QCM device. The results show a better sensitivity for methanol and ethanol molecules compared to isopropanol molecules. According to Xie et al., this result is due to the position of hydroxyl in the molecules that makes easier the adsorption of methanol and ethanol molecules on the ZnO surface than isopropanol molecules [65].

Despite the cited advantages of metal oxide, the main inconvenient of such materials for BTEX sensing is their limited selectivity and their hydrophilic behaviour which reduces their performance in the presence of humidity imposing high temperature operation [66,67].

2.2.2.2 Zeolite

Zeolite materials are good candidates for the detection of VOCs gases due to their high specific area, non-toxic behaviour and high chemical and thermal stability. Several trials integrated zeolites materials in the gravimetric sensing and monitoring of humidity, NO, SO₂ as well as VOCs gases such as acetone, pentane and hexane [68]. In the work of Brosillon *et al.* the adsorption of an acetone/heptane gas mixture on a zeolite material was tested. The sensor showed a good selectivity and sensitivity towards acetone due to the polarity, volatility and boiling temperature differences between acetone and heptane [69]. Similarly, other works also used zeolites to detect dimethylmethylphosphonate (DMMP) gas with piezoelectric sensor devices (QCM). The results show high material sensitivity towards the targeted vapour and a detection limit up to 0.1 ppm [70].

Nevertheless, the integration of such materials in the gravimetric sensing applications of VOCs especially BTEX is complex due to the necessity of surface hydrophobicity tailoring for such materials and the need of high temperature application for desorption [70].

2.2.2.3 Polymers

Conventional polymers have been the most widely used materials for gravimetric sensing of VOCs, especially BTEX, due to their long flexible backbone chains and free volumes that ensure the penetration of large amounts of analytes into the polymer network. In addition, the flexibility of these polymer chains facilitates the desorption phenomenon, which means that the desorption mechanism can occur rapidly, easily and without any heating operations [71,72]. Furthermore, the possibility of modifying the molecular structure of polymers as well as their composition has made possible to study a large number of polymers with different functional groups. Beside thermal and chemical stability [73], many polymers exhibit good adhesion properties and can be deposited on many substrates. The most used polymers for the detection of VOCs are organic polymers and organosilicon polymers. Organic polymers such as poly(methyl methacrylate) (PMMA), polyisobutylene (PIB) and polybutadiene (PBD) has been used for the detection of VOCs such as toluene vapor (one of the BTEX) [74,75]. Organosilicon polymers such as polydimethylsiloxane (PDMS) were the earliest to be used in gravimetric sensors [76]. They are widely used for the detection of VOCs due to their hydrophobicity, which is important for the detection of non-polar molecules such as BTEX. In the work of Mirmohseni

et al., they used a PDMS layer casted on a quartz electrode in order to sense BTEX vapours using a QCM system [77]. Maute *et al.* coated a PDMS layer on silicon cantilevers to sense different vapour concentrations of n-octane, toluene and n-butanol. The coated cantilevers showed high sensitivities towards n-octane vapour compared to the cantilevers without polymer coating [78].

The application of polymers for the gravimetric sensing can face problems such as the thickness of the coated polymer or the high crosslinking degree. In fact, devices coated with conventional polymers can suffer from low sensitivity due to thick coated films [79]. In addition, for NEMS applications, deposits made without solvent are advantageous solutions because the capillarity forces present during the evaporation of the solvent can damage the nanobeams [5,6]. The choice of gravimetric detection imposes thus conditions on the films studied: they must be uniform, adherent and thin. Furthermore, the films should exhibit good chemical and physical stability.

The dry process deposition techniques can be a solution for the functionalization of gravimetric sensors. These techniques allow the synthesis of uniform films on a relatively large wafer, thin films of few nanometers, and most important, adherent films. Thus, these type of deposition processes answer the requirements of a sensing layer for gravimetric sensing applications. In the following section, we will detail the dry elaboration process technique used during this thesis, *i.e.* the plasma enhanced chemical vapour deposition (PECVD), its different characteristic parameters that influences the deposited materials and finally its application for the preparation of VOCs sensing materials.

3 The PECVD for thin films preparation

The Plasma Enhanced Chemical Vapour Deposition (PECVD) process is a well-known technique for the elaboration of thin, adherent and uniform films. This process will be used during this thesis to elaborate thin films for the VOCs gas sensing applications. In this section, the plasma deposition process will be detailed as well as the major parameters that influence the deposit.

3.1 The PECVD process principle

In order to understand the PECVD process principle, a general knowledge about the plasma (known also as the fourth state of matter) will be presented firstly.

3.1.1 The definition of Plasma

A plasma is a partially or fully ionized gas containing different species such as neutral, excited and / or ionized atoms / molecules, radicals, electrons and photons (Figure 7). Despite the presence of different charged species, this phase is electrically neutral due to the compensation of negative and positive charges. In order to create these different species in a gas, and therefore to create a plasma, it is necessary to supply a quantity of energy to a gaseous environment. In the laboratory, this energy can be supplied in the form of electrical energy. Under the effect of the electric field applied to the gas, the free electrons in the system can be accelerated. These electrons can collide with the species present in the gas creating excited species, neutral radicals due to the direct fragmentation of gaseous precursors, photons but also few ions. This phenomenon will repeat itself between the electrons, the species produced and the remaining molecules, enabling to maintain the plasma, appearing as a glow discharge [80].

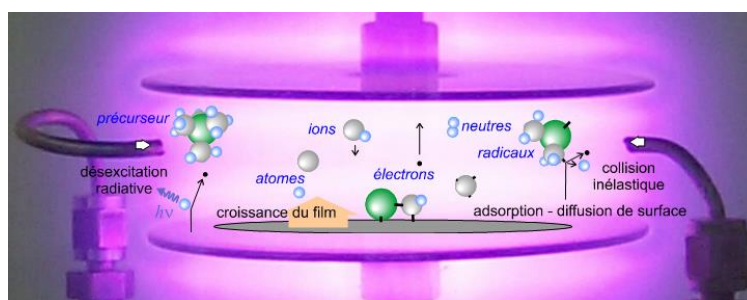


Figure 7: Scheme representing the different species in the plasma

Generally, the reactions occurring in the plasma phase can be divided into 3 categories:

- Primary reactions correspond to the first interactions between electrons and neutral molecules forming the gas phase such as ionization, dissociative ionization, excitation and dissociative attachment. These reactions are followed by reactions of de-excitation or dissociation.
- Secondary reactions correspond to the recombination between electrons and unstable species created during primary reactions such as electron-ion/ electron-excited molecules recombination.
- Reactions between heavy radicals.

Once all the species have been created, the system goes into a thermodynamic non equilibrium state. In fact, in this system, the electrons and heavy species are not at the same temperature due to the large difference in their mobility. Highly energetic primary electrons have a very high temperature ($> 10,000$ K) while neutral and ionic species maintain a temperature close to ambient (< 500 K); in this case, the glow discharge is called a cold plasma, being out of thermodynamic equilibrium as all the species are not at the same temperature.

The most abundant species in a cold plasma involving molecules are the radicals. These unstable species possess one or more unpaired electrons on their outer layers and therefore are very reactive. There are different reactions involving plasma radicals in contact with any surface such as chemical etching, grafting, crosslinking in case of polymer substrates [81–83] and film deposition. Whereas, non-condensable plasma phases favour etching, grafting and crosslinking, plasma phases issued from condensable molecules essentially induce film deposition, the other three phenomena becoming minor.

In this work, we will be interested in thin films deposition from condensable plasma discharge. Thus, in the next part, we will discuss how the plasma can be used to grow thin films on substrates.

3.1.2 The PECVD deposition mechanism

The PECVD process is based on the recombination and/or the adsorption of condensable radicals of the plasma on the surface of a substrate leading to the formation of a thin film. This deposition process will be used during this work and will be detailed hereafter.

Generally, a PECVD deposition involves only one of the two types of polymerization entitled plasma induced polymerization and plasma polymerization [84].

The plasma induced polymerization is close to the conventional polymerization. It is activated by radical species or electrons created in the plasma. These species react with

functional groups (double bond or ring) on the surface of a substrate and the reaction propagates to form a film.

The plasma polymerization is the reaction between different radicals created in the plasma, which react together to form the film. Usually, the material obtained is amorphous and highly crosslinked. In the frame of this thesis, only the plasma polymerization will be involved in the elaboration of plasma-deposited thin films.

The deposition mechanism shown in Figure 8 incorporates the main steps of plasma polymerization. Once the electrical energy (alternating voltage) is applied, electrons are accelerated, plasma is activated and radicals are created (2). The first step is the adsorption of the species at the surface of the substrate (3). Two types of adsorption are involved, either physisorption type (weak interactions such as Van der Waals), or chemisorption type (strong bonds between gaseous species and substrate). Then, the species diffuse (in the physisorption case) once adsorbed on the substrate surface (4). Depending on the rearrangement processes, the reactive species and their reaction products can either generate the film growing (5) and can induce the desorption of gaseous by-product fragments to the plasma phase (6). They can recombine in gas phase and be evacuated by the pumping system (7).

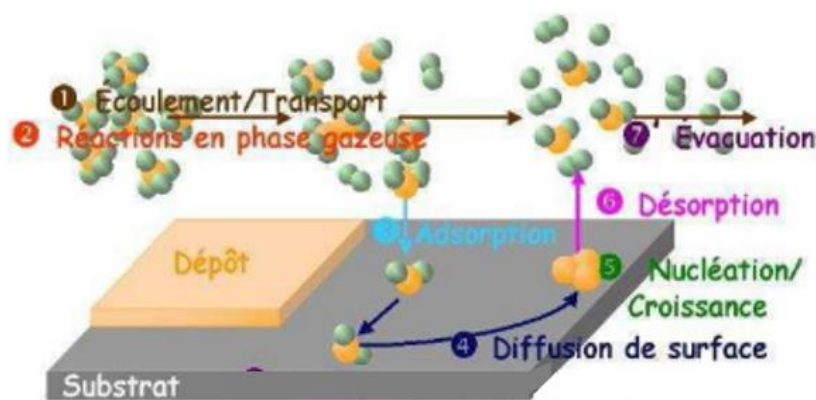


Figure 8: The plasma deposition mechanism issued from [85]

Accordingly, this deposition mechanism gives to the plasma polymerized films many advantages. As mentioned earlier, the PECVD deposition technique is able to elaborate thin (on a nanometer scale), uniform, without defects and tridimensional films on a relatively large substrate. In addition, the elaborated films are characterized by their very good adherence on different supports, whatever their chemical nature or surface topography may be. As well, the fact of randomly combining the species present in plasma gas phase generates a hybrid deposit that can be used for different applications. In addition to these characteristics, one of the most

important advantages of the plasma deposition is its versatility. In fact, depending on the application, the operating conditions of the PECVD process can be optimized to obtain the desired material. Thus, the many operating parameters, which can be adjusted, make it possible to obtain materials with different structures and compositions.

In the next section, we will present the different parameters that can be controlled during a PECVD deposition and their influence on the characteristics of the materials obtained.

3.1.3 Plasma parameters influencing the deposition

The PECVD differs from the thermal CVD by its versatility. In fact, the predominant parameters in the CVD are the nature of the precursors used, the temperature and the pressure conditions. However, the PECVD is also influenced by the plasma power and the plasma frequency. In this section, we will explain how each parameter can affect the chemical composition and the structure of the deposited materials.

3.1.3.1 *Reactor geometry*

The geometry of the reactor (precursor injection system, pumping system, shape and volume of the reactor, and position of the substrate) influences the transport parameters of the plasma species during the deposition process. This can modify the nature and the hydrodynamics of the active species, and therefore the deposition rate and the (micro) structure of the materials obtained.

3.1.3.2 *Substrate temperature*

One of the important advantages of the PECVD compared to the classical CVD is that the deposition can be occurred at room temperature. This fact made the PECVD compatible with any type of substrates. Nevertheless, the substrate temperature in a PECVD reactor can be controlled up to few hundreds degree Celsius affecting the deposited material structure. In fact, increasing the temperature of the substrate promotes surface mobility and desorption of species to the plasma phase. Thus, this temperature elevation causes a decrease in the film growth rate and an increase of the material crosslinking degree, or even the crystallization of the material (at temperature of several hundred °C).

3.1.3.3 *Plasma frequency*

The applied current frequency has a strong effect on the ionization of the gas phase. A low frequency leads to a high ionic energy and therefore the ionic bombardment of any surface in contact with the plasma phase is important. In this configuration, the etching phenomenon is

favoured. On the contrary, a high frequency leads to an increase in the number of electrons, thus there are more electron-molecule shocks leading to an improvement in the number of reactive species making film deposition the major phenomenon. Three frequency ranges can be considered:

- Low frequencies (LF) (<450 kHz)
- Radio frequencies (RF) (1 MHz - 0.5 GHz)
- Microwaves (MW) (~ 1 GHz and above)

During this thesis, we worked on a microwave MW-PECVD reactor (presented and detailed in the materials and methods section) to elaborate plasma polymerized thin films due to several reasons.

First of all, the fact of using microwave frequencies avoids any ionic bombardment in the plasma which reduces the probability of the film surface deterioration by the etching phenomenon [86]. The second advantage is that microwaves do not require the use of electrodes. In fact, the microwaves are distributed in the reactor using ECR (Electronic Cyclotronic Resonance) applicators and they transmit their energy directly to the electrons in the vapor phase. Furthermore, the MW-PECVD allows higher deposition rates comparing to other frequencies, which highly reduces the deposition time [87]. Finally, the MW-PECVD process allows the deposition of homogeneous layers on substrates of large dimensions [88]. Indeed, the absence of electrodes in the MW-PECVD enlarge the plasma area which is no more limited by the size of the electrodes but by the number and lattice of the MW applicators. Also the efficiency of a MW-PECVD process is better than the efficiency of a lower frequency PECVD process as the electronic density is higher, thus the growth rate of the deposited film is higher even if the working pressure is much lower, which induces a lower consumption of the precursors. These last points make the MW-PECVD a very attractive deposition technique for the industries.

3.1.3.4 Plasma power

The enhancement of the plasma electrical power favours the increase of the dissociation degree of the species. Thus, a limitation of the reaction is observed by the reactive species created at low power. However, at high plasma power, the reaction is limited by the transport of the active species.

3.1.3.5 Precursors

Identically to the thermal CVD, many precursors can be chosen in a PECVD process. They must be volatile under the pressure and temperature conditions chosen for the synthesis. Gaseous precursors and liquid precursors with a high vapour pressure (several mbar) at ambient temperature can be easily vaporized under the only effect of vacuum in the deposition chamber. But liquid precursors with relative low vapour pressure should be heated up or/and pushed/lead thanks to a pusher/carrier gas. In case of heated precursor, the feed tube should be also heated up to maintain the vapour state of the precursor up to the PECVD chamber. For carrier or dilution purpose, some gas or mixture of gases (Ar, He, N₂...) can eventually be mixed with the precursor(s) vapours in the deposition chamber. The variety of obtained materials is all the larger than the composition of the plasma gaseous phase is complex.

3.1.3.6 Pressure

The pressure in the deposition chamber is linked to the precursors flux and the pumping strength since it depends on the balance between the incoming flows (flow rates of precursors, micro-leaks...) and the outgoing flows (pumping flow rates). In general, at the same plasma power density, lower pressure slows down the reactions in the gas phase and increases ion bombardment at the surface of the substrate, which reduces the deposition rate. On the contrary, higher pressure leads to a high growth rate of the film but can even also lead to the formation of powder in the gas phase if excessively high. Usually, the pressure for a PECVD process is in the range of 10^{-3} - 1 mbar in order to control the formation of the deposit. In a MW plasma the high electronic density generates an important monomer fragmentation which leads to high film growth rate at lower pressures ($\approx 10^{-3} - 10^{-2}$ mbar).

3.1.3.7 Yasuda parameter $W/F.M$

The deposit structure depends strongly on the fragmentation of the precursor which is dependent on all the experimental parameters described above. In order to simplify the conditions of synthesis, Yasuda proposed an empirical parameter [89]. The Yasuda parameter corresponds to the energy supplied to the plasma related to the mass of the precursor. It is expressed by the ratio $W / (F.M)$, where W is the power supplied to maintain the plasma, F the precursor flux and M the molar mass of the precursor. So, this parameter allows the differentiation of the plasma energetic behaviour:

- For low $W / F.M$, the energy is low compared to the injected mass of the precursor which is weakly fragmented and therefore the deposited film conserves the chemical

patterns present in the precursor. In this case, the plasma is called soft plasma and the precursor polymerization phenomena is close to the conventional polymerization.

- Conversely, for a high $W / F.M$, there is a precursor deficit and/or an energy exceed. The molecules present in the plasma are strongly fragmented and the deposit is denser, and more inorganic. In this case, we are talking about hard plasma conditions.

As shown in this section, the versatility of the PECVD technique makes it possible to prepare various materials in terms of their composition and their (micro) structure. Among the wide range of materials that can be elaborated by PECVD, in this work, the PECVD was used to deposit plasma organosilicon materials.

In the following section, the organosilicon materials will be introduced as well as their structure and applications fields. In addition, the choice of this material for gas sensing application mainly BTEX vapours will be justified.

4 Organosilicon materials

In this section, an overview on the organosilicon materials will be presented with a focus on the plasma organosilicon materials. Characterization results issued from the literature will be very briefly summarized to give a global idea on the plasma organosilicon material structure. Indeed, a more detailed state of the art concerning the plasma organosilicon chemical composition would be found in chapter 3 (introduction of the first article). Finally, the different application fields and a state of the art concerning the introduction of plasma organosilicons in gas sensing applications will be presented.

4.1 Conventional organosilicon polymers

Organosilicon materials have a chemical structure composed of silicon and carbon atoms. In the case of supplementary oxygen atoms, silicon and oxygen atoms can be bonded together to form siloxane bonds. In the case of the well-known PDMS polymer (shown in Figure 9) whose main chain is a siloxane one, each silicon atom is also bonded to two CH₃ (methyl) groups to form the dimethylsiloxane unit [SiO(CH₃)₂].

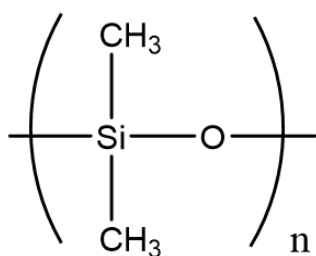


Figure 9: Dimethylsiloxane monomer

In the PDMS, the covalent bond created between the silicon and the oxygen is extremely stable due to its high large bond energy (452 kJ/mol). In addition, the wide Si-O-Si bond angle ($\approx 143^\circ$) and the high Si-O bond length ($\approx 1.63 \text{ \AA}$) give the PDMS chain good flexibility and mobility. Furthermore, the presence of free volumes in siloxane-type polymers (compared to hydrocarbon polymers) explains their high solubility and high gas diffusion coefficients [90]. As mentioned before, these polymers are also hydrophobic due to the presence of methyl groups pointing to the outside (Figure 9). Because of all these advantages, the organosilicon materials (and especially organosiloxane ones) are widely used in different applications and specifically in the sorption and detection of VOCs such as BTEX.

Organosilicon polymers are usually polymerized conventionally by using a 3 steps synthesis: the chlorosilane synthesis, the chlorosilane hydrolysis and finally ring opening polymerization or polycondensation (more details can be found in [90]). However, as mentioned before the conventional polymers are not totally adequate for gravimetric sensing applications. Thus, other polymerization techniques such as plasma polymerization of organosilicon precursors could be a suitable solution. The next part will focus on the plasma organosilicons, which will be the materials used in this work.

4.2 Plasma polymerized organosilicons

Thanks to the versatility of the PECVD technique, a wide range of organosilicon materials could be elaborated. In fact, by varying the plasma parameters and the organosilicon precursor, the PECVD technique is capable to elaborate various organosiloxane films ($\text{SiO}_x\text{C}_y\text{H}_z$) ranging from polymer-like materials (close to conventional PDMS) to inorganic SiO_2 -like materials [91]. Thus, most of the work done on plasma polysiloxane-type materials investigates the process parameters influence on the deposit structure. To sum up, most important parameters influencing the chemical structure are the Yasuda parameter (W/F.M) and the addition of a gas to the monomer flow.

The Yasuda Parameter:

The Yasuda parameter represents the energetic character of the plasma. As already presented before, the increase of W/F.M induces the increase of the organosilicon monomer fragmentation, therefore the deposit is affected by:

- Loss of the organic character due the cleavage of Si-CH₃ bonds.
- Formation of Si-CH₂-Si bonds leading to a more crosslinked network.
- Densification of the material.

The Mixture of gas/monomer:

A large number of studies have mixed organosilicon monomers with dioxygen, for the elaboration of silica SiO_2 films. The addition of O_2 enhances the fragmentation of the monomer and favours the elimination of organic groups by forming inorganic Si-O-Si chains [92,93].

Other studies have mixed organosilicon monomers with other gases such as argon, helium, or nitrogen. However, the addition of argon or helium does not affect strongly the chemical structure of the deposit. In fact, it can enhance the molecule-ion bombardment leading to a slight elimination of organic groups and increasing the films density [94,95]. On the other

hand, the addition of N_2 or NH_3 has not only the effect of eliminating the organic groups, but it leads to the formation of polysilazane films by creating nitrogen bridges between the Si atoms.

In this study, the PECVD deposition was carried out only with the monomer flow without any mixing gas. The next paragraph will present the different precursors used in the literature for the elaboration of plasma organosilicons.

Organosilicon precursors

Various linear or cyclic organosilicon precursors have been utilized in the synthesis of $SiO_xC_yH_z$ films by PECVD such as Tetramethyldisiloxane (TMDSO), Tetramethylsilane (TMS) or hexamethylcyclotrisiloxane (D3). In this work, the precursor used for the elaboration of $SiOCH$ thin films is the hexamethyldisiloxane (HMDSO) shown in Figure 10. This monomer has been chosen due to its high vapour pressure, which facilitates its injection into the PECVD enclosure, its high deposition rate, accessibility, safety compared to silanes and low cost. In addition, the HMDSO monomer has been widely tested for the elaboration of hydrophobic films (under specific plasma conditions), close to PDMS (PDMS-like) in the literature [96–98]. Accordingly, this precursor can lead to the elaboration of adherent, thin, hydrophobic PDMS-like films for BTEX sensing applications [99–101].

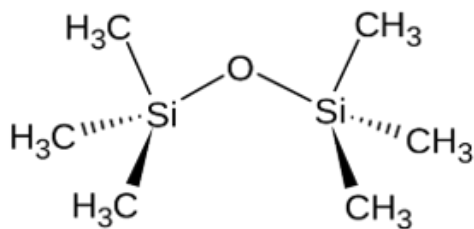


Figure 10: HMDSO monomer

For all the reasons mentioned above, the HMDSO will be the precursor used for the elaboration of plasma polymers in this work. In the next section, the mechanism of the HMDSO polymerization will be presented.

4.2.1 HMDSO Plasma polymerization

Gas phase analysis is very useful to determine the mechanism of the HMDSO plasma polymerization. This analysis provides interesting information on the fragmentation process of the monomer. Several studies have analysed the gas phase of pure HMDSO (or mixed with argon or oxygen) using mass spectrometry (MS) [102–104], Optical Emission Spectroscopy (OES) [105] or FTIR absorption spectroscopy [106]. The most abundant chemical species present in the gas phase of an HMDSO plasma are listed in Table 4.

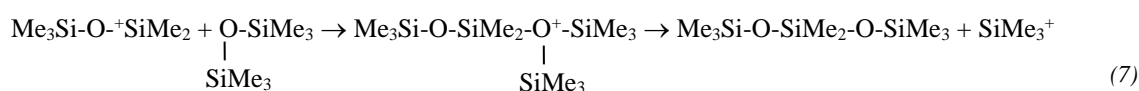
Table 4: Chemical species identified in the HMDSO plasma gas phase [102–106]

Composite type	Chemical species
Inorganic species	H ₂ , ArH
Hydrocarbons	CH, CH ₂ , CH ₃ , CH ₄ C ₂ H, C ₂ H ₂ , C ₂ H ₃ , C ₂ H ₄ , C ₂ H ₅ , C ₂ H ₆ C ₃ H ₂ , C ₃ H ₃ , C ₃ H ₄ , C ₃ H ₅ , C ₃ H ₆ , C ₃ H ₇ , C ₃ H ₈
Methylsilanes	H ₂ SiMe HSiMe ₂ SiMe ₃
Siloxanes composite	Me ₃ SiOSiHMe, Me ₃ SiOSiMe ₂ , Me ₃ SiO

The species identified in the gas phase result from the dissociation of the monomer (HMDSO) due to electronic impact, formed radicals ionization reactions and secondary reactions occurring between ion-molecule, ion-radical and radical-molecule. So, these radicals and ions produced in the plasma by fragmentation initiate the polymerization reactions.

The analysis of the gas phase shows that the main fragmentation reaction of the HMDSO monomer is the abstraction of methyl groups especially at low plasma energy. However, the plasma polymerized HMDSO (PP-HMDSO) deposit contains small organosilicon oligomers [104,106] and the structure of these oligomers indicates that their formation is initiated by the breaking of the Si-O bond in the monomer molecule.

Briefly, the HMDSO plasma polymerization process consists of the extension of the HMDSO molecule by one dimethylsiloxane unit according to the following equation (7)[95]:



We should mention that, the gas phase of organosilicon monomers mentioned the presence of reactive silicon-carbon double bonds groups (Si=CH₂) leading to the formation of some Si-CH₂-Si or Si-CH₂-CH_x bridges. Besides, the presence of the CH₂ groups in the gas phase [106] also could lead to the formation of some Si-CH₂ bridges. A detailed plasma polymerization mechanism of HMDSO monomer can be found in the paper of Alexander *et al.* [103,104].

After presenting the organosilicon plasma gas phase composition and the HMDSO plasma polymerization mechanism, the next section will be dedicated to the PP-HMDSO chemical structure based on a sum up of the results found in the literature.

4.2.2 Plasma polymerized HMDSO structure

The plasma polymerization produces small amounts of deposited material (a few mg). In addition, the polymer produced is generally insoluble in organic solvents due to its high degree of crosslinking. Therefore, the characterization of the plasma materials by analytical methods generally used for conventional polymers is complicated. However, the chemical composition and structure of plasma polysiloxane materials are mainly characterized by powerful techniques such as: infrared absorption spectroscopy (FTIR), AUGER electron spectroscopy (AES) and X-ray photoelectron spectroscopy (XPS), elemental analysis (AE), solid state nuclear magnetic resonance (NMR), gas chromatography combined to mass spectrometry (GC/MS) analysis. Other analyses such as water contact angle measurement (WCA), scanning electron microscopy (SEM), ellipsometry are also widely used for the characterization of plasma films. In this section, we will present some results of the organosilicons chemical composition found in the literature; we will focus on the FTIR, ^{29}Si solid state NMR and XPS techniques in order to depict the bulk and surface chemical composition. Then, physical properties results will also be presented such as density, refractive index and wettability. This summary is completed by a more detailed state of the art in the chapter 3 (introduction of first article).

4.2.2.1 *FTIR analysis*

The different IR absorption bands of the plasma polysiloxanes are presented in Table 5. Some of the bonds present in the polymers are also shown in the FTIR spectra of the HMDSO monomer. Nevertheless, new bonds are also formed during the plasma polymerization, such as Si-OH, Si-H, Si-(CH₂)_x-Si and Si-O-C. The absorption bands of the plasma organosilicons spectra are generally wider than those of the monomer; this indicates the presence of various compounds (compared to the monomer) and the high crosslinking degree of the plasma materials.

Table 5: Infrared absorption band of plasma organosilicons with ν : mode stretching, δ : mode bending, ρ : mode rocking, s : symmetric, a : asymmetric and s : strong, m : medium, v : variable [92,95,106–108]

Groups nature	Position Wavenumber (cm ⁻¹)	Vibration mode	
Alkyl groups			
CH ₃	2960 2900	$\nu^a(\text{C-H})$ $\nu^s(\text{C-H})$	s-m m
CH ₂	2925 2855	$\nu^a(\text{C-H})$ $\nu^s(\text{C-H})$	s-m m
Si-CH₂ groups			
Si-CH ₂ -CH ₂ -Si	1400	$\delta(\text{CH}_2)$	
Si-CH ₂ -Si	1360	$\delta(\text{CH}_2)$	
Si-CH₃ groups			
Si-Me _x	1410	$\delta^a(\text{CH}_3)$	
Si-Me _x	1260	$\delta^s(\text{CH}_3)$	s-m
Si-Me ₃	845	$\rho(\text{CH}_3) / \nu(\text{Si-C})$	v
Si-Me ₃	760	$\rho(\text{CH}_3) / \nu(\text{Si-C})$	v
Si-Me ₂	885	$\rho(\text{CH}_3) / \nu(\text{Si-C})$	v
Si-Me ₂	805	$\rho(\text{CH}_3) / \nu(\text{Si-C})$	v
Si-Me	775	$\rho(\text{CH}_3) / \nu(\text{Si-C})$	v
Si-H groups			
R-SiH ₂ -R	2138-2117	$\nu(\text{Si-H})$	s
H-SiR ₃	2110-2094	$\nu(\text{Si-H})$	s
H-SiR ₃	842-800	$\delta^s(\text{Si-H})$	s
OH groups			
OH in Si-OH	3650	$\nu(\text{O-H})$	m
OH in Si-OH	3400	$\nu(\text{O-H})$	m
Si-OH	930	$\nu(\text{Si-O})$	s
Si-O-Si groups			
Si-O-Si	1150-1100	$\nu^a(\text{Si-O-Si})$	vs
Linear siloxane chains	1093-1076 et 1055-		vs
cyclotrisiloxanes	1024		vs
other cyclosiloxanes	1020-1010		
Si-O-Si	1100-1050 810-800	$\delta(\text{Si-O-Si})$	m
Si-O-C groups			
Si-O-CH ₃	1100-1075 850-800	$\nu^a(\text{Si-O-C})$ $\nu^s(\text{Si-O-C})$	vs s-m

4.2.2.2 Solid-state NMR analysis

NMR analysis is the technique that provides the most detailed information on the molecular structure of plasma polymers. This powerful technique investigates the bulk chemical composition of the plasma organosilicons. However, only few works present in the literature deal with this technique because it requires a large amount of materials (about 400 mg for the quantitative solid state NMR) and most PECVD reactors find difficulties to produce this amount under normal conditions. The environments detected in siloxanes by ^{29}Si solid state NMR are $\text{SiO}(\text{CH}_3)_3$, $\text{SiO}_2(\text{CH}_3)_2$, $\text{SiO}_3(\text{CH}_3)$ and SiO_4 denoted as M, D, T and Q respectively (Table 6). These environments are located in chemical shifts range between +10 and -110 ppm. Other compounds derived from initial ones (M, D, T and Q) can be detected in the NMR spectra due to substitution of methyl groups by hydrogen or hydroxyl groups. We should mention also that another compound that can also be found in the bulk composition of plasma organosilicons is the $\text{Si}(\text{CH}_2)(\text{CH}_3)_3$.

Table 6: The different environments detected in the NMR solid state spectra of plasma organosilicons (illustrated from [95,109–111])

Resonance type	Environments	shift (ppm)
^{29}Si	$\text{Si}(\text{CH}_2)(\text{CH}_3)_3$	0
	M : $\text{O}-\text{Si}(\text{CH}_3)_3$	9
	M^{H} : $\text{O}-\text{SiH}(\text{CH}_3)_2$	-5
	D : $(-\text{O}-)_2\text{Si}(\text{CH}_3)_2$	-9 and -18
	D^{H} : $(-\text{O}-)_2\text{SiH}(\text{CH}_3)$	-35
	T : $(-\text{O}-)_3\text{SiCH}_3$	-47 to -77
	Q : $(-\text{O}-)_4\text{Si}$	-84 to -110
^{13}C	$(\text{CH}_3)_3-(\text{Si})-\text{O}-$	-3
	$(\text{CH}_3)_2-(\text{Si})-(\text{O})_2$	1
	$\text{C}-(\text{C})$	17.5
	$\text{O}-\text{CH}_3$ (methoxy)	40

4.2.2.3 XPS analysis

The XPS analysis is one of the most powerful techniques for the characterization of the surface chemical composition. This quantitative technique allows the determination of the different environments present on the surface of the material by the decomposition of the Si 2p core level. However, the decomposition of the Si 2p peak of plasma organosilicons materials is complex and due to the various environments present on the surface. Usually, the Si 2p core level of PP-HMDSO is decomposed into four environments denoted as M, D, T and Q (similar

to the environment shown in the NMR paragraph) [92,107,112–114]. The binding energy of these environments increases when a methyl group is replaced by an oxygen atom. However, Roualdes et al. [113] added a fifth component in the decomposition of the Si 2p spectra of a plasma organosilicon elaborated in soft conditions. This supplementary environment is attributed to SiC₄, i.e. a SiC₃ termination group bonded to a methylene bridge Si(CH₃)₃(CH₂). Table 7 represents the different Si environments found on the PP-HMDSO surface and their binding energies illustrated from the literature (a more precise state of the art on the Si 2p core level decomposition is presented in chapter 3).

Table 7: The different environments detected on the surface of organosilicon materials [92,98,107,112,114]

Core level	Environments	Binding energy (eV)
Si2p	SiC ₄	99,5
	SiOC ₃ (M)	101.5 - 101.6
	SiO ₂ C ₂ (D)	101,9 – 102.1
	SiO ₃ C (T)	102.6 - 102,8
	SiO ₄ (Q)	103.2 - 103,6

4.2.2.4 Density

The plasma polymerized organosilicons exhibit higher densities compared to the conventional polysiloxanes such as PDMS. Indeed, the plasma polysiloxanes reveal a highly more crosslinked structure than their analogues conventionally polymerized. Indeed, the PP-HMDSO density can varies from 1.1 to 2.2 g.cm⁻³ depending on the plasma deposition conditions (from the softest to the hardest ones). However, the PDMS, which is the closest conventional polymer to the PP-HMDSO elaborated in low energetic plasma, has a density of 0.98 g.cm⁻³ [94,95].

4.2.2.5 Refractive index

The refractive indices of plasma polysiloxanes have been widely reported in the literature. This characteristic depends not only on the material chemical composition, but also on the material density. In fact, according to the Clausius-Mosotti equation (8) the refractive index n is directly related to the dielectric constant ϵ of the material, i.e. $\epsilon = n^2$ in the visible optical range.

$$\frac{\varepsilon - 1}{\varepsilon + 2} = \frac{\rho_m}{3\varepsilon_0} \sum_{i=1}^k N_i \alpha_i \quad (8)$$

Where ρ_m is the material density, ε_0 is the vacuum permittivity, N_i is the number of atoms i per cm^3 , and α_i is the polarizability of atom i .

Therefore, the variations of the material density and chemistry induce a variation of the material refractive index. The plasma polysiloxanes refractive index varies from 1.4 to 1.9, depending on the material density as well as the chemical composition [94,115,116] which are directly related to the deposition conditions. For soft plasma conditions (low W/F.M) the refractive index (≈ 1.4) is close to the conventional PDMS refractive index (1.43). However, for hard plasma conditions (high W/F.M), the high value (1.9) compared to the silica (which is a dense Si-O material) refractive index (1.47), is mainly due to the chemical composition (high carbon content) [117,118].

4.2.2.6 Wettability

The wettability of the PP-HMDSO thin films is highly dependent on the gas/monomer mixture on the one hand and on the Yasuda parameter (W/F.M) on the other hand. For instance, a film elaborated from a mixture of HMDSO and O_2 exhibits a water contact angle (WCA) of 33° [119]. However, in this study we are interested in hydrophobic films and WCA measurements previously revealed that the PP-HMDSO films can be very hydrophobic: the non-polar methyl groups present on the surface electrostatically shield the polar Si-O-Si chain and give a non-polar and hydrophobic characteristic to the surface [120]. For example at low plasma energy, plasma polymers elaborated from pure HMDSO can exhibit a contact angle up to 130° [121–124].

All these characterization techniques allow us to conclude that plasma organosilicon films possess a complex structure and are basically composed of siloxane (Si–O–Si) chains and methylsilyl (Si–CH₃)_x groups. In addition, the main skeleton chains are also formed by other chains such as Si–(CH₂)_x–Si or Si–O–C. As well, the characterization techniques can detect the presence of Si–OH and Si–H as chain terminations. In this structure, the M, D, T, Q (see Table 6 and Table 7) and the additional Si(CH₃)₃(CH₂) (denoted S) environments will be the main components forming the film, knowing that the methyl groups can be replaced by –OH or –H. Furthermore, and despite the higher material density compared to conventional PDMS, the plasma organosilicon films elaborated in soft plasma contain free volumes in the material structure. Figure 11 represents an idea of a PP-HMDSO chemical structure.

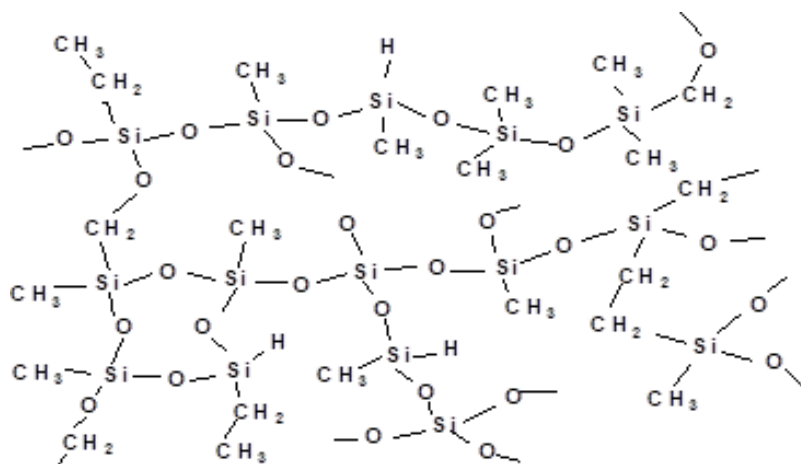


Figure 11: A representation of the structure of a PP-HMDSO film (illustrated from [95])

All the characteristics of the PP-HMDSO films mentioned above made them gain the attention of the science community and industries for several applications.

In the next section, the different applications employing plasma organosilicon materials will be mentioned. In particular, we will be focusing on the gas sorption applications. Hence, a state of the art concerning the gas sorption into plasma organosilicons will be presented which is complementary to another one focused on the BTEX sorption into plasma organosilicons illustrated in chapter 4 (introduction of the second article).

4.2.3 The PP-HMDSO different applications

In recent years, the scientists showed high interests in the organosilicon thin films technology for different fields of application due to their important and adjustable properties. We can mention applications fields such as microelectronics [125], biocompatible coatings [126,127], optics [128,129], anticorrosion protection [130], solar cells [131], water vapour and oxygen barrier [132]. Several properties of polysiloxanes (optical transparency, resistance, controllable refractive index, etc.) make these materials very attractive for optical applications. They are mainly used as anti-reflection protective layers or as components for integrated circuits (waveguides, interconnections, corner reflectors). In the field of electricity and electronics, plasma polysiloxanes are used as electric insulant for semiconductor technology. In biotechnology, plasma polysiloxane films are used to cover biomedical membranes to make them biocompatible. Certain specific characteristics of the plasma organosilicon films such as low thickness, uniformity, high adhesion, and the absence of defects, make them suitable for gas sorption applications. Furthermore, and most importantly plasma organosilicon polymers are formed of flexible Si-O-Si chains, which facilitate the penetration of gases within them. As

well, the hydrophobicity and the crosslinking degree of these deposits offers them the capacity of being selective.

Several works integrated plasma organosilicon materials in the field of gas sensing, permeation or separation. For example, Roualdes *et al.* have tested plasma polymerized organosilicon thin films prepared by a low frequency PECVD for the permeation and sorption of N_2 , H_2 , CO_2 and CH_4 . The permeation performances were studied as a function of the W/F.M ratio i.e. plasma energetic character which affects the films composition and structure. The sorption results showed a better performance for the films with an organic character i.e. elaborated at low W/F.M due to their low density and high chain flexibility [115]. In addition, Bosc *et al.* have worked on plasma polymerized HMDSO membranes for measuring the sorption of hydrocarbons (an alkane series) using a QCM setup. The gas permeation measurements showed that the permeability increases with hydrocarbons chain length due to a stronger interaction between the polymer and the penetrant. In addition, they also concluded that the solubility is highly dependent on the critical volume of the penetrant molecules. In fact the solubility increases with carbon atoms, however this assumption is limited when the diffused molecules size is close to the free volumes size [133]. Similarly, Rouessac *et al.* have synthesized organosilicon materials by PECVD using a mixture of cyclic and linear siloxane monomers for hydrocarbons sorption. The sorption performance was measured as a function of the material composition and structure using QCM. As a result, they showed that the hydrocarbons affinity and selectivity is strongly dependent of the material chemical structure. In fact, the increase of the cyclic Si-O-Si percentage in the material decreases the vapours solubility due to more rigid materials. However, when the number of the linear Si-O-Si chains is important in the material the hydrocarbons solubility increases due to a more flexible structure [134]. More recently, Andreeva *et al.* have studied the affinity of a plasma organosilicon material towards toluene, formaldehyde and water using QCM. As a result, they showed that the organosilicon super hydrophobic material is suitable for the detection of low polar vapours such as toluene and formaldehyde. Their results were also interpreted considering the high specific surface area. On the contrary, the water adsorption showed a poor performance due to the hydrophobicity of the material [135]. One can also mention the work of Bougharouat *et al.*; presenting the detection of different VOCs vapours by organosilicons (ethanol, methanol, acetone and chloroform) using QCM. Their results showed good affinities especially to methanol which was linked to material hydrophobicity and the presence of free volumes [7].

Since organosilicons showed good performances in the field of gas sensing, this study will be focusing on the use of plasma polymerized organosilicon thin films in the field of gas detection and monitoring applications.

As mentioned above, the accurate knowledge of the organosilicon chemical structure is necessary to understand the vapours (VOCs) sorption mechanism into these materials. The experimental data presented earlier can be sometimes not very accurate due the complexity of the polymer network (such as XPS). Therefore, in addition to the chemical characterization used, quantum calculations ensure a theoretical support for the experimental data. For example, the combination of XPS experimental analysis and DFT calculations refine the investigation of the film surface structure. The following section will attack the theoretical background of the quantum calculations specifically the simulation of XPS spectra by DFT calculations.

5 Theoretical section: DFT Calculations and XPS spectra simulation

Quantum methods such as the density functional theory (DFT) can be used to determine electronic properties of molecules and solids. For example, calculations of core electron binding energies can help and support XPS experimental data. In this section, we will present some theoretical concepts about quantum methods as well as XPS spectra simulations on polymers and specifically organosilicons.

5.1 The Schrödinger equation

The Schrödinger equation is a fundamental equation in quantum. This equation can give information on the evolution over time of a non-relativistic system taking into account quantum effects. Despite the fact that this equation describes evolutions over time, it can be simplified to a time independent equation:

$$\hat{H}\Psi = E\Psi \quad (9)$$

Where \hat{H} is the Hamiltonian operator, Ψ is the wave function and E represents the total energy of the state Ψ .

The Hamiltonian operator for a system of N nuclei and n electrons can be expressed by (in a.u.):

$$\hat{H} = - \sum_I^N \frac{1}{2M_I} \nabla_I^2 - \sum_i^n \frac{1}{2} \nabla_i^2 - \sum_I^N \sum_i^n \frac{Z_I}{r_{Ii}} + \sum_{J>I}^N \frac{Z_I Z_J}{R_{IJ}} + \sum_{j>i}^n \frac{1}{r_{ij}} \quad (10)$$

Where, M_I and Z_I are respectively the mass and the charge of the nucleus I , r_{Ii} represents the distance between an electron and a nucleus, while R_{IJ} is the distance between two nuclei I and J , and r_{ij} is the distance between two electrons i and j . In equation (10), the first term represents the kinetic energy of the nuclei and the second term represents the electrons kinetic energy. While, the third term depicts the electrostatic attraction between electrons and nuclei. Finally, the two last terms describe the nuclei/nuclei and electron/electron repulsions respectively.

The wave function Ψ is a mathematical representation of a quantum state of a quantum system. Ψ is for instance function of the particle position or its momentum. The presence

probability of a particle at a given position is a real number and can be calculated from the square modulus of its wave function, *i.e.* $|\Psi|^2$.

The Born-Oppenheimer approximation considers that the nuclei are much slower than the electrons due to their difference in mass. Thus, it can be assumed that the nucleus are fixed and their kinetic energy is negligible compared to the one of the electrons. This approximation allows the reduction of the Schrödinger equation to the electronic Schrödinger equation leading to the electronic wave function:

$$\hat{H}_{electrons}\Psi_{electrons} = E_{electrons}\Psi_{electrons} \quad (11)$$

However, for systems with more than one electron, there is no analytical solution to the Schrödinger equation due to its complexity. Different methods have been developed to bypass this problem and approximate solutions can be obtained. The density functional theory for instance leads to a resolution of the Schrödinger equation for systems of physical interest.

5.2 Density Functional Theory

The principle of the density functional theory is to replace the n -electrons wave function $\Psi(\vec{r}_1, \vec{r}_2, \dots, \vec{r}_n)$ by the electron density $\rho(\vec{r})$ which is the number of electrons per volume at a specific position \vec{r} . The main two theorems responsible of the creation of DFT were established by Hohenberg and Kohn (HK) [136].

First theorem known as the existence theorem, is based on relating all the properties of a system in a ground electronic state to the ground state electron density $\rho_0(x, y, z)$. In other words, the determination of the ground state electron density allows the calculation of any ground state property. The energy for example can be calculated from the ground state electron density:

$$E_0 = E(\rho_0) \quad (12)$$

Second theorem known as the variational theorem, states that the calculation of the ground state energy using a trial electron density function can fall on a higher or equal value than the real ground state energy. Therefore, the ground state electron density function is calculated using a variational method.

The approach therefore established later by Kohn and Sham [137] will be explained in the following section.

5.2.1 The Kohn-Sham approach

In the Kohn-Sham approach, the electronic energy of system is represented by equation (13):

$$E[\rho] = T[\rho] + E_{Ne}[\rho] + E_{ee}[\rho] \quad (13)$$

Where, the first term represents the electron kinetic energies, the second term describes the nucleus-electron attraction potential energies, and the last term represents the electron-electron interaction energies.

The second term $E_{Ne}[\rho]$ is the sum (integral) over all n electrons of the potential corresponding to the electron attraction for all the nuclei I , thus the previous becomes:

$$E[\rho] = T[\rho] + \int \rho(\vec{r}) v_{Ne}(\vec{r}) d\vec{r} + E_{ee}[\rho] \quad (14)$$

The problem of this equation is the difficulty of determining the kinetic and interaction energies functionals, $T[\rho]$ and $E_{ee}[\rho]$. Hence, Kohn and Sham proposed a resolution using a non-interacting electrons reference system. The non-interacting electrons system has to provide a ground state electron density distribution similar to the real system ($\rho_{ref} = \rho_0$). The difference in energy between these two systems is compensated by a ‘correction’ term called the exchange and correlation energy $E_{XC}[\rho]$.

The exchange and correlation energy $E_{XC}[\rho]$ comes first from the difference between the electron kinetic energy in the reference system, expressed from ρ_{ref} , and the real electron kinetic energy, calculated from ρ_0 . Thus, a quantity $[\rho]$, representing the variation between the electron kinetic energies of the two systems, is defined as: $\Delta[\rho] = T[\rho]_{real} - T[\rho]_{ref}$.

In addition, the variation between the real electron-electron energy and the classical electrostatic coulomb repulsion energy is defined as $\Delta E_{ee}[\rho]$ and can be written as:

$$\Delta E_{ee}[\rho] = E_{ee}[\rho]_{real} - \frac{1}{2} \iint \frac{\rho(\vec{r}_1)\rho(\vec{r}_2)}{r_{12}} d\vec{r}_1 d\vec{r}_2 \quad (15)$$

By replacing $[\rho]_{real}$ and $E_{ee}[\rho]_{real}$ in equation (15), we obtain the electronic energy equation determined from the Kohn and Sham approach:

$$E_{KS} = \int \rho(\vec{r}) v_{Ne}(\vec{r}) d\vec{r} + \frac{1}{2} \iint \frac{\rho(\vec{r}_1)\rho(\vec{r}_2)}{r_{12}} d\vec{r}_1 d\vec{r}_2 + \Delta E_{ee}[\rho] + \Delta T[\rho] + T[\rho]_{ref} \quad (16)$$

The two Δ terms shown in this equation represent the electron-electron repulsion energy deviation from the classical system and the kinetic energy deviation from the reference system respectively. Thus the exchange-correlation energy is:

$$E_{XC}[\rho] = \Delta E_{ee}[\rho] + \Delta T[\rho] \quad (17)$$

Therefore, The Kohn-Sham electronic energy equation (16) can be written as:

$$E_{KS} = T[\rho]_{ref} + \int \rho(\vec{r}) v_{Ne}(\vec{r}) d\vec{r} + \frac{1}{2} \iint \frac{\rho(\vec{r}_1)\rho(\vec{r}_2)}{r_{12}} d\vec{r}_1 d\vec{r}_2 + E_{XC}[\rho] \quad (18)$$

The Kohn-Sham energy equation is exact. However, it won't give a correct energy unless the exact electronic density function $\rho(r)$ and the functional for the exchange-correlation energy $E_{XC}[\rho]$ are known. Thus, determining the $E_{XC}[\rho]$ term is a need.

5.2.2 Approximation of $E_{XC}[\rho]$

The main problem of the DFT is to find an accurate expression of the functional $E_{XC}[\rho]$. Thus, several scientists proposed approximations for this functional such as the local density approximation (LDA) and the generalized gradient approximation (GGA) that have been used in our work. Other functionals, *e.g.* hybrid functionals will thus not be described.

5.2.2.1 The local density approximation (LDA)

The local density approximation is based on the assumption that the exchange and correlation energy term depends only on the local electronic density value $\rho(r)$. In addition, the LDA approximates that at every point in the system the electron density is considered as a homogeneous electron gas. Thus, the value of the energy density at this point, is similar to the one given by the uniform electron gas and the exchange-correlation energy can be expressed as followed:

$$E_{XC}^{LDA}[\rho(\vec{r})] = \int \rho(\vec{r}) \varepsilon_{XC}[\rho(\vec{r})] d\vec{r} \quad (19)$$

Where, ε_{XC} is the exchange and correlation energy of a homogenous electron gas.

The LDA can give correct results for systems in which the variation of the electronic density is low. However, it can poorly describe some properties such as the bonding energies, bond lengths and the semiconductor/insulators gap. This method is usually replaced by other approximation for the exchange and correlation energy that uses the electron density and its gradient.

5.2.2.2 The generalized gradient approximation (GGA)

The generalized gradient approximation (GGA) is one of the highly used methods nowadays. This approximation of the exchange-correlation energy uses both the electron density and its gradient. The gradient of the electron density is the first derivative of the position.

The GGA split the exchange correlation energy functional in two functionals, *i.e.* an exchange-energy functional and a correlation-energy functional as presented in equation (20):

$$E_{XC}^{GGA} = E_X^{GGA} + E_C^{GGA} \quad (20)$$

The GGA reduces the bond dissociation energy error and ameliorate the bond lengths and angles. However, they are more computationally expensive than LDA functionals. The functional used in our work is the Perdew, Burke, and Enzerhof functional (PBE)[138].

After this overview, the basis of the XPS spectra simulation for polymers will be presented.

5.3 XPS spectra simulation

The simulation of XPS spectra is based on quantum methods. The Binding Energy (BE) of a core electrons can be calculated using the difference between the total energy after ionization (final state) and the total energy before ionization (initial state) of the system of interest [139–142]:

$$BE = E^{N-1}(final) - E^N(initial) \quad (21)$$

Where N is the total number of electrons of the system.

This theoretical aspect can strongly support the experimental data. In fact, XPS analyses can lead to complicated spectra especially when the chemical surface of the material is complex and contains a large number of chemical group. Therefore, the quantum calculations combined with experimental XPS refine the investigation of the surface chemical composition allowing a more accurate decomposition of the core levels.

For example, Giesbers *et al.* compared several methods to simulate XPS spectra of a wide range of organic monolayers using DFT calculations and second-order Møller–Plesset theory (MP2) combined with many basis sets. The core level spectra were calculated using the Koopmans' theorem. The calculated results were compared to the experimental data in order to find the most accurate method. After correcting the core level position (by shifting the computed binding energies), the B3LYP/6-311G(d,p) method was the more accurate method to simulate C 1s core levels. In fact, a good match is obtained between the experimental data and the calculated BE of the different carbon functional groups with a maximum error of 0.3 eV [143]. Smith *et al.* also used DFT calculations to decompose C 1s and O 1s XPS spectra of cellulose chars [144]. The Koopmans' theorem was applied to determine the core binding energy. This theorem estimated the core level binding energy as the negative of the electron's shell energy in the initial state. However, this method needs a linear correction factor to estimate

reasonable binding energies. The calculated binding energies (after the linear correction) as well as the simulated spectra shapes matched exceptionally well with the experimental core levels [144]. Later, Duguet *et al.* combined DFT calculations and experimentally determined XPS spectra to characterize the surface of a poly epoxy polymer [145]. They used a macromolecule made from one DGEBA and one EDA molecules as a model of the poly epoxy and they performed DFT calculations of O 1s, N 1s and C 1s core levels binding energy of the different environments present on the polymer surface in the framework of the Δ KS approach ($BE = E^{N-1}(final) - E^N(initial)$). Accordingly, they calculated the binding energy shifts that lead them to decompose the O 1s core level and the C 1s core level into two and five environments respectively. As a result, this methodology allowed them to distinguish phenyl groups from methyl bonds, C-OH and a part of C-O-C bonds from other C-O-C bonds [145]. Later on, the same group also studied the interaction between Cu atoms and the poly epoxy surface [140] and they simulated XPS spectra to investigate the bonding mechanisms of the Cu atoms on the poly epoxy polymer (Δ KS and u-GTS approaches). The simulation of the XPS spectra of the Cu/polymer shows the replacement of the initial C-OH component by new C-O-Cu bond and the formation of other new groups such as $C_{phenyl}(Cu)$. The O 1s core level decomposition also reveals the presence of $C_{phenyl}-O-C$ and $Cu-O-C$ bonds [140].

Basically, very few attempts are available in the literature concerning the decomposition of Si 2p XPS spectra of organosilicons using *ab initio* calculations. Otsuka *et al.* simulated thanks to DFT calculations the C1s, N1s, O1s or F1s core levels of a large range of polymers including organosilicons such as PDMS. The calculation of the model molecules core electron binding energies (CEBEs) was performed within the framework of the uGTS approach. The computed CEBEs of all the polymers using uGTS method are in better agreement with the experimental values compared to those calculated using Koopmans' theorem. Furthermore, reasonable polymers WDs were obtained; WDs being the difference between the oligomers CEBEs (which corresponds to the gas phase) and of the polymer (solid phase) [146]. We can also mention the work of Motozaki *et al.* [147]. They also used DFT to calculate CEBEs of gas molecules containing silicon atoms using the unrestricted generalized diffuse ionization (uGDI) method. They succeeded to compute acceptable CEBEs values with an aged absolute deviation (ADD) value of 0.37. Furthermore, they calculated Si 2p, O 1s and C 1s CEBEs for silicone polymers such as PDMS using deMon-KS DFT calculations. Reasonable differences between the calculated and experimental CEBEs were obtained.

As shown in the chemical characterization section, the PP-HMDSO surface can contain a wide range of Si environments, which complicates the surface characterization using

empirical methods only. Thus, one of this work's aims is to simulate using DFT calculations Binding energy differences (ΔBE) between the components in order to refine the material surface characterization. This attempt will provide a progress in the Si 2p core level decomposition with different siloxy contributions.

6 Conclusion

This first chapter pointed out the general context in which this PhD thesis was initiated and carried out. The hierarchy of the sections presented in this chapter, starting with the necessity of BTEX sensing, then going through the different gas sensing techniques with a focus on the gravimetric methods as well as the PECVD deposition process and the organosilicon materials for the VOCs detection and finally by the DFT calculations allows to draw the objective of this thesis.

The objective of this work is to understand the VOCs, specifically BTEX vapours, sorption mechanism into organosilicon materials for gas sensing applications. In the next chapter we will present the materials and methods used during this PhD thesis.

Chapter 2: Materials and Methods

In this section, the materials and methods used during this PhD thesis will be presented. First, the film deposition process will be described as well as the PECVD reactor. Then, all the characterization techniques and the experimental parameters of each technique will be detailed. As well, the sorption characterization methods will be described and their operating modes will be thoroughly explained. Finally, the DFT computational details will be mentioned. We should note that all the materials and methods introduced in this chapter are also described in the following articles (chapters 3 to 5), but grouping them in one ‘materials and methods’ chapter aims at simplifying the manuscript reading (the “materials and methods” section in every results chapter, *i.e.* every article so being not required to be read).

1 Sample preparation

1.1 Films deposition

The plasma polymerized HMDSO (PP-HMDSO) thin films were elaborated in a microwave (MW-) PECVD reactor supplied by Boreal Plasmas (HEF Group). Figure 12 represents a scheme representation of the PECVD reactor. The reactor enclosure is a cylindrical chamber (interior diameter around 200 mm); pumped using a primary pump (Oerlikon- Trivac, 25 m³/h) and a secondary turbo-molecular pump (Oerlikon-Turbovac, 145 L/s). The maximum pressure attended in the enclosure is around 1.10^{-6} mbar (pressure gauge). The PECVD reactor is supplied by a microwave generator (2.45 Hz, Sairem) using ECR antennas [148]. These applicators are distributed on the top of the chamber at a distance of 7 cm from the sample holder, forming a rectangular lattice matrix (3 x 2, 11 x 5.5 cm) (only two antennas are shown in the scheme). This distribution ensures the homogeneity of the discharge and the deposited films [148].

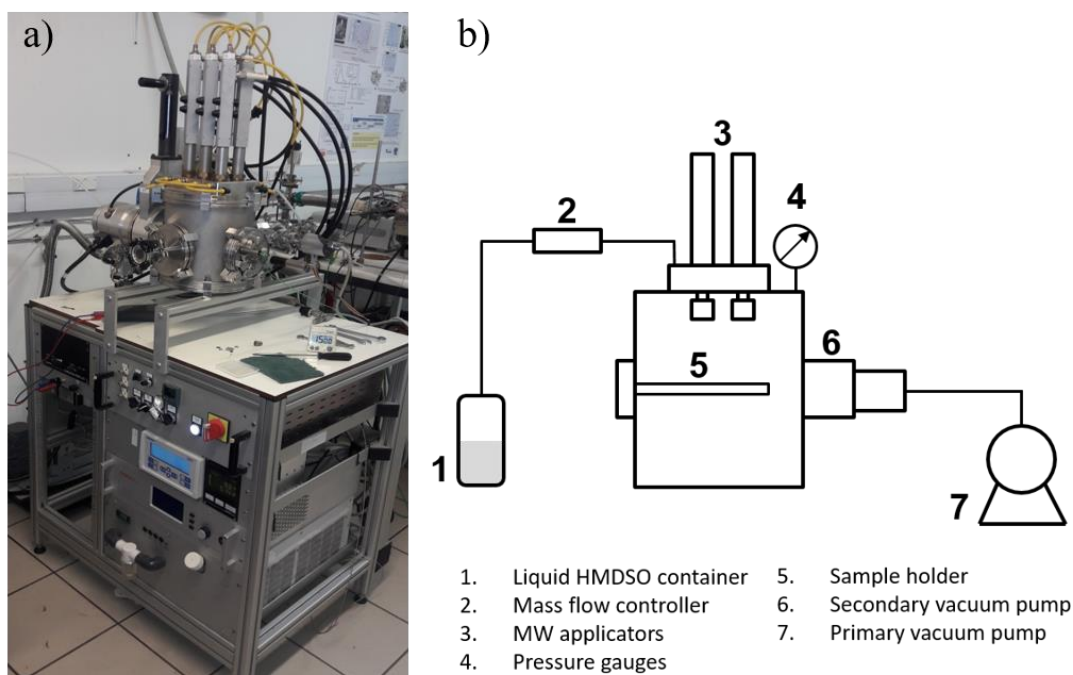


Figure 12: a) The PECVD reactor used during this thesis b) MW- PECVD set-up scheme

The HMDSO precursor (Sigma-Aldrich $\geq 98.5\%$) was injected with no dilution or carrier gas into the chamber using a mass flow controller (Brooks). The depositions were all carried out at room temperature. The plasma input power W and the monomer flux F were varied from 20 W to 140 W and from 1 sccm to 8 sccm, respectively. The microwave generator

(1000) was used within its lower operating limit: 20W; thus for low W/F values, the flux has been increased.

The W/F (Yasuda parameter explained above) composite ratio represents the plasma energetic behaviour. This parameter was simplified by removing the precursor molecular weight (M) because it is constant (same precursor for all deposits). Accordingly, the films were synthesized at different W/F values ranging from “soft” for the lowest W/F values, to “hard” for the highest. It must be mentioned that there was no temperature increase during the films deposition. Table 8 reports the deposition conditions of each sample denoted as “WFX”, X being the W/F ratio value.

Table 8: MW-PECVD thin films deposition parameters.

Sample	Plasma power (W)	HMDSO flux (sccm)	W/F	Deposition pressure ($\times 10^{-3}$ mBar)	Thickness (nm)	Average growth rate (nm/min)
WF2.5	20	8	2.5	15.5	308	154
WF5	20	4	5	10.5	337	109
WF10	20	2	10	7.5	351	58
WF20	20	1	20	5.9	242	30
WF40	40	1	40	6.2	395	33
WF70	70	1	70	6.4	314	31
WF140	140	1	140	6.7	257	29

The errors on average thicknesses are deduced from the standard deviation over three measurements and they are typically ± 3 nm. For the quantitative Solid-state ^{29}Si NMR analyses, four samples were prepared (WF2.5 to WF20). These films were deposited on glass substrates and the powder was collected by scratching the films with a metallic spatula. The deposition times for the WF2.5, WF5, WF10 and WF20 samples were 7, 13, 13, 28 hours, respectively, carried out twice for WF5 and WF10 and three times for WF20. Approximately, 400 mg was collected for each sample and packed into a ZrO_2 rotor with a diameter of 7.5 mm. For the QCM measurements WF5 thin films were deposited on an AT-cut gold covered quartz (6 MHz). Whereas, for all other analytic methods, films were deposited on a (100) p-type silicon wafer (Si-Mat) in all conditions reported in Table 1. A PP-HMDSO collected powder and thin film deposited on a silicon substrate are shown in Figure 13.

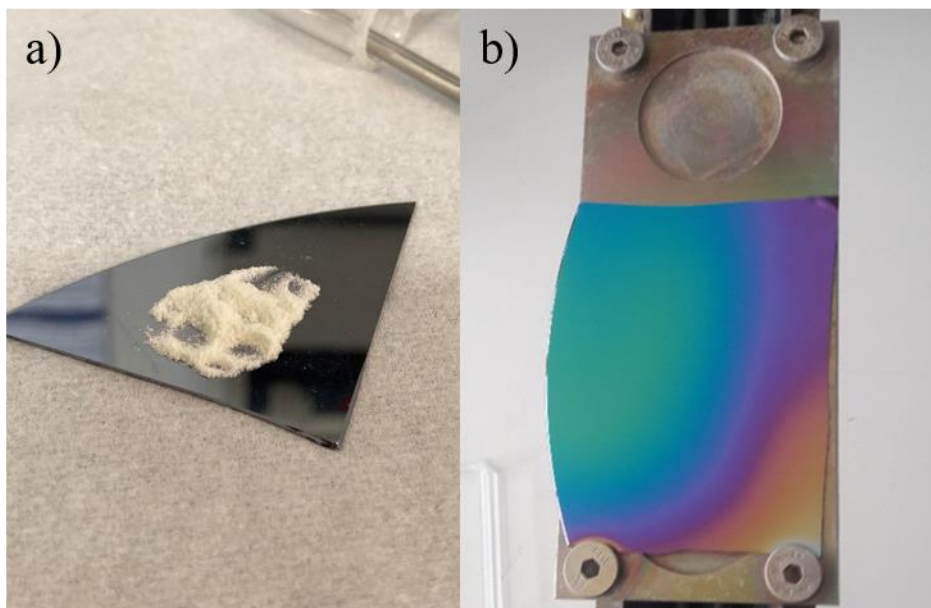


Figure 13: a) PP-HMDSO powder collected for ^{29}Si NMR analysis b) PP-HMDSO thin film deposited on a 5 cm x 7 cm silicon substrate.

1.2 Films thermal treatment

The WF5 samples were annealed under air and nitrogen flow at three different temperatures 250°C, 300°C and 350°C in order to test the sorption performance after annealing (the temperature range choice was based on the TGA analysis). The temperature-heating rate was 5 °C.min⁻¹ from room temperature up to the desired temperature, followed with a plateau of 15 minutes was maintained before cooling.

2 Characterization methods

The different characterization techniques aim to investigate the bulk and surface chemical composition of the organosilicons, the physical properties and more importantly the gas vapours sorption. They will be detailed hereafter.

2.1 Bulk characterization

2.1.1 Fourier Transform InfraRed spectroscopy

Fourier Transform Infrared spectroscopy (FTIR) is a characterization technique that determines the chemical bonds nature of a material. The sample is scanned by an IR radiation range with different wavelengths. So, the FTIR is based on the absorption of some infrared radiation by the analysed sample following the Beer-Lambert equation. This absorption corresponds to vibrations (stretching or bending) or forced rotations of bonds present in the material. Only vibrations involving a variation in the dipole moment of the molecule can generate an absorption in the infrared. The molecular vibration frequency at which light energy is absorbed depends on the nature of the bonds, the chemical environment, and the mass of the atoms involved, *i.e.* the material chemical structure. The intensity and area of the absorption bands depends mainly on the magnitude of the change in the dipole moment of the vibrating molecule.

In this work, this technique is used for the bulk chemical composition characterization of the organosilicon material. FTIR absorption spectra were collected between 400 cm^{-1} and 4000 cm^{-1} using a ThermoFisher IS-50 spectrometer, in transmission mode at room temperature. The scanning velocity was 0.4747 cm/sec .

The background signal (silicon wafer) was subtracted from all the spectra. The spectra deconvolution and the baselines correction were done using Labspec software.

2.1.2 ^{29}Si Solid- state Nuclear magnetic resonance

Solid- state Nuclear magnetic resonance (NMR) is an extremely powerful technique that gives information about the chemical environment of an atom by detecting variations in the nuclei magnetization under the effect of a magnetic field and an electromagnetic wave. The NMR is applicable for both solid and liquid state; however, in our case we will be clearly interested in the solid-state NMR. The magnetic moment of a nuclei population placed in a magnetic field B_0 form a real oscillator characterized by a frequency known as Larmor frequency. During the NMR experiment, an electromagnetic wave (oscillating in the radio

frequency domain) is applied to the oscillator which absorbs the wave energy. During the frequency scanning, when the frequency of the applied wave is equal to the oscillator one, the energy absorption is maximum resulting in the appearance of a resonance peak. This phenomenon is very strong for nuclei with a non-integer spin, such as ^{29}Si (spin of $1/2$).

The detection of thin films by quantitative ^{29}Si solid state NMR is considered as a big challenge due to the necessity of collecting a huge material mass (hundreds of milligrams). During this thesis, the interests of using this technique for organosilicon chemical characterization are: first, it is rarely found in the literature for organosilicons thin films; second, it completes the bulk chemical characterization of organosilicons by providing a quantitative analysis on the different component present in the materials.

Concerning the operational mode, Solid State ^{29}Si NMR spectra were recorded on a 300 MHz Varian VNMRS300 spectrometer ("Wide Bore" magnet at 7.05 Tesla) using a Varian T3 MAS (Magic Angle Spinning) probe with 7.5 mm ZrO_2 rotors. Spectra were acquired using the quantitative SP technique (Single Pulse) with Magic Angle Spinning and 1H decoupling. A $\pi/2$ pulse was used with a duration of 6 μs , the recycle delay was chosen to be 60 s and the spinning rate of all the samples was 5 kHz. Q8M8H (octakis-(dimethylsiloxy)octasilsesquioxane) was used as a secondary reference (left peak at -2.25 ppm). The width of the spectral window was 50 kHz and the line broadening was 50 Hz. The NMR spectra were fitted using Gaussian/Lorentzian peaks with DMFIT software package.

2.1.3 Energy dispersive X-ray spectroscopy

Energy dispersive X-ray spectroscopy (EDS or EDX) is a chemical composition characterization technique that determines the elemental composition of a sample. The EDX process is based on the ionization of atoms by an electron beam leading to holes formation in the core electronic shells. After the ionization, these holes are filled by the electrons present in the outer shells leading to the emission of X-rays (deexcitation energy). This technique was combined during this work with the X-ray reflectometry in order to determine the material density (this combination will be presented later in this chapter). The EDX analysis was performed on a sample with a thickness of 1.5 μm approximately (to eliminate the risk of detecting the Si of the silicon substrate) using a Silicon Drift Detector (SDD), X-MaxN, Oxford Instrument.

2.2 Surface characterization

2.2.1 X-ray photoelectron spectroscopy

X-Ray Photoelectron Spectroscopy (XPS) is a powerful technique for the surface chemical composition characterization. It allows the determination of the elemental composition as well as the different environments present on the surface (from a few Å up to 10 nm).

The principle of XPS is based on bombarding a sample surface with X-Rays and then analysing the emitted electron energy. The sample irradiation with X-rays provokes the extraction of an electron from the core-level of the atoms called photoelectron with a specific kinetic energy. The measurement of the electron kinetic energy allows the determination of electron binding energy in its atomic level using the following equation:

$$BE = h\nu - KE - \varphi_{sample} \quad (22)$$

Where BE is the electron binding energy, $h\nu$ is the photon energy, KE is electron the kinetic energy and φ represents the work function of the sample. Actually, the Fermi levels of the sample and the spectrometer are equal because they are electrically connected. Therefore, an electric field appears affecting the photoelectron (acceleration) due to the difference between the two work functions φ_{sample} and φ_{spec} (Figure 14). Thus, this term ($\varphi_{sample} - \varphi_{spec}$) is added to equation (22) giving:

$$BE = h\nu - KE - \varphi_{sample} + (\varphi_{sample} - \varphi_{spec}) = h\nu - KE - \varphi_{spec} \quad (23)$$

Where φ_{spec} is a constant determined by the apparatus calibration.

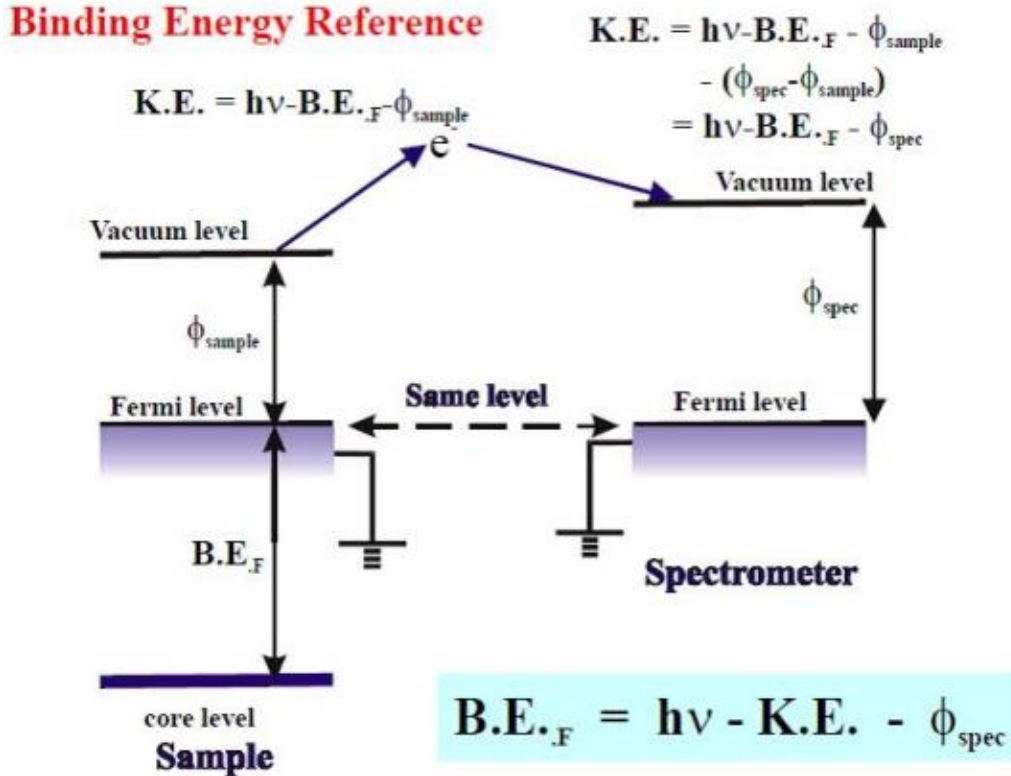


Figure 14: XPS principal measurements illustrated from [149]

The XPS analysis performed during this work was carried out using a Thermo Scientific K-Alpha X-ray Photoelectron Spectrometer. In order to record the photoemission spectra, Al-K α radiation ($h\nu = 1486.6$ eV) was used from a monochromatized source. The diameter of the spot on the sample surface was 400 μm . We fixed the pass energy at 30 eV for narrow scan and at 170 eV for survey scans. A Shirley background was systematically subtracted. In the end, the photoelectron peaks were analysed and fitted using a combination of Lorentzian and Gaussian peaks in Thermo Advantage software.

2.2.2 Water Contact Angle

Water contact angle (WCA) analysis is usually used to determine the hydrophilic or hydrophobic character of the material surface. This method consists of dropping a water droplet on the surface of the material and measure the contact angle Θ at point between the surface, water and air as shown in Figure 15.

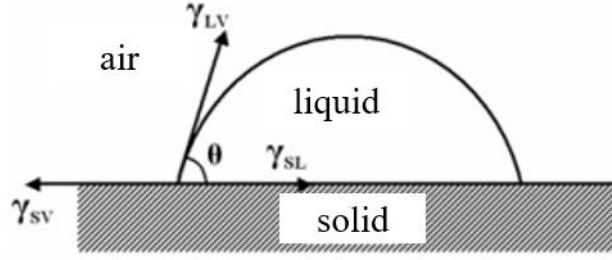


Figure 15: scheme representation of the WCA on a solid surface

Where γ_{SV} is the solid-vapour (air) interfacial tension (or surface energy); γ_{SL} is the solid-liquid interfacial tension; and γ_{LV} , liquid-vapour (air) interfacial tension. The three interfacial tension and the contact angle are linked together in the young's equation:

$$\gamma_{SV} + \gamma_{SL} + \gamma_{LV} \cdot \cos \theta = 0 \quad (24)$$

The WCA measurements were carried out using a lab-made apparatus composed from a camera which allows the acquisition of 6 μL drops photos deposited on a solid surface. All the drops were photographed ten seconds after their deposition on the film surface. The photographed drops were processed and analysed using the Image J software, which, together with the Drop Analysis plugin developed by EPFL, allows the determination of the WCA. The WCA was calculated as the mean value of 6 WCAs and the error on each mean value is deducted from the standard deviation over the six measurements.

2.3 Physical properties

2.3.1 X-ray reflectometry analysis

The X-ray reflectometry analysis (XRR) was used to determine the electronic density of the material. The XRR principle is based on applying an X-ray beam at grazing incidence on a flat sample. The intensity variation of the reflected beam is recorded as a function of the angle of incidence. Thus, the electron density (ρ_e) can be determined from the limit angle of total reflection (critical angle) which corresponds to total reflection half intensity Θ_c , using the following equation:

$$\Theta_c = \sqrt{\frac{\lambda^2 r_0}{\pi} \rho_e} \quad (25)$$

Where λ is the wavenumber and r_0 is the electron radius. X-ray reflectometry analysis (XRR) were carried out using a Bruker D8 diffractometer with Cu K α 1 ($\lambda = 0.154056$ nm) radiation. Standard θ – 2θ scans for the data collections were taken from $2\theta = 0$ to 4° with an angular resolution of 0.002° .

The elemental composition determined by EDX and the electronic density calculated by XRR analyses lead to the mass density (ρ_m) of the PP-HMDSO films using equation (26):

$$\rho_m = \rho_e \frac{\sum C_j A_j}{N_A \sum C_j Z_j} \quad (26)$$

Where C_j is the percentage of an element j in the PP-HMDSO chemical composition, Z_j its atomic number, A_j its atomic mass and N_A represents the Avogadro number. The error on the density value is estimated to be ± 0.03 g/cm³. This error is due to the zero-point error (sample height and/or goniometer) and the unknown hydrogen content which is needed to convert the electron density to the mass density.

2.3.2 Ellipsometry

Ellipsometry is an optical technique that allows to determine the thickness and refractive index of a low absorbent thin film (from a few nm to several μ m), deposited on a highly reflective support. This technique is based on the measurement of the light polarization state change after reflection on a flat surface. The polarization state change of the incident light beam is determined by the ratio (ρ_0) between the parallel and perpendicular reflection coefficients defined by the following equation:

$$\rho_0 = \frac{r_p}{r_s} = \tan \Psi \cdot e^{i\Delta} \quad (27)$$

Where r_p and r_s are the ratios of the parallel (index p) and perpendicular (index s) complex reflection coefficients of the analysed system respectively, $\tan \Psi$ is the amplitude ratio, and Δ is the phase difference after reflection.

The analysis is deduced from the acquisition of the curves of $\tan \Psi$ and $\cos \Delta$ as a function of λ (light beam wavelength), the thicknesses and indices of the superposed layers by mathematical regression of the experimental data based on an optical model. The samples optical response was modelled using a model composed of a semi-infinite plane substrate (silicon wafer) and a layer of uniform thickness (PECVD deposit), transparent in the visible as shown in Figure 16.

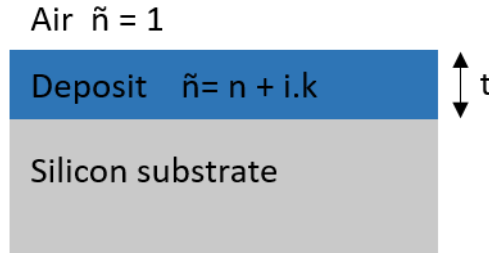


Figure 16: Ellipsometric model scheme

The complex refractive index of the thin film (\tilde{n}) is defined by equation (28), where n and k being the real and complex component:

$$\tilde{n}(\lambda) = n + i.k \quad (28)$$

Since the PECVD deposit is dielectric, the refractive index of the film can be expressed as function of λ using Cauchy's model for visible transparent dielectrics as follows (the extinction coefficient (k) is considered zero):

$$\tilde{n}(\lambda) = A + \frac{B}{\lambda^2} + \frac{C}{\lambda^4} \quad (29)$$

However, in the case where the material absorbs weakly in the UV range, the extinction coefficient k (not being zero) is added. Therefore, the Cauchy model for absorbent materials is completed by the following equation:

$$k = \frac{D}{\lambda} + \frac{E}{\lambda^3} + \frac{CF}{\lambda^5} \quad (30)$$

Thin films thicknesses and refractive indices (given at $\lambda = 633$ nm) were determined by spectroscopic ellipsometry (Semilab GES5E) at atmospheric pressure (Figure 17). The data were collected from 1.2 to 4.5 eV and fitted using a composition of Cauchy transparent dispersion law and a non-transparent dispersion term towards the UV range. The results are retained when the fit quality exceeds 0.99 in the full spectral range.

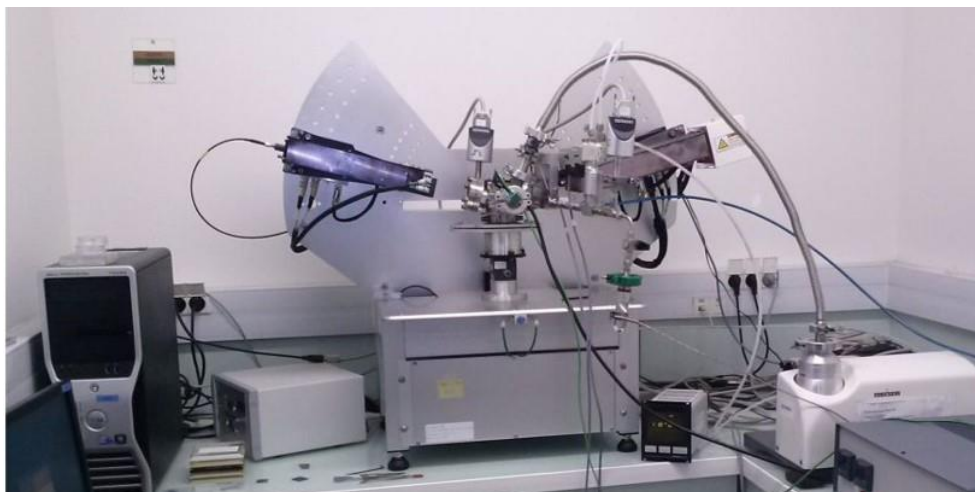


Figure 17: Ellipsometry apparatus used during this work

2.4 Thermal properties

2.4.1 Thermogravimetric analysis

The Thermo Gravimetric Analysis (TGA) was performed in order to investigate the thermal stability of the PP-HMDSO and to display the optimal atmosphere and annealing temperature. The analysis was carried out on a TGA-STD Q600 apparatus and the samples were purged with nitrogen or air flow rate of $100 \text{ ml} \cdot \text{min}^{-1}$. The temperature heating rate was constant at $5 \text{ }^{\circ}\text{C} \cdot \text{min}^{-1}$ from room temperature up to $1000 \text{ }^{\circ}\text{C}$. The samples weights were 5 mg for the sample purged with nitrogen flow and 10 mg for the sample purged with air flow.

2.5 Sorption characterization

2.5.1 Ellipsometry coupled to sorption

The ellipsometry coupled to sorption can be considered as an optical sensor (presented earlier in chapter 1 paragraph 2.2.1) which is able to detect changes in the polarization of the reflected light during the introduction of analytes in the polymer network. However, this technique is difficult to miniaturize. The polarization change is presented in term of refractive index and thickness variation with the increase of the probe concentration. Two cases can be considered:

1) Rigid porous material composed on 2 phases: pores surrounded by dense walls. Thus, the global refractive index is a combination of the refractive index of the pores and the refractive index of the walls. The last is constant whereas the refractive index of the pore can increase from 1 (material with open porosity under vacuum) up to the refractive index of the liquid probe if it is capillary condensed in the mesopores. This is the only case (equivalent to type IV

isotherm according to IUPAC) where it is possible to calculate the volume of the open porosity and also the pore size distribution (PSD) which directly depends on the shape of the refractive index isotherm as a function of the partial pressure of the probe. If the material is microporous, its refractive index increases also but it is not easy to calculate the microporous volume as the micropores do not represent a real independent phase. Thus its refractive index is unknown.

2) The material is not rigid. This is the case of PP-HMDSO synthesized at plasma low energetic conditions. It can swell as far as the probe molecules are sorbed in the network. The material cannot be considered as a mixture of phases. The material under vacuum is one phase represented by its refractive index, continuously varying as far as the probe incorporates the material by progressively spreading the polymers chains. The refractive index evolution as a function of the partial pressure of the probe can decrease or increase depending on the evolution of the swelling and the average dielectric constant.

Ellipsometry coupled to sorption (EP) measurements [150] was carried out by exposing PP-HMDSO thin films to toluene or ethanol at controlled vapour pressures (scheme presented in Figure 18). Samples were placed in a homemade optical cell equipped with pressure and temperature control systems. The lab-made cell was initially pumped under primary vacuum before any probe introduction down to 0.05 mbar. Afterwards, toluene or ethanol gas vapours were introduced into the vacuumed cell gradually up to its saturation pressure. For the thickness calculation, Cauchy model was always used as the global refractive index is that of a dielectric material, under vacuum or during any partial sorption of the probe.

Last, for easy calculation, the refractive index was considered constant along the depth from the surface, even if the concentration of the probe is probably higher close to the surface than deep in the layer. The concentration close to the material-silicon interface can be estimated very small as the material cannot easily inflate.

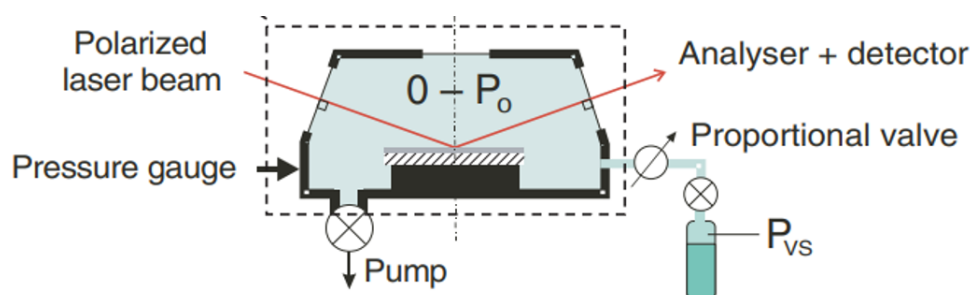


Figure 18: Ellipsometry coupled to sorption set-up scheme [151]

2.5.2 QCM coupled to sorption

The QCM is based on measuring the frequency shifts of a coated quartz crystal due to an additional mass uptakes caused by a contact with a gas vapour.

QCM measurements for gas sorption and desorption were performed using an Inficon STM2 thin film oscillator monitor driven by a lab-made data collection software in order to get mass uptake sorption isotherms (Figure 19). PP-HMDSO thin films were deposited on an AT-cut gold-covered quartz (6 MHz). The coated quartz was placed in a chamber under vacuum in which gas vapours were introduced systematically up to its saturated vapour pressure value at room temperature. During measurements, the quartz was thermally stabilized using a water circulation at 25°C. The frequency variation (Δf) between the coated quartz frequency at time t and t_0 was measured in MHz. Δf is proportionally linked to the mass variation (Δm) due to gas vapour sorption or desorption according to Sauerbrey's equation [151] (equation (6) shown previously):

$$\Delta m = -\frac{\sqrt{\rho_q \mu_q}}{2f_0^2} S \Delta f$$

Where ρ_q and μ_q are the density ($\rho_q = 2.65 \text{ g.cm}^{-3}$) and the shear modulus ($\mu_q = 2.947 \times 10^{11} \text{ g.cm}^{-1}.\text{s}^{-2}$) of the quartz respectively, S is the surface area of the deposited film (0.5 cm^2) while f_0 represents the resonant frequency (6 MHz).

The mass of the deposited film can be neglected compared to the mass of the quartz. Since the mass of both the quartz and the films are constant, Δm corresponds to the sorbed vapour mass uptake m_{sorbed} by the thin films. Therefore, the mass uptake (m_{sorbed}) of the deposited thin films was determined using equation (31):

$$m_{\text{sorbed}} (P/P_0) = \frac{-\Delta f}{f_q^2} 1.67 \times 10^5 \times \rho_q \times S \quad (31)$$

The collected data were converted into mass uptake and isotherms of m_{sorbed} as a function of relative pressure (P/P_0) were collected and plotted.

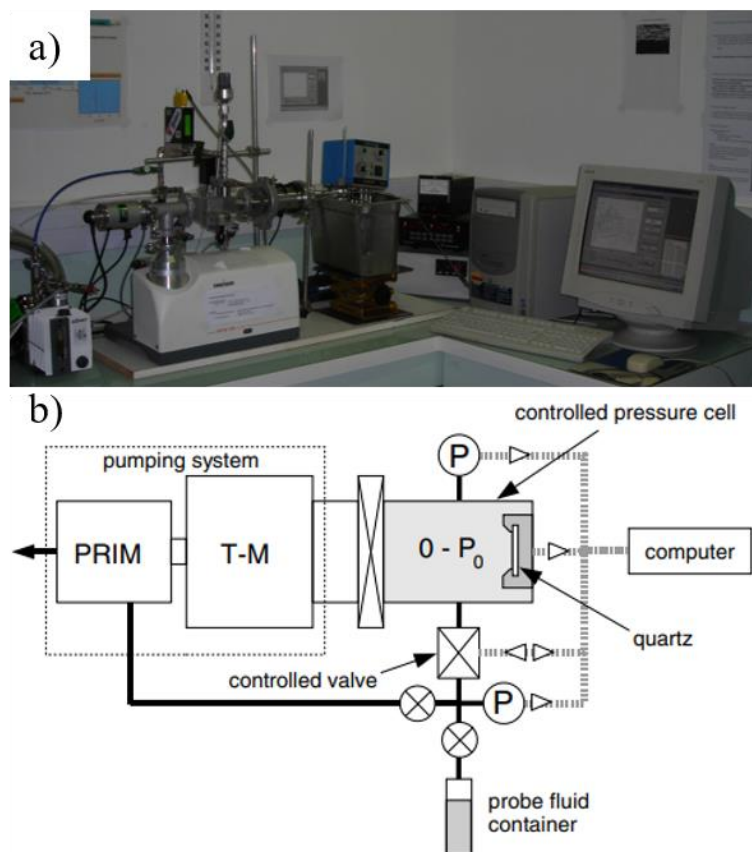


Figure 19: a) QCM apparatus used during this thesis b) QCM set-up scheme

3 DFT computational details

Density Functional computations were performed to calculate the electron core-level binding energies (BE) of Si atoms that are present in the chemical environments shown in Table 7.

Four PP-HMDSO molecules containing the S, M, D, T and Q environments were used as models of subparts of the material. These molecules are presented in Figures S1 to S4 (SI of article 1 shown in annex A). All geometries were fully optimized in vacuum using conjugate gradients methods. The gradient corrected PBE functional [138] was chosen together with the def2TZVP basis set [152,153] and Grimme's dispersion corrections were added [154,155]. We used the Gaussian 09 package [156]. All the stationary points were characterized as minima by a vibrational analysis and it was followed by a NBO [157] population analysis to determine the atomic charges.

The calculation of Si2p BE was done in a second step within the Δ KS (Kohn Sham) framework using the deMon2k code [158]. Thus, the BE (Δ KS) of electrons of the Si 2p core levels was determined using equation (32):

$$BE(\Delta KS) = E_{TOTAL} (Ion) - E_{TOTAL} (Neutral) \quad (32)$$

With $E_{TOTAL} (Neutral)$ and $E_{TOTAL} (Ion)$ the total energies of the neutral (initial state) and ionized (final state) molecules, respectively. The ionized molecule has one missing electron on the 2p orbital of the Si atom of interest.

To get these total energies, single point energy calculations were performed using the PBE functional [138], GENA2 auxiliary functions [159], an all electron potential and an augmented basis set (AUG-CC-PVTZ) [160] on the Si atom of interest, and a relativistic basis and effective core potentials (RECP|SD) [161] on the others atoms, excluding H atoms (DZVP).

4 Conclusion

The characterization techniques described in this chapter are complementary and lead to a fine investigation of the surface and bulk chemical composition (XPS, WCA, FTIR, RMN, and EDX) as well as the physical properties such as refractive index, thickness and mass density (Ellipsometry, EDX/XRR). In addition, the simulation of XPS BE shifts by DFT calculations strongly supports the experimental XPS spectra and will ensure an accurate surface characterization. Furthermore, the sorption characterization (QCM, Ellipsometry coupled to sorption) allows the study of the materials performance towards the vapours. Therefore, using all of these analyses provides a very high level of structural knowledge of our materials as well as their behaviour towards the VOCs.

The next three chapters will be dedicated to the results achieved during this work divided into three articles. First article concerns the bulk and surface chemical compositions of the organosilicon materials. The second and the third articles discusses the VOCs, especially BTEX sorption performances into the organosilicon materials.

The following chapters will group the ensemble of the results achieved during this work. These results are divided into three chapters in which each chapter represents an article.

The next chapter is dedicated to the results concerning the elaboration of organosilicon materials and their chemical characterization. The aim of this article is to study and compare the bulk and surface chemical composition of the organosilicon materials as a function of the Yasuda parameter W/F *i.e.* the plasma energetic character. The introduction of this article contains a state of the art concerning the chemical composition of organosilicon materials, which is complementary to the summary presented in chapter one. The fine bulk chemical composition investigation was done using ^{29}Si quantitative solid-state NMR and infrared spectroscopy (FTIR). Since the organosilicon surface can contain a wide range of components, our methodology to characterize the surface chemical composition is to combine experimental XPS and DFT calculations. The DFT computations were so used to determine BE energy shifts between the different Si environments. To our knowledge, there is no such attempts in the literature, thus this work will be a step forward in the investigation of the surface composition of organosilicon films. In addition, water contact angle measurements were performed in order to detect the surface hydrophobic character. Accordingly, this chemical composition study would lead us to understand the responses of the materials towards VOCs vapours in further articles.

Chapter 3 (1st article)

This article is published in *Surface and Interfaces*

<https://doi.org/10.1016/j.surfin.2021.101256>

Comparative study of bulk and surface compositions of plasma polymerized organosilicon thin films

Ghadi Dakroub^{1,2}, Thomas Duguet¹, Jérôme Esvan¹, Corinne Lacaze-Dufaure¹, Stéphanie Roualdes², Vincent Rouessac^{2}.*

¹ CIRIMAT, Université de Toulouse, CNRS, INP- ENSIACET 4 allée Emile Monso - BP44362, 31030 Toulouse cedex 4 - France.

² Institut Européen de Membranes, IEM UMR 5635, Univ Montpellier, ENSCM, CNRS, Montpellier, France

ABSTRACT: Plasma polymerized organosilicon thin films were deposited in a MW-PECVD using hexadimethylsiloxane (HMDSO) as a precursor. Thin films were synthesized with different plasma conditions ranging from soft (low plasma energy) to hard (high plasma energy) ones. Quantitative ²⁹Si solid state NMR and FTIR spectroscopy were used to characterize the bulk composition. X-ray photoelectron spectroscopy (XPS) coupled with Density functional theory (DFT) calculations were used to determine the surface chemical composition. The bulk and the surface of the plasma polymerized HMDSO (PP-HMDSO) showed a complex chemical composition. The four main environments M, D, T and Q were present in the films. An additional environment Si(CH₂)(CH₃)₃ denoted S was detected in the PP-HMDSO films. The chemical composition comparison showed a difference between the bulk and the surface of the films. Under soft plasma conditions, a high amount of SiOC₃ termination was present in the bulk of the films. While, the SiO₂C₂ chains were highly present on the surface. On the other hand, under hard plasma conditions, the number of the SiOC₃ termination increased on the surface and decreased in the bulk. Under soft plasma conditions, the PP-HMDSO structure was close to PDMS, while under hard plasma conditions, the PDMS similarity was lost.

KEYWORDS: PECVD, Organosilicon, PDMS, Thin films, NMR, FTIR, XPS, DFT.

Introduction

Among the different precursors mentioned in the literature for plasma enhanced chemical vapor deposition (PECVD), a very wide attention has been given to the organosilicon monomers that allow the deposition of various polysiloxane films, ranging from polymer-like $\text{SiO}_x\text{C}_y\text{H}_z$ to inorganic SiO_2 –like materials [91]. The organic/inorganic balance of the layers depends on the plasma composition [92,105] and the polymerization process conditions, e.g. plasma power and monomer flux [113].

Many monomers can be used for the deposition of Si-containing films, among which the most widely used is hexamethyldisiloxane (HMDSO)[124,162,163]. This monomer shows a great interest because of its high deposition rate, good thermal and chemical stabilities[73], low cost and especially its noticeable safety compared to silanes [99]. HMDSO plasma-polymerized thin films are interesting for biomedical applications[164], optics[165], corrosion protective coatings[166], food and pharmaceutical packaging [167]. Also, they are used in microelectronic industry because of their low dielectric permittivity (low-k)[168], and in vapors and liquids separation, purification and detection [115,134]. In the field of vapors detection, organosilicon membranes have shown a high affinity towards volatile organic compounds (VOCs), and specifically BTEX (benzene, toluene, ethyl-benzene, xylene) [5]. The sorption of gases at the surface as well as their diffusion within the bulk are the two main mechanisms that condition the performances of separation or detection of membranes. Therefore determining the bulk and the surface composition is necessary in order to understand the interaction between BTEX and PECVD organosilicon membranes [169].

The bulk of the plasma polymerized HMDSO (PP-HMDSO) deposits contain a wide range of environments. Therefore, specific characterisation techniques are required to determine the PP-HMDSO bulk chemical composition, such as quantitative ^{29}Si solid state NMR. The environments detected in siloxanes by ^{29}Si solid state NMR are $\text{SiO}(\text{CH}_3)_3$, $\text{SiO}_2(\text{CH}_3)_2$, $\text{SiO}_3(\text{CH}_3)$ and SiO_4 denoted as M, D, T and Q respectively as shown in Figure 20. The corresponding chemical shifts in NMR range between +10 and -110 ppm. In addition, other configurations derived from M, D, T, and Q due to substitution of methyl groups by hydrogen or hydroxyl groups are found in the bulk structure. However, the quantitative NMR characterization of the PECVD deposits is limited due to the sample requirements for the measurement. ^{29}Si solid state NMR require hundreds of milligrams of powder and most PECVD reactors find difficulties to produce this amount under normal conditions. Besides, a long time of deposition to collect enough sample material can change the films chemistry [109–111,113].

In complement, Fourier transform infrared spectroscopy is a well-known characterization to determine the chemical bonds present in the whole thickness of the films.

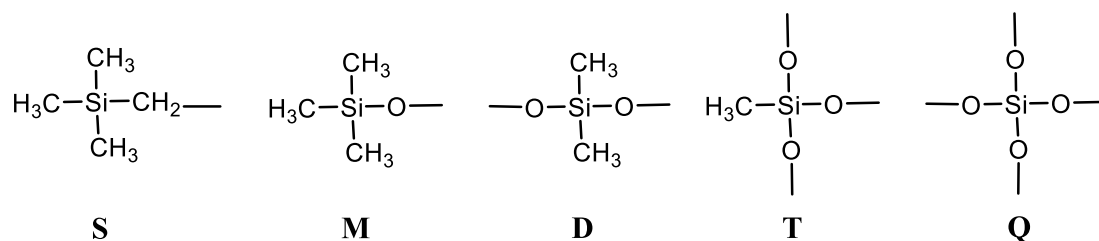


Figure 20: The five environments of silicon atom present in PP-HMDSO

Finally, X-ray photoelectron spectroscopy (XPS) can be very useful for the determination of the surface composition of the films (which can be as complex as the bulk), as long as a great care is taken for spectral decompositions. The curve-fitting of the Si2p core level shows that the PP-HMDSO thin films surface are composed of the M, D, T and Q environments described above in NMR studies. The electron core-level binding energy increases when a methyl group is replaced by an oxygen atom in these environments, following the M, D, T, Q sequence [114]. Unfortunately, the decomposition of Si2p is not straightforward and strongly limited with experimental work alone. In order to decompose the Si2p core level, Alexander et al. [107] used a simple method. First, they measured the positions of D and Q units using polydimethylsiloxane (PDMS) and silica (SiO₂) standards. Secondly, the positions of M and T were estimated by considering that the replacement of a methyl group with an oxygen atom shifts the component position by half of the distance between D and Q. In other words, the four components M, D, T and Q were separated by a constant binding energy shift. They also decided to fix an equal full width at half-maximum (FWHM) for the four environments [92,170]. Other authors decomposed the Si2p peak by using the M,D,T and Q components without mentioning the position of the peaks nor the full width at half maximum (FWHM) [105,171]. Roualdes *et al.* deposited SiO_xC_yH_z thin films using the octamethyltrisiloxane precursor. They added a fifth component at 99.5 eV for films obtained in soft plasma conditions (low power and high monomer flux); this peak (S) could be attributed to SiC₄ (SiC₃ chain termination linked to a methylene bridge) as shown in Figure 20 [113]. On the other hand, O'Hare *et al.* performed a thorough investigation of the binding energy shifts between the four siloxy components (M, D, T, Q). First of all, a homopolymer PDMS standard was characterised by XPS to determine the position of environment D. They further analysed siloxane deposits composed of (D, T) units and (M, Q) units mixtures, with known composition determined by ²⁹Si NMR. The use of these standards enables to identify the binding energy of each siloxy species (M, D, T, Q). As a

result, the difference in the binding energy between each siloxane component is not the same. Thus, the values of M-D, D-T and T-Q are 0.36 eV, 0.68 eV and 0.80 eV, respectively. Eventually, the binding energy increases non-linearly when an oxygen atom replaces a methyl group [114], in contradiction with previous studies [92,107,112].

The simulation of XPS spectra by quantum calculations ensures a theoretical support for the experimental data in order to decompose the core levels. *Duguet et al.* used density functional theory (DFT) calculations to simulate O 1s and C 1s spectra of a poly epoxy polymer composed from diglycidylether of bisphenol A (DGEBA) and ethylene diamine (EDA) molecules. Thanks to the binding energy shifts calculated by DFT they decomposed the O 1s and the C 1s by two and five contributions respectively. As a result, they discriminated phenyl groups from CH₃ bonds, C-OH and a part of C-O-C bonds from other C-O-C bonds [145]. *Gavrielides et al.* worked on the same polymer, they simulated XPS spectra of the C 1s core level using Hartree-Fock calculations. The C 1s core level is decomposed experimentally into three environments i.e, C-C/C-H, C-N and C-O-H/C-O-C. The Hartree-Fock calculations provides the decomposition of the same C 1s core level by nine contributions using calculated binding energy shifts [139]. To our knowledge, there is a lack of attempts to decompose the Si 2p core level for polysiloxanes with S, M, D, T and Q environments using quantum calculations. *Motozaki et al.* calculated the core electron binding energies (CEBEs) of Si containing gas molecules by DFT calculations using the unrestricted generalized diffuse ionization (uGDI) method. Reasonable CEBEs values were obtained with an aged absolute deviation (ADD) value of 0.37. In addition, they calculated CEBEs of Si 2p, O 1s and C 1s for Si containing polymers such as PDMS by deMon-KS DFT calculations. They obtained reasonable differences between the calculated values and experimental ones [147].

In this work, we will present our methodology that combines experiments, chemical characterization and quantum calculations at the atomic scale with the aim to understanding and comparing bulk and surface compositions of the organosilicons. Thin films are deposited by PECVD under various plasma conditions, using HMDSO as precursor. Then, the films are characterized by ellipsometry to determine their thicknesses, Fourier transform-infrared (FTIR) and ²⁹Si Solid-state NMR spectroscopies to determine bulk composition. Finally, XPS combined with density functional (DFT) calculations of theoretical chemical shifts lead to the fine determination of the surface composition.

Materials and methods

Films deposition:

HMDSO plasma polymerized thin films were elaborated in a microwave (MW-) PECVD reactor supplied by Boreal Plasmas (HEF Group). A schematic representation of the reactor is shown in Figure 21. The deposition reactor is a cylindrical chamber, with a limit pressure of 1.10^{-6} mbar. The ECR antennas[148] supply the plasma power in the chamber from a microwave generator (2.45 Hz, Sairem). The applicators are distributed on the top of the chamber, forming a rectangular lattice matrix (3 x 2). This distribution ensures the homogeneity of the discharge and the deposited films [148].

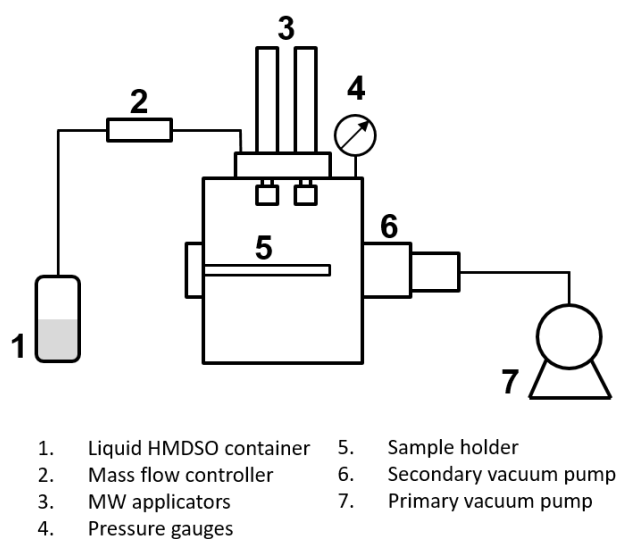


Figure 21: MW- PECVD set-up scheme

The HMDSO precursor (Sigma-Aldrich, $\geq 98.5\%$) was injected into the chamber using a mass flow controller (Brooks) with no dilution or carrier gas. All depositions were performed at room temperature, while the plasma input power W and the monomer flux F were varied from 20 W to 140 W and from 1 sccm to 8 sccm, respectively. The W/F composite ratio represents the energetic character of the plasma. The films were synthesized at different W/F values ranging from “soft” for the lowest W/F values, to “hard” for the highest. This parameter is often described as Yasuda parameter [84]. The deposition conditions of each sample are reported Table 9. The sample names are “WFX”, X being the W/F ratio value.

Table 9: MW-PECVD thin films deposition parameters.

Sample	Plasma power (W)	HMDSO flux (sccm)	W/F	Deposition pressure ($\times 10^{-3}$ mBar)	Thickness (nm)	Average growth rate (nm/min)
WF2.5	20	8	2.5	15.5	308	154
WF5	20	4	5	10.5	337	109
WF10	20	2	10	7.5	351	58
WF20	20	1	20	5.9	242	30
WF40	40	1	40	6.2	395	33
WF70	70	1	70	6.4	314	31
WF140	140	1	140	6.7	257	29

For the quantitative Solid-state ^{29}Si NMR analyses, four samples were prepared (WF2.5 to WF20). These films were deposited on glass substrates and the powder was collected by scrapping the films with a metallic spatula. The deposition times for the WF2.5, WF5, WF10 and WF20 samples were 7, 13, 13, 28 hours, respectively, carried out twice for WF5 and WF10 and three times for WF20. Approximately, 400 mg was collected for each parameters set and packed into a ZrO_2 rotor with a diameter of 7.5 mm.

For all other analytic methods, films were deposited on a (100) p-type silicon wafer (Si-Mat) in all conditions reported in Table 1.

Characterization methods:

Thin films thicknesses were determined by spectroscopic ellipsometry (Semilab GES5E) at atmospheric pressure. The data were collected from 1.2 to 4.5 eV and fitted using a composition of Cauchy transparent dispersion law and a Lorentz absorption term towards the UV range. The results are retained when the fit quality exceeds 0.99 in the full spectral range.

The FTIR absorption spectra were collected between 400 and 4000 cm^{-1} (ThermoFisher IS-50) in transmission mode at room temperature. The background signal (silicon wafer) was subtracted from all the spectra.

Solid State ^{29}Si NMR spectra were recorded on a 300 MHz Varian VNMR300 spectrometer ("Wide Bore" magnet at 7.05 Tesla) using a Varian T3 MAS (Magic Angle Spinning) probe with 7.5 mm ZrO_2 rotors. Spectra were acquired using the quantitative SP technique (Single Pulse) with Magic Angle Spinning and ^1H decoupling. A $\pi/2$ pulse was used with a duration of 6 μs , the recycle delay was chosen to be 60 s and the spinning rate of all the samples was 5 kHz. Q8M8H (octakis(dimethylsiloxy)octasilsesquioxane) was used as a secondary reference (left peak at -2.25 ppm). The width of the spectral window was 50 kHz and the line broadening was

50 Hz. The NMR spectra were fitted using Gaussian/Lorentzian peaks with DMFIT software package.

The XPS analysis were carried out using a Thermoelectron Kalpha apparatus. In order to record the photoemission spectra, Al-K α radiation ($h\nu = 1486.6$ eV) was used from a monochromatized source. The diameter of the spot on the sample surface was 400 μm . We fixed the pass energy at 30 eV for narrow scan and at 170 eV for survey scans. A Shirley background was systematically subtracted. In the end, the photoelectron peaks were analysed and fitted using a combination of Lorentzian and Gaussian peaks in Thermo Advantage software.

Calculation

Density Functional computations were performed to calculate the electron core-level binding energies (BE) of Si atoms that are present in the environments shown in Figure 20 .

Four PP-HMDSO molecules containing the S, M, D, T and Q environments were used as models of subparts of the material. These molecules are presented in Figures S1 to S4 (SI). All geometries were fully optimized in vacuum using conjugate gradients methods. The gradient corrected PBE functional[138] was chosen together with the def2TZVP basis set[152,153] and Grimme's dispersion corrections were added [154,155]. We used the Gaussian 09 package.[156] All the stationary points were characterized as minima by a vibrational analysis and it was followed by a NBO[157] population analysis to determine the atomic charges.

The calculation of Si2p BE was done in a second step within the ΔKS (Kohn Sham) framework using the deMon2k code [158]. Thus, the BE (ΔKS) of electrons of the Si 2p core levels was determined using equation (33):

$$BE(\Delta\text{KS}) = E_{\text{TOTAL}}(\text{Ion}) - E_{\text{TOTAL}}(\text{Neutral}) \quad (33)$$

With $E_{\text{TOTAL}}(\text{Neutral})$ and $E_{\text{TOTAL}}(\text{Ion})$ the total energies of the neutral (initial state) and ionized (final state) molecules, respectively. The ionized molecule has one missing electron on the 2p orbital of the Si atom of interest.

To get these total energies, single point energy calculations were performed using the PBE functional[138], GENA2 auxiliary functions[159], an all electron potential and an augmented basis set (AUG-CC-PVTZ)[160] on the Si atom of interest, and a relativistic basis and effective core potentials (RECP|SD)[161] on the others atoms, excluding H atoms (DZVP).

Results and discussions

HMDSO polymerized FTIR spectra:

Figure 22 shows the FTIR spectra of HMDSO plasma polymerized films deposited with W/F = 2.5, 40 and 140. Strong absorption bands are observed at 2960 cm^{-1} , 2140 cm^{-1} , 1257 cm^{-1} , $1010\text{--}1090\text{ cm}^{-1}$, 840 cm^{-1} and 795 cm^{-1} and a weak absorption band at 1354 cm^{-1} . The absorption bands at 2960 cm^{-1} and at 2140 cm^{-1} correspond to CH_3 stretching and Si-H stretching vibrations, respectively. The absorption band at 1257 cm^{-1} represents CH_3 symmetric bending SiMe_x (Me used as abbreviation for the methyl bond CH_3). The wide band representing Si-O-Si stretching vibrations is composed of two bands present between 1010 cm^{-1} and 1090 cm^{-1} . Also, it can be assigned to Si-O-C asymmetric stretching. Furthermore, the Si- CH_2 -Si absorption band is usually observed at 1080 cm^{-1} – 1040 cm^{-1} , but for oxygen containing coatings this peak is masked by the Si-O-Si band [119,172]. The absorption band at 840 cm^{-1} can be attributed to CH_3 rocking vibrations in SiMe_3 , while the peak at 795 cm^{-1} is referred to CH_3 rocking vibrations in SiMe_2 . The weak absorption band at 1354 cm^{-1} is assigned to CH_2 scissor vibration in Si- CH_2 -Si [92,121,173]. All peaks are summarized in Table 10.

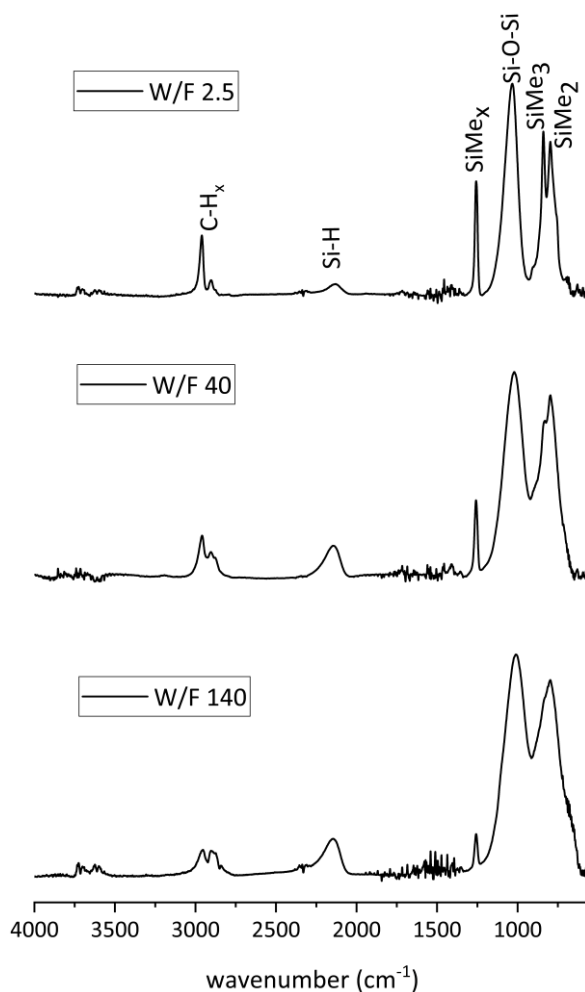


Figure 22: FTIR spectra of pp-HMDSO films deposited at different W/F values.

We observe a decrease in the intensity of the bands present at 2960 cm^{-1} , 1257 cm^{-1} , and 840 cm^{-1} while increasing the W/F value from 2.5 W/sccm to 140 W/sccm . This modification results from the decrease in the number of CH_3 bonds. We assume that the significant amount of hydrocarbons bonds present at small W/F values (soft plasma conditions) is due to the low monomer fragmentation. Whereas the decrease in the CH_3 bands intensities and the simultaneous increase of the Si-H absorption band intensity at 2140 cm^{-1} at higher W/F values (hard plasma conditions), is due to the higher monomer fragmentation. This result is consistent with the work of Sonnenfeld et al[174] who explained the loss of carbon containing groups by the increase of monomer fragmentation at higher plasma specific energy.

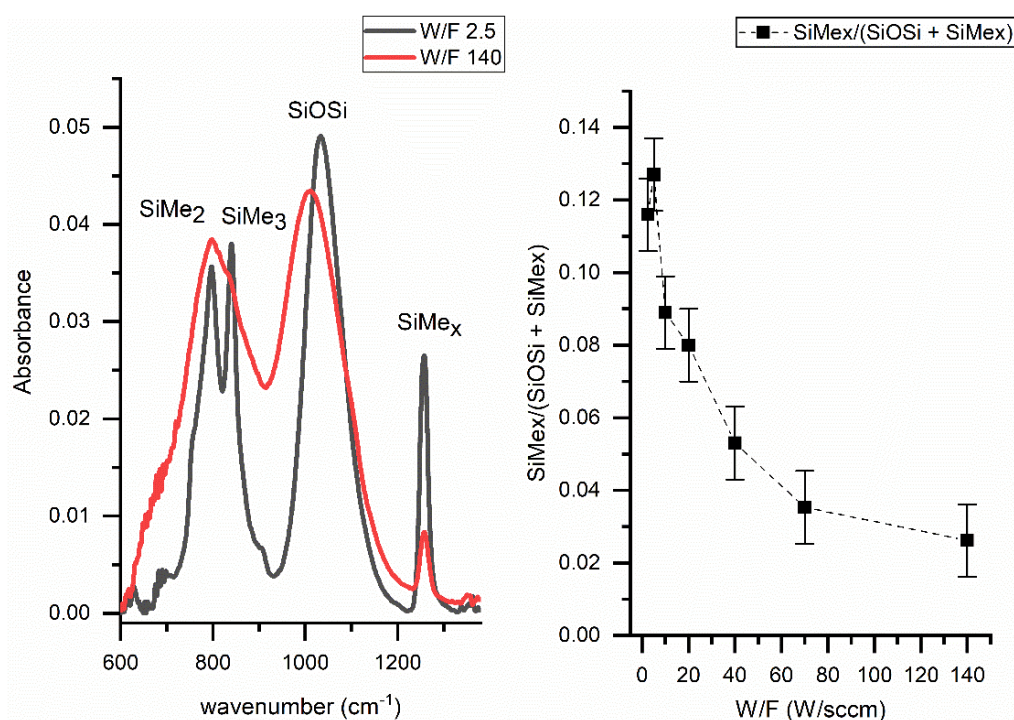


Figure 23: a) The FTIR spectra of WF2.5 and WF140 b) PDMS-like rate ($\text{SiMe}_x/(\text{SiOSi} + \text{SiMe}_x)$) of the films deposited at different W/F values.

Figure 23a shows a focused comparison of WF2.5 and WF140 infrared spectra, in the finer range $600\text{--}1400\text{ cm}^{-1}$. A broadening and a shift of the SiOSi peak are observed while depositing under harder plasma conditions (140 W/sccm). This band modification is possibly due to the increase of the Si-O-C band intensity near 965 cm^{-1} . Sonnenfeld et al assigned the absorption band near 943 cm^{-1} in the FTIR spectra of a plasma polymerized TEOS to Si-O-C symmetric stretching in Si-O- CH_2 . In fact, under hard plasma conditions, the high fragmentation induces the introduction of carbon atoms in the Si-O-Si skeleton forming molecules containing Si-O-Si chains coupled with hydrocarbon branching. This molecules formation makes the skeleton chains more rigid explaining the shift of the SiOSi/SiOC band to lower wavenumber values

(from 1032 cm^{-1} to 1010 cm^{-1}). In addition, the presence of the Si-CH₂-Si bonds at higher W/F values is possible since the FTIR spectra of the deposition from hexamethyldisilane reveal a broad band at 1020 cm^{-1} that has been attributed to Si-CH₂-Si bridge, previously.[106]

Table 10: FTIR absorption bands of PP-HMDSO films

Chemical bond and vibration mode	Band position (cm^{-1})	References
CH₃ rocking in SiMe₃	760	[91] [119] [108]
CH₃ rocking in SiMe₂	795	[91][92] [148] [119] [175] [106]
CH₃ rocking in SiMe₃	840	[91] [92] [148] [119] [175] [106]
Si-O stretching Si-OH / Si-C stretching in SiMe₂	902	[91] [119] [175]
Sym. Si-O-C stretching	965	[108][174]
Si-O stretching in SiOSi	1010-1090	[91] [92] [148] [119] [173] [175] [106]
CH₃ sym. bending in SiMe_x	1257	[91] [92] [148] [119] [173] [106]
Si-H stretching	2140	[91] [92] [175] [106]
CH₃ sym. Stretching	2900	[91] [92] [175] [106]
CH₃ asym. Stretching	2960	[91] [92] [175] [106]

The SiMe_x/(SiOSi + SiMe_x) ratio, i.e. the area of the SiMe_x band divided by the sum of the areas of SiOSi and SiMe_x bands, is defined as the *PDMS-like rate*, and shown in Figure 23b. The areas of the peaks were calculated by peak decomposition of the infrared spectra using Labspec software. The uncertainty on the PDMS-like rate value, due to peak broadening or peaks superposition is taken as the standard deviation over three repeated syntheses of each sample. The decrease of the PDMS-like rate with increasing W/F proves that the character of the films synthesized under soft conditions is closer to PDMS than the films prepared under hard conditions. In fact, under hard conditions, the chemical and structural disorder due to the introduction of Si-O-C, Si-CH₂-Si and Si-H bonds is responsible for the loss of the PDMS character.

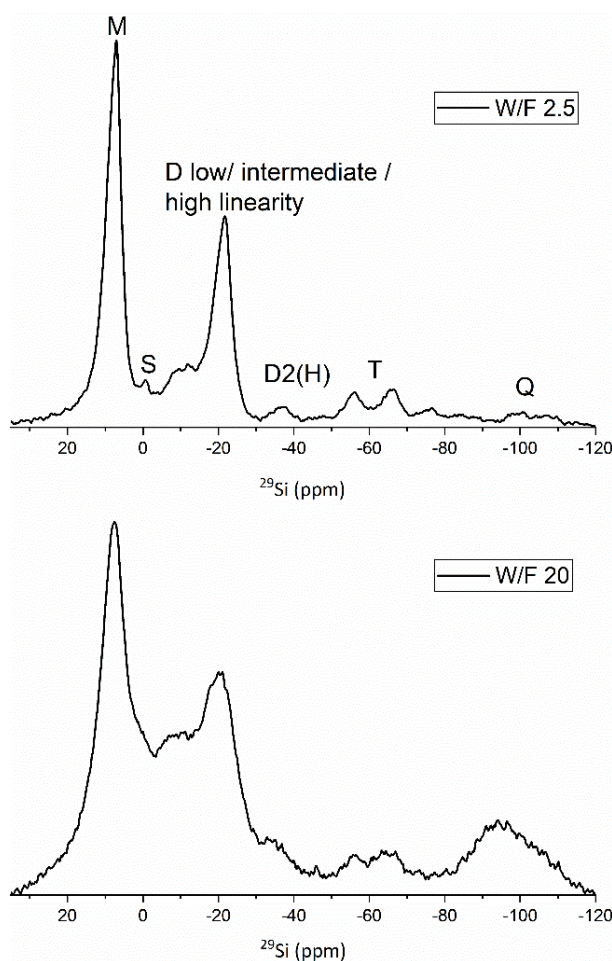
^{29}Si NMR spectra:

Figure 24: ^{29}Si NMR spectra of PP-HMDSO films deposited at 2.5 W/sccm and 20 W/sccm.

In order to get a deeper knowledge of the bulk composition and structure, thin films were characterized by quantitative ^{29}Si solid state NMR. The ^{29}Si NMR spectra of the PP-HMDSO deposited at 2.5 W/sccm and 20 W/sccm are shown in Figure 24. The spectra consist of 15 resonance lines listed in Table 11 that correspond to different environments distinguished by their oxidation state, i.e. M for $\text{SiO}(\text{CH}_3)_3$, D for $\text{SiO}_2(\text{CH}_3)_2$, T for $\text{SiO}_3(\text{CH}_3)$ and Q for SiO_4 . An additional environment S appears around 0 ppm, it can be referred to SiC_4 which is likely a SiC_3 termination bonded to CH_2 bridge. Table 11 also shows the presence of different peaks grouped in the same environment category; this is due to the change in the crosslinking degree or the substitution of methyl by hydrogen and hydroxyl groups.

Table 11: Positions and percentages of the environments in the PP-HMDSO deposited at different W/F value.

	WF2.5		WF5		WF10		WF20	
	$\delta(^{29}\text{Si})/\text{ppm}$	Percentage (%)	$\delta(^{29}\text{Si})/\text{ppm}$	Percentage (%)	$\delta(^{29}\text{Si})/\text{ppm}$	Percentage (%)	$\delta(^{29}\text{Si})/\text{ppm}$	Percentage (%)
M1- Si(OSi)C₃	8.9	27.4	9.0	20.3	11.4	14.7	13.7	5.4
M1- Si(OSi)C₃	6.9	19.0	6.9	20.4	7.7	28.2	7.7	28.2
S – Si(CH₂)C₃	-0.8	0.9	-0.4	2.1	0.0	3.3	0.6	4.3
D2 - Si(OSi)₂C₂ Low linearity	-10.6	11.8	-8.6	10.4	-9.0	16.0	-8.0	15.6
D2 - Si(OSi)₂C₂ Intermediate linearity	-18.9	10.0	-18.9	14.2	-18.9	14.7	-18.9	15.9
D2 - Si(OSi)₂C₂ High linearity	-22.1	15.2	-22.1	10.2	-22.1	6.7	-22.1	7.0
D2(H) Si(OSi)₂CH	-37.0	1.3	-36.7	2.2	-34.5	2.6	-34.8	3.5
T1 Si(OSi)(OH)₂C	-46.9	0.4	-46.7	0.6	-47.7	0.7	-46.1	0.4
T2 Si(OSi)₂(OH)H	-56.0	3.9	-55.9	2.7	-55.2	2.9	-55.6	2.2
T3 - Si(OSi)₃C	-65.8	4.6	-65.7	3.5	-65.1	4.8	-64.9	3.3
T3(H) Si(OSi)₃ H	-76.0	1.7	-76.5	1.6	-75.8	0.4	-76.5	1.3
Q1 Si(OSi)(OH)₃	-83.6	0.8	-82.2	0.1	-82	0.6	-85.7	1.2
Q2 Si(OSi)₂(OH)₂	-88.3	0.5	-92.4	7.3	-92.9	3.0	-91.8	4.3
Q3 Si(OSi)₃OH	-99.5	1.6	-97.5	0.3	-98.8	0.1	-98.2	4.5
Q4 - Si(OSi)₄	-107.2	0.9	-104.5	4.1	-104.4	1.3	-106.3	2.9

The variation of the environments percentages with the increase of W/F from 2.5 W/sccm to 20 W/sccm is shown in Table 11 and Figure 25a. The monotonic decrease of the M environment from 46% to 33%, reveals that the number of Si-(CH₃)₃ chain terminations is reduced with the augmentation of W/F. On the other hand, the increase of the S component from 1% to 4% proves that the number of the Si-CH₂ bonds is more important at higher W/F values. Also, the slight growth of the D2(H) peak intensity observed in Figure 24 confirms the increase of the Si-H bonds in the PP-HMDSO deposits at greater W/F values. These variations validate that under soft plasma conditions, the monomer fragmentation is low causing the preservation of the Si-(CH₃)₃ bonds in the bulk of the films. The increase of W/F values leads to the enhancement of the monomer fragmentation, giving rise to the Si-H and Si-CH₂ bonds as previously demonstrated in the FTIR section.

Three different D2 peaks are found that we presumably attribute to the more or less linear character of the D chains (high, intermediate, low). In fact, the linearity of the SiO₂C₂ chains is

linked to the fragmentation degree of the monomer. The SiO_2C_2 linear chains are flexible and similar to the PDMS polymer chains, while the low and intermediate SiO_2C_2 chains are mostly folded, which explains their low linearity and their dissimilarity with PDMS.

Figure 25b illustrates a remarkable drop of the percentage of the highly linear SiO_2C_2 component in addition to an important increase in the percentages of the chains with intermediate and low linearity while expanding W/F from 2.5 to 20 W/sccm. These evolutions demonstrate that PP-HMDSO films deposited under soft conditions are close to the conventional PDMS polymer. The low percentage of the T and Q environments compared to the M and D units indicates that the deposits character is highly organic. Indeed, these depositions were performed under soft conditions ($\text{W/F} = 2.5$ to 20 W/sccm) and without oxygen as dilution gas.

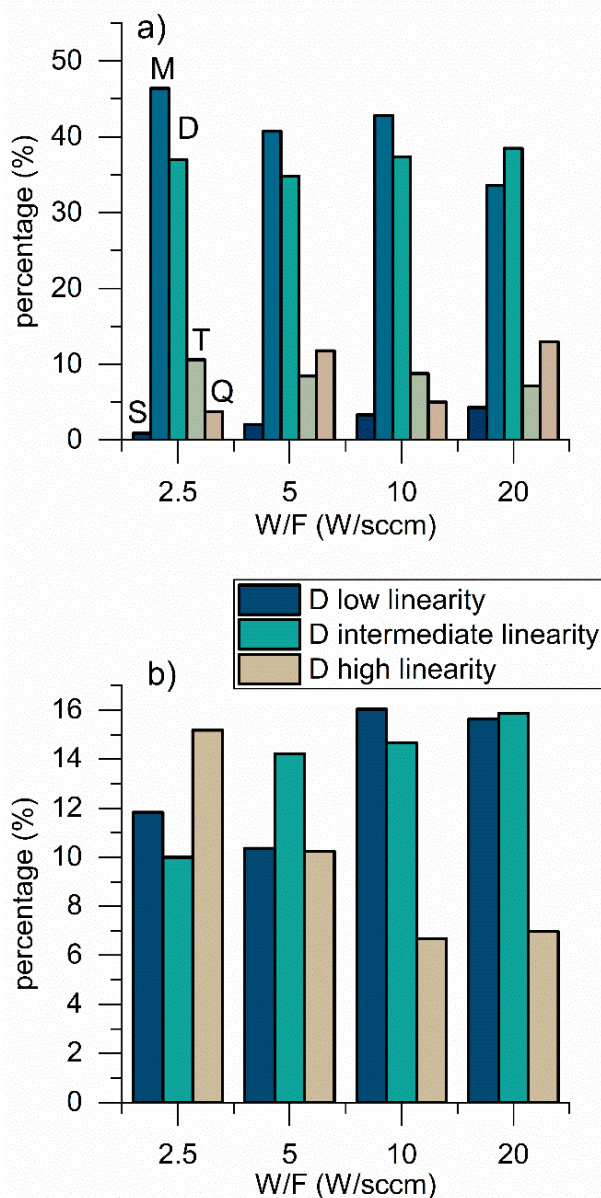


Figure 25: (a) NMR environments percentages of the films at different W/F (b) The percentages of the low linearity D (navy blue), intermediate linearity D (light blue) chains, and high linearity D (grey) chains at different W/F values.

X-ray photoelectron spectroscopy:

The BE of the Si 2p electrons, calculated in the Δ KS framework using equation (33) defined in the computational section above, are presented in Table 4, for the five environments S, M, D, T and Q. The m and m2 indices on some environments serves to differentiate them (see Table 4). Two additional environments were added in molecular models that corresponds to $(\text{CH}_3)_2\text{-Si-H}_2$ and $\text{H}_2\text{-Si-O}_2$. The Si-O, Si-C, Si-H, C-C and C-H bonds lengths are in good agreement with the experimental ones available in the literature (Table S7 annex 1) [176,177]. In order to decompose the peaks of the Si 2p experimental spectra, binding energy differences ($\Delta\text{BE}_{\Delta\text{KS}}$) between the environments are used. The S environment was considered as reference for all the

BEs because of its lowest binding energy, therefore at this environment $\Delta BE_{\Delta KS} = 0$. The $\Delta BE_{\Delta KS}$ calculated are compared to binding energy differences between similar environments in ref.[147]. The ΔBE s values obtained for M-S, D-M, T-D and Q-T in ref. [147] were 0.57, 0.36, 0.42 and 0.62 respectively. Thus, the $\Delta BE_{\Delta KS}$ values calculated by DFT agree quite well with the ones found in ref.[147].

The calculated charge of Si atoms (Q_{Si}) increases with the number of Si-O bonds, leading to an increase in the binding energy of the Si 2p electrons. A good linear fit is obtained in the form of $\Delta BE_{\Delta KS} = 0.26 \times Q_{Si} + 1.76$ ($r^2 = 0.85$). Nevertheless, the charge of the two environments SiH_2C_2 and SiH_2O_2 does not follow this evolution. This is due to the neighbouring Si atoms that affect the charge of the Si atom of interest in these environments. The calculated ΔBE s presented in column 6 Table 12 indicate that there is a non-linear increase in the binding energy when an oxygen replaces a methyl, in accordance with ref.[114]. These $\Delta BE_{\Delta KS}$ are then used to decompose the experimental XPS Si 2p core levels, as explained in the following.

Table 12: Si 2p BE, ΔBE (the reference is the S environment) values and Si NBO atomic charges determined from DFT calculations.

	Environment	BE (ΔKS) (eV)	Standard deviation	$\Delta BE_{\Delta KS}$ (eV)	$\Delta BE_{\Delta KS}$ environment	Charge Q_{Si} (e)	Standard deviation
S = SiC ₄	SiC ₄	107.74		0.00		1.81	
	SiC ₄	108.14		0.40		1.78	
		107.94	0.20	0.20	0.00	1.80	0.02
SiH ₂ C ₂	SiH ₂ C ₂	107.97		0.00		1.16	
M = SiOC ₃	SiOC ₃	108.49		0.75		1.97	
	SiOC ₃	108.49		0.76		1.98	
	SiOC ₃ m	108.61		0.87		2.01	
	SiOC ₃	108.65		0.91		1.98	
	SiOC ₃	108.67		0.94		1.98	
	SiOC ₃ m2	108.69		0.95		2.03	
	SiOC ₃	108.78		1.04		1.98	
	SiOC ₃	108.79		1.06		1.98	
	SiOC ₃ m	108.84		1.10		2.00	
	SiOC ₃	108.86		1.13		1.98	
	SiOC ₃	108.86		1.13		1.97	
	SiOC ₃	108.90		1.16		1.98	
	SiOC ₃	108.92		1.19		1.98	
		108.74	0.12	1.00	M-S = 0.80	1.99	0.01
D = SiO ₂ C ₂	SiO ₂ C ₂	108.70		0.96		2.20	
	SiO ₂ C ₂	109.00		1.27		2.20	
	SiO ₂ C ₂	109.10		1.37		2.16	
	SiO ₂ C ₂	109.11		1.37		2.16	
	SiO ₂ C ₂	109.15		1.41		2.16	
	SiO ₂ C ₂	109.17		1.43		2.16	
	SiO ₂ C ₂ m2	109.21		1.48		2.18	
	SiO ₂ C ₂	109.21		1.48		2.16	
	SiO ₂ C ₂	109.25		1.51		2.15	
	SiO ₂ C ₂	109.25		1.51		2.16	
	SiO ₂ C ₂	109.27		1.53		2.18	
	SiO ₂ C ₂	109.27		1.53		2.16	
	SiO ₂ C ₂	109.39		1.65		2.16	
	SiO ₂ C ₂ m	109.54		1.80	D-M = 0.45	2.20	

		109.19	0.13	1.45		2.17	0.02
SiO ₂ H ₂	SiO₂H₂	109.57		0.00		1.63	
T = SiO ₃ C	SiO ₃ C	109.45		1.71		2.31	
	SiO ₃ C	109.84		2.10		2.30	
	SiO ₃ C	109.97		2.23		2.30	
		109.75	0.20	2.01	T-D = 0.56	2.30	0.00
Q = SiO ₄	SiO ₄	110.29		2.55		2.44	
	SiO ₄	110.37		2.63		2.43	
		110.33	0.04	2.59	Q-T = 0.58	2.43	0.00

Figure 26 shows the fitted Si 2p core levels for WF2.5, WF40 and WF140. All the Si 2p peaks were fitted with DFT S, M, D, T and Q components. The FWHM was fixed at 1.1 eV for all components. We used a PDMS conventional polymer as reference for the SiO₂C₂ (D) environment and the calculated $\Delta E_{\Delta KS}$ to fix the BE of the components. A good fit to the Si 2p experimental envelope was obtained except for the low-BE side of the peak. The high BE value of S as compared to the value found in *Roualdes et al.* [113] can originate from the choice of the shape of the component S (fixed like others), or to the lack of an additional unknown contribution.

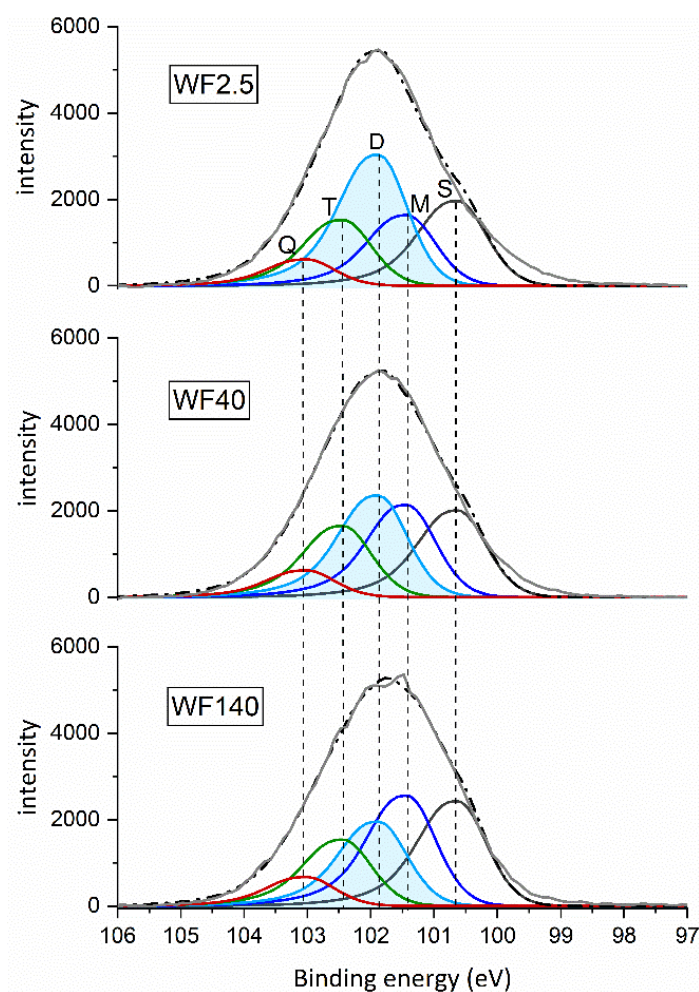


Figure 26: The decomposed Si 2p core level of WF2.5, WF40, and WF140. Dotted line = experimental envelope, full line = calculated envelope.

The decomposition procedure of the Si 2p core levels is described hereafter. First, a PDMS homopolymer was used as a reference for the correct positioning of the SiO₂C₂ (D) environment. In this sample, the PDMS O 1s core level exhibits a single oxidation state and is therefore used for charge correction. It is fixed at BE = 532.0 eV as advised by Beamson and Briggs [178]. The same charge correction value was used to adjust the binding energy of the pure D Si 2p envelope, resulting in BE (D) = 101.88 eV. In addition, Si 2p_{3/2} and Si 2p_{1/2} components were used to fit the PDMS Si 2p core level with an equal FWHM, and an area ratio of 2:1. A good fit is obtained with an energy separation of 0.67 eV, in accordance with reference work [114,178]. We then modelled the synthetic peak that encompasses the Si 2p_{3/2} and Si 2p_{1/2} doublet (with asymmetry parameters), and used these parameters to model all environments in the Si 2p fitting procedures. Finally, since the O 1s peak could not be used as a reference anymore because of the multiple environments of O atoms in unknown PP-HDMSO films, the position of the D component was fixed at 101.88 eV with regards to the maximum of the C 1s peak (fixed at 284.5 eV). Other components (S, M, T, and Q) positions are constrained by DFT calculated chemical shifts filled in the fitting procedure, and summarized in Table 12. Intensities were left free to fit. The positions of the S, M, D, T and Q components extracted from the decomposition procedure of the experimental spectra are shown in Table 13 and Figure 26.

Table 13: Binding energy of the various units present in Si 2p core level.

Environments	Binding energy (eV)
S (SiC₄)	100.6
M (SiOC₃)	101.4
D (SiO₂C₂)	101.9
T (SiO₃C)	102.4
Q (SiO₄)	103.0

The evolution of the environments percentages while increasing W/F is shown in Figure 27. The percentage of SiO₂C₂ (D) environment, which represents the conventional PDMS polymer, decreases from 34.6 % to 21.4 % while increasing W/F. However, the M percentage evolves from 18.6 % to 28 % illustrating the augmentation of SiOC₃ chain termination on the surface with increasing W/F values. These variations confirm that under soft plasma conditions, the low fragmentation leads to the preservation of the SiO₂C₂ environments on the surface i.e. the PP-HMDSO films are closer to PDMS. On the contrary, under hard plasma conditions, the high fragmentation results in a higher concentration of SiOC₃ terminations on the surface, and

the loss of the PDMS structure. The SiOC_3 component can be also assigned to $-\text{CH}_2-\text{Si}-(\text{CH}_3)_2-$ bonds. These bonds formation is due to the introduction of carbon atoms in the SiOSi chains at hard plasma condition as shown in FTIR and RMN sections. In addition, Table 14 illustrates the evolution of the Si 2p, C 1s, and O 1s core levels FWHM while increasing W/F. The increase in the FWHM of the three core levels confirms the formation of new bonds on the surface such as $\text{CH}_2-\text{Si}-(\text{CH}_3)_2$, Si-H, Si-O-C and Si-OH, leading to some disorder in the chains formation. In both cases, the result is a loss of the PDMS-like character.

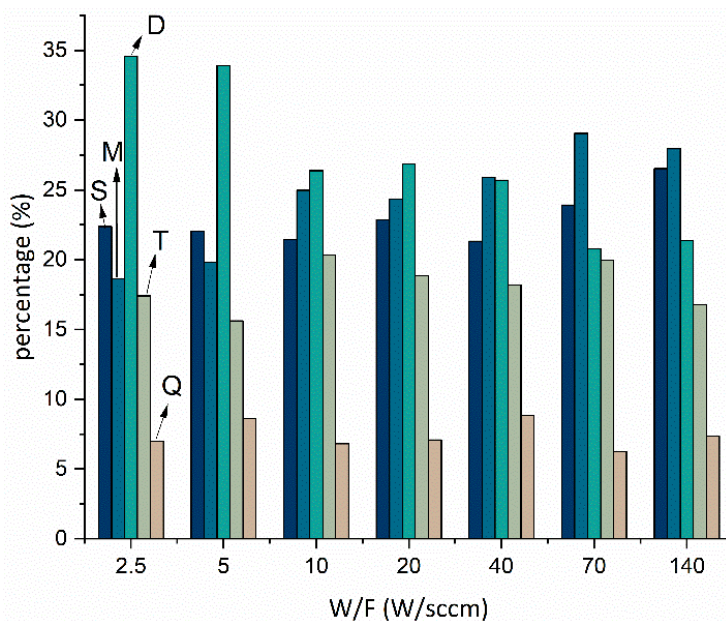


Figure 27: The percentages of S, M, D, T and Q components at different W/F values.

The high concentration of CH_3 bonds and the low quantity of SiO_4 units indicate that all the deposits are organic. This can explain the low binding energy value of the SiO_4 (Q) environment compared to the binding energy of inorganic silica (103.2 eV for our reference, not shown). Besides, the SiO_4 component can be referred to $\text{Si}(\text{OSi})_x(\text{OH})_{4-x}$ environments. These hydroxyl groups formation induces the loss of the inorganic $\text{Si}(\text{OSi})_4$ sites causing the shift of the binding energy to lower values, and they are identified by RMN in the present study (see Q1-3 in Table 11).

Table 14: The evolution of the FWHM of Si 2p, C 1s, and O 1s core levels with W/F.

W/F (W/sccm)	FWHM		
	Si 2p	C 1s	O 1s
2.5	2.18	1.52	1.51
5	2.20	1.56	1.52
10	2.29	1.70	1.61
20	2.31	1.80	1.60
40	2.31	1.83	1.68
70	2.35	1.90	1.64
140	2.43	1.97	1.65

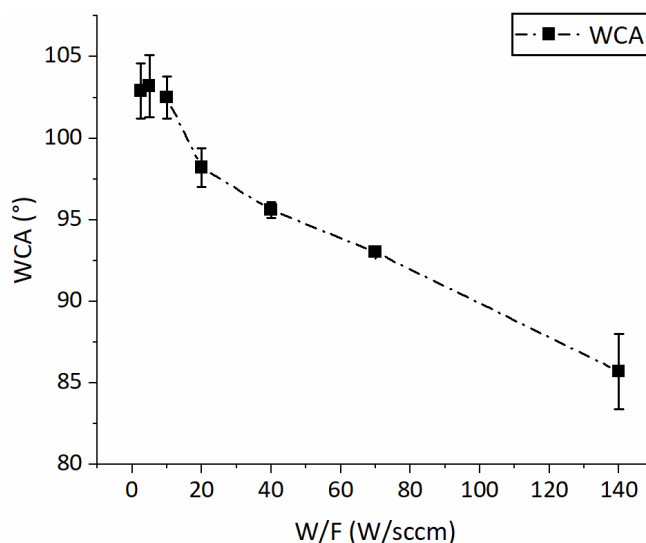
Water contact angle (WCA):

Figure 28: WCA measurements for PP-HMDSO thin films at different W/F values

Figure 9 shows the water contact angle (WCA) of all the PP-HMDSO thin films. The error on each value is deducted from the standard deviation over six repeated measurements. The WCA values for the PP-HMDSO films are higher than 90° except the film deposited at 140 W/sccm that reveals a lower WCA angle value (85.7°) but yet still close to 90° . Therefore, the hydrophobic character is dominant on all the PP-HMDSO film despite the WF140 deposit that shows relatively a low WCA value and can be considered as weakly hydrophobic. Indeed, as shown in the sections above all the deposits are considered organic due to the high amount of CH₃ bonds and the low quantity of SiO₄ components present in the films. Despite the films hydrophobicity, the contact angle value decreases while increasing W/F from 2.5 W/sccm to 140 W/sccm. This WCA change can be justified by the disorder occurred in the bonds formation while increasing W/F. In fact, the decrease of the Si-CH₃ terminations amount and the formation of new bonds such as Si-H, Si-OH and Si-O-C can reduce the WCA value.

Surface and Bulk comparison:

The FTIR, RMN and XPS analyses showed a difference in the composition between the bulk and the surface of the deposited films. At soft plasma conditions, the FTIR and RMN analyses showed an important amount of SiOC₃ termination in the bulk of the prepared films. In addition, the linear SiO₂C₂ chains that are close to chains found in conventional PDMS are present in high concentration in the bulk. While the XPS analysis indicates that the number of SiO₂C₂ environment is larger than the amount of SiOC₃ component on the surface.

On the other hand, at high plasma conditions, the amount of SiOC_3 units decreases while the number of Si-H and $\text{Si-CH}_2\text{-Si}$ bonds increases in the bulk. In addition, the amount of the linear SiO_2C_2 chains is lower at higher W/F values. XPS analyses showed a disorder in the bonds formation in addition to an augmentation of the SiOC_3 component and a decrease in the SiO_2C_2 unit on the surface.

As a conclusion, under soft plasma conditions, the low fragmentation of the monomer preserve the $\text{Si-(CH}_3)_3$ termination groups and promote the polymerization of linear SiO_2C_2 chains in the bulk and on the surface [174]. This structure elevates the flexibility of the chains and the formation of free volumes in the polymer network. Thus, this chemical composition gives the PP-HMDSO films a structure close to conventional PDMS. On the contrary, under hard plasma conditions, the high fragmentation of the monomer favours the formation of random bonds leading to a cross-linked network, more rigid with little amount of free volumes. Therefore, a formation of Si-H , Si-O-C , $\text{Si-CH}_2\text{-Si}$ bonds and a change in the SiO_2C_2 structure are shown in the material bulk. Also, the growth of the material network induces an increase of the SiOC_3 concentration on the surface.

Conclusion

We have presented an investigation of the PP-HMDSO thin films bulk and surface chemical compositions. The films were prepared in a MW-PECVD reactor under different plasma conditions ranging from “soft” (i.e. low HMDSO fragmentation) to “hard” (i.e. higher HMDSO fragmentation). Specific characterisation techniques were used to determine the bulk composition such as ^{29}Si quantitative solid-state NMR and FTIR spectroscopy. A combination between X-ray photoelectron spectroscopy (XPS) and DFT calculations was used to determine the surface chemical composition. The chemical composition comparison showed a difference between the bulk and the surface of the films. Under soft plasma conditions, a high amount of SiOC_3 termination is present in the bulk of the films. In addition, the linear SiO_2C_2 chains that are close to PDMS chains are present in high concentration in the bulk of the prepared films. While the concentration of the SiO_2C_2 chains is higher than the number of the SiOC_3 component on the surface. On the contrary, under hard plasma conditions, the concentration of the SiOC_3 termination decreases while the amount of Si-H and $\text{Si-CH}_2\text{-Si}$ bonds increases in the bulk. In addition, the linear SiO_2C_2 chains decreases in the bulk at hard plasma conditions. On the surface, the number of SiOC_3 unit increases and the amount of the linear SiO_2C_2 chains decreases. The PP-HMDSO deposited under soft conditions shows a high PDMS-like rate, while the PP-HMDSO prepared under hard plasma conditions shows a disorder in the bonds

formation. The study of the bulk and surface chemical compositions of the PP-HMDSO thin films, contributes to the understanding of the sorption phenomena of VOC vapors (especially for BTEX), on organosilicon membranes that will be analyzed and presented in a future article.

Appendix A. Supporting Information

Images of the simulated molecules using Gabedit ref. 1 in SI.

Validation of the molecular simulation by comparing bond lengths with experimental data.

Corresponding Author

*Corresponding Author Email: vincent.rouessac@umontpellier.fr, Tel. +33. (0) 4 67 14 91 45

Acknowledgements

This work was granted access to the HPC resources of CALMIP supercomputing center under the allocation 2019- 2020 [p1526]. It was also supported by the French Carnot Institute *Chimie Balard Cirimat* (PhD grant #ENSCM2018.2021-IEM/PETAB/2018-030).

Annex 1: Supplementary Information of article 1 (chapter 3)

Comparative study of bulk and surface compositions of plasma polymerized organosilicon thin films

Ghadi Dakroub^{1,2}, Thomas Duguet¹, Jérôme Esvan¹, Corinne Lacaze-Dufaure¹, Stéphanie Roualdes², Vincent Rouessac^{2}.*

¹ CIRIMAT, Université de Toulouse, CNRS, INP- ENSIACET 4 allée Emile Monso - BP44362, 31030 Toulouse cedex 4 - France.

² Institut Européen de Membranes, IEM UMR 5635, Univ Montpellier, ENSCM, CNRS, Montpellier, France

Supplementary images:

Density Functional computations were performed to calculate the electron core-level binding energies (BE) of Si atoms. The calculations included 2 steps.

Step 1 : Full optimization of the geometry of the molecules within the PBE-D3/def2TZVP level of theory using the Gaussian 09 package. All the stationary points were characterized as minima by a vibrational analysis. The optimized geometries are presented in Figure S1 to S4. All the figures were obtained using Gabedit software [179].

Step 2 : Single point energy calculation of Si2p BE within the Δ KS (Kohn Sham) framework using the deMon2k code. PBE functional, GENA2 auxiliary functions, all electron potential and an augmented basis set (AUG-CC-PVTZ)[160] on the Si atom of interest, and relativistic basis and effective core potentials (RECP|SD)[161] on the others atoms, excluding H atoms (DZVP).

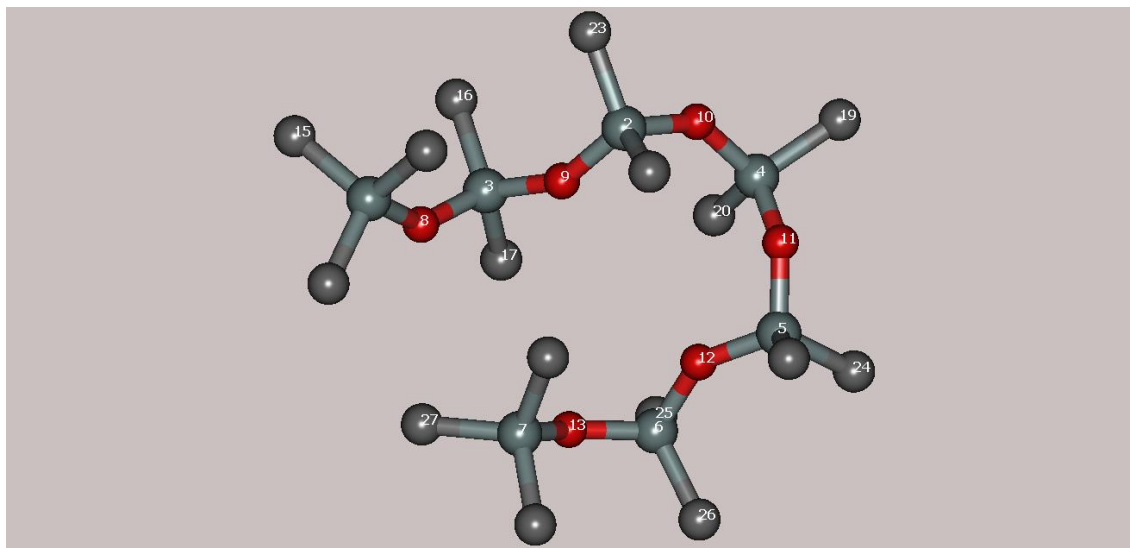


Figure S29: TPDMS molecule.

The true PDMS molecule (TPDMS) shown in Figure S29 represents a short conventional PDMS polymer chain. This molecule contains two SiOC_3 (M) environments (chain terminations) and five SiO_2C_2 (D) environments.

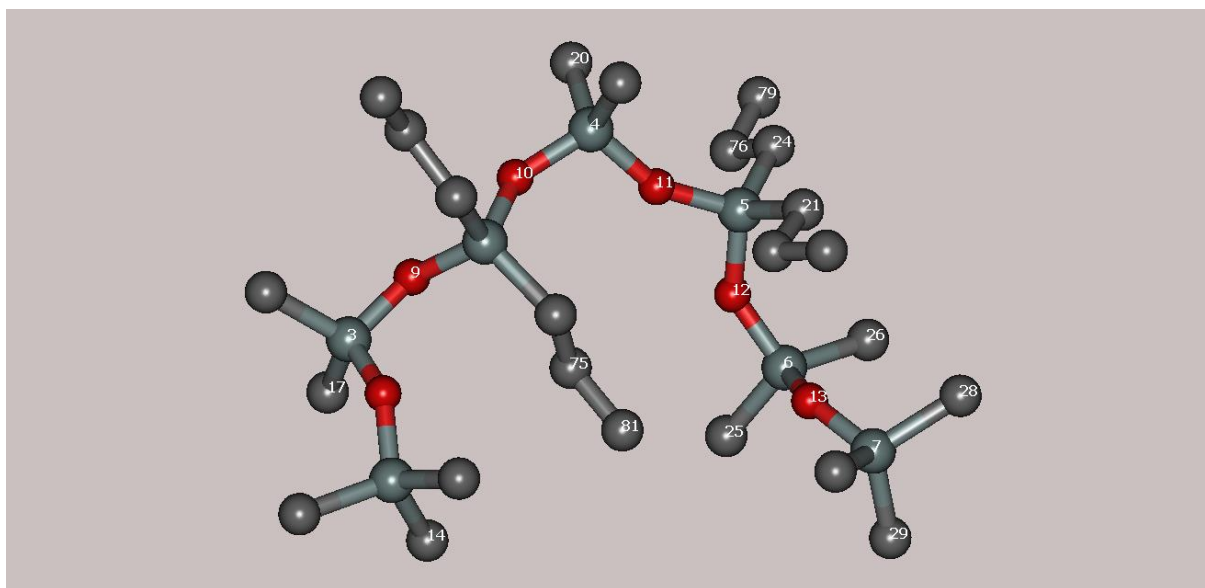


Figure S30: MPDMS molecule.

The modified PDMS molecule (MPDMS) shown in Figure S30 represents a PDMS chain with a $-\text{CH}_2-\text{CH}_2-\text{CH}_3$ bond on two SiO_2C_2 (D) environments.

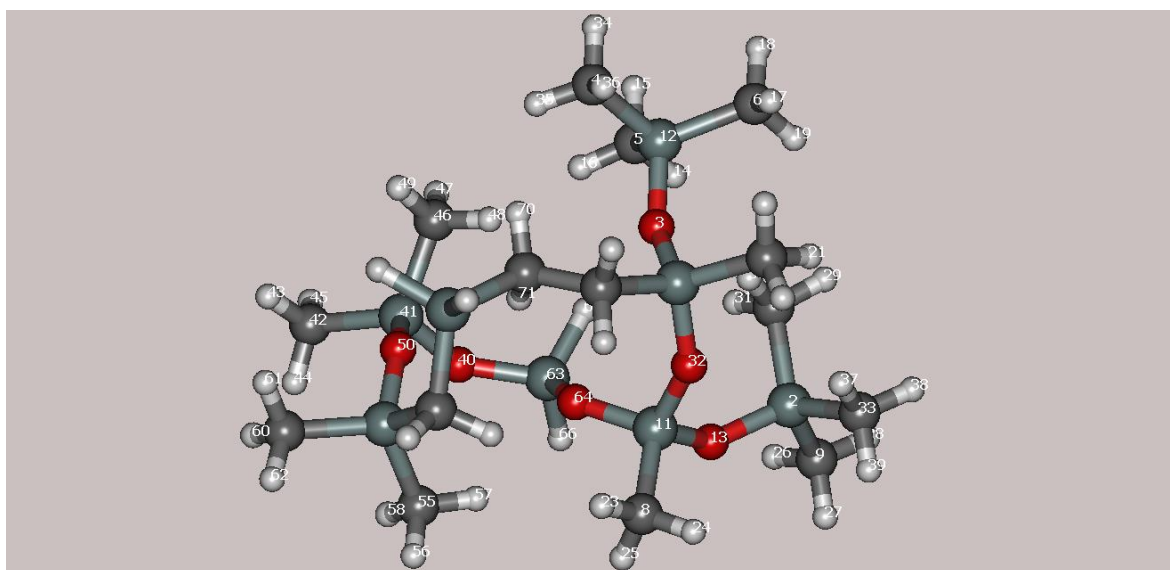


Figure S31: PDMS plasma molecule.

The PDMS plasma molecule shown in Figure S31 tentatively represents a plasma polymerized organosilicon molecule. This molecule contains three M environments, two D environments and one SiO_3C (T) environment. Two additional environments are also shown in this molecular model that corresponds to $(\text{CH}_3)_2\text{-Si-H}_2$ and $\text{H}_2\text{-Si-O}_2$ (Table S16 in SI).

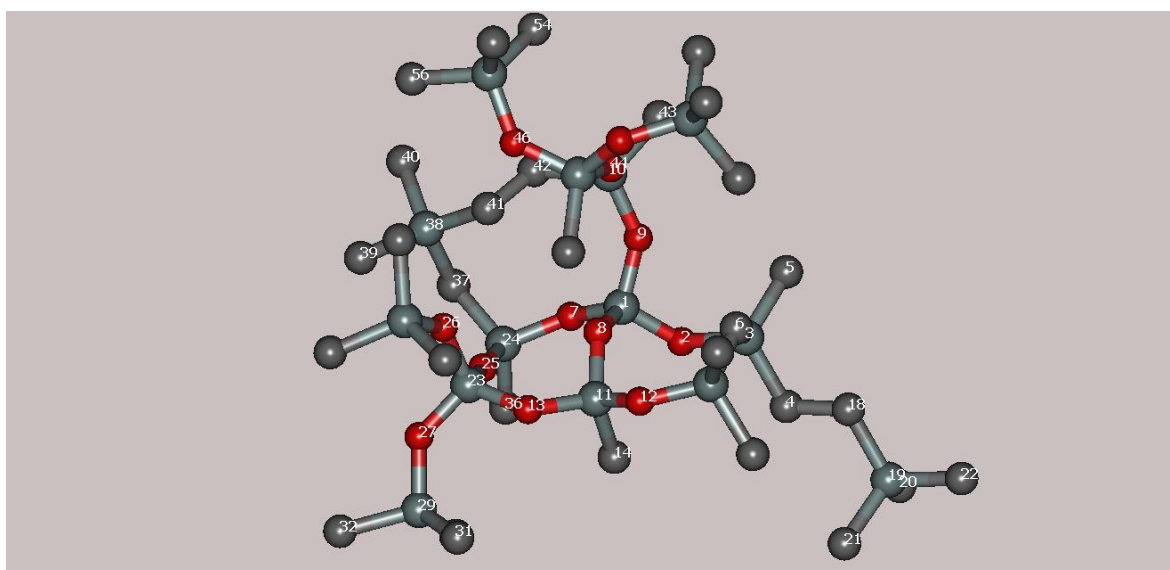


Figure S32: NPP molecule.

Another Plasma polymerized organosilicon molecule is shown in Figure S32. This large molecule contains the four siloxy environments M, D, T and Q (SiO_4) in addition to two S environments (SiC_4).

Supplementary Tables:

Table S15: The calculated bonds lengths in the four molecules compared to the values found in the literature

	Bonds lengths (Å)		References
	Calculated values	Literature values	
Si-O	1.64-1.68	1.613 - 1.66	[176][180]
Si-CH₂	1.87 – 1.91	1.87 – 1.90	[177]
Si-CH₃	1.88 – 1.90	1.85 – 1.92	[180] [181]
Si-H	1.50	1.48 – 1.51	[177][180]
C-C	1.54 – 1.55	1.54	[176]
C-H	1.10 – 1.12	1.10	[176][180]

Table S15 shows a comparison between the calculated lengths of the bonds present in the four simulated molecules (PBE-D3/Def2TZVP level of theory) and the values found in literature. The comparison shows a good agreement with literature.

Table S16: Si 2p atoms number, BE, ΔBE (the reference is the S environment) values determined from DFT calculations.

	Si Atom (number)	Environment	BE (ΔKS) (eV)	Standard deviation	$\Delta BE_{\Delta KS}$ (eV)
S = SiC₄	NPP Si38	SiC ₄	107.74		0.00
	NPP Si19	SiC ₄	108.14		0.40
			107.94	0.20	0.20
SiH₂C₂	PDMS plasma Si68	SiH ₂ C ₂	107.97		0.00
M = SiOC₃	NPP Si28	SiOC ₃	108.49		0.75
	TPDMS Si7	SiOC ₃	108.49		0.76
	PDMS plasma Si51	SiOC ₃ m	108.61		0.87
	NPP Si53	SiOC ₃	108.65		0.91
	NPP Si48	SiOC ₃	108.67		0.94
	NPP Si3	SiOC ₃ m2	108.69		0.95
	TPDMS Si1	SiOC ₃	108.78		1.04
	MPDMS Si1	SiOC ₃	108.79		1.06
	NPP Si15	SiOC ₃ m	108.84		1.10
	PDMS plasma Si2	SiOC ₃	108.86		1.13
	NPP Si29	SiOC ₃	108.86		1.13
	MPDMS Si7	SiOC ₃	108.90		1.16
	PDMS plasma Si12	SiOC ₃	108.92		1.19
			108.74	0.12	1.00
D = SiO₂C₂	MPDMS Si2	SiO ₂ C ₂	108.70		0.96
	MPDMS Si5	SiO ₂ C ₂	109.00		1.27
	MPDMS Si3	SiO ₂ C ₂	109.10		1.37
	MPDMS Si4	SiO ₂ C ₂	109.11		1.37
	TPDMS Si3	SiO ₂ C ₂	109.15		1.41
	TPDMS Si2	SiO ₂ C ₂	109.17		1.43
	NPP Si10	SiO ₂ C ₂ m2	109.21		1.48
	TPDMS Si4	SiO ₂ C ₂	109.21		1.48
	PDMS plasma Si41	SiO ₂ C ₂	109.25		1.51
	MPDMS Si6	SiO ₂ C ₂	109.25		1.51
	PDMS plasma Si1	SiO ₂ C ₂	109.27		1.53
	TPDMS Si6	SiO ₂ C ₂	109.27		1.53
	TPDMS Si5	SiO ₂ C ₂	109.39		1.65

	NPP Si24	SiO ₂ C ₂ m	109.54 109.19	0.13	1.80 1.45
SiO₂H₂	PDMS plasma Si63	SiO ₂ H ₂	109.57		0.00
T = SiO₃C	NPP Si45	SiO ₃ C	109.45		1.71
	PDMS plasma Si11	SiO ₃ C	109.84		2.10
	NPP Si11	SiO ₃ C	109.97		2.23
			109.75	0.20	2.01
Q = SiO₄	NPP Si23	SiO ₄	110.29		2.55
	NPP Si1	SiO ₄	110.37		2.63
			110.33	0.04	2.59

Table S16 shows the number of each Si atom and which molecule it belongs to, their calculated binding energy BE (Δ KS) and the binding energy differences Δ BE $_{\Delta$ KS. The S environment was considered as reference for all the BEs due to its lowest binding energy. The m and m2 indices on some SiOC₃ and SiO₂C₂ environments serve to differentiate them. The m index represents a Si-CH₂- bond while the m2 index represents a Si-CH₂-CH₂- bond.

A fine investigation on the chemical composition of a wide range of plasma organosilicon thin films elaborated during this work has been presented in chapter 3. We have characterized the bulk of the PP-HMDSO using powerful techniques such as the ^{29}Si quantitative solid-state NMR completed with FTIR characterization. In addition, the films surface chemical composition was depicted using a powerful methodology based on experimental XPS combined with DFT calculations in order to support the experimental data. As well, WCA angle measurements for the PP-HMDSO in order to determine the surface hydrophobicity. The chemical composition comparison showed a difference between the bulk and the films surface. Furthermore, the results show that the plasma energetic character plays a major role in defining the PP-HMDSO chemical composition. Under a soft plasma, the deposits show a high PDMS-like rate, while the films elaborated under hard plasma conditions present a disorder in the bonds formation. This chemical composition investigation leads to the understanding of the VOCs vapours into organosilicons membranes that will be presented in the next article.

In the next chapter, we will present some of the PP-HMDO physical properties such as refractive index and density. In addition, and most importantly we will present the PP-HMDSO thin films performances towards the VOCs vapours function of the Yasuda parameter (plasma energetic character) using QCM and ellipsometry coupled to sorption. The introduction of this article contains a complementary state of the art concerning the materials used for the VOCs detection. This work will aim to figure out which PP-HMDSO film presents the best sorption performances towards the VOCs vapours especially BTEX for potential application in a portable gravimetric BTEX sensor.

Chapter 4 (2nd article)

This article has been submitted to *Sensors and Actuators B: Chemical*

Plasma polymerized organosilicon thin films for Volatile Organic Compounds (VOCs) detection

Ghadi Dakroub^{1,2}, Thomas Duguet¹, Corinne Lacaze-Dufaure¹, Stéphanie Roualdes², Arie Van der Lee², Diane Rebiscoul³, Vincent Rouessac^{2}.*

¹ CIRIMAT, Université de Toulouse, CNRS, INP- ENSIACET 4 allée Emile Monso - BP44362, 31030 Toulouse cedex 4 - France.

² Institut Européen de Membranes, IEM UMR 5635, Univ Montpellier, ENSCM, CNRS, Montpellier, France

³ ICSM-UMR 5257 CEA-CNRS-UM- ENSCM, CEA, Bagnols-sur-Cèze, France

ABSTRACT: Plasma polymerized (PP) thin films deposited in a soft or intermediate plasma discharge from hexamethyldisiloxane (HMDSO) were developed as sensors for the detection of volatile organic compounds (VOCs) vapours. Energy dispersive X-ray spectroscopy (EDX) and X-ray reflectometry (XRR) were performed to determine the organosilicon films elemental composition and density. Spectroscopic ellipsometry measurements were carried out to determine the refractive index of the films. Quartz crystal microbalance (QCM) and ellipsometry coupled to vapour sorption were used to investigate the sorption mechanism of several VOCs vapours into the films as a function of the plasma deposition conditions. The density and the refractive index of the PP-HMDSO films increased with the plasma energy due to a different chemical composition and different proportion of free volumes in the material network. The PP-HMDSO films showed different affinities towards the VOCs vapours depending on the plasma discharge energy. The films elaborated in the lowest plasma energy revealed a good sensitivity towards the VOCs especially toluene (one of the BTEX vapours) compared to the other films deposited under higher plasma energy. In addition, the selectivity between toluene and other non-BTEX VOCs such as heptane and ethanol decreased to become zero while increasing the plasma energy.

KEYWORDS: Organosilicon, VOCs, sorption, thin films, QCM, Ellipsometry.

Introduction:

Volatile Organic Compounds (VOCs) are toxic gases present in ambient air because of natural resources and human activities, such as the transportation sector or industrial processes. Several materials have been synthesized for VOCs detection such as activated carbons [182], zeolites [183] and metal oxide materials [59]. Activated carbons are useful materials for VOCs detection due to their microporous structure, large surface area and fast adsorption capability [182,184]. However, these materials reveal experimental problems such as their high flammability [185] and difficulty of regeneration [186] that restrain their use in such applications. Alternatively, zeolite materials seems to be useful candidates for VOCs detection thanks to their high specific area, non-toxic behaviour and high thermal stability [187,188]. Nevertheless, zeolite are hydrophilic and thus need a surface treatment to turn hydrophobic [189]. Furthermore, the detection of VOCs using zeolite materials requires a compact Gas Chromatograph (GC) system to analyse the gaseous effluent desorbed from the zeolite by thermal heating [4]. Numerous other studies focused on the sorption of toluene and benzene on metal oxide materials such as ZnO and WO₃ [53,190]. A good sensitivity has been obtained towards benzene and toluene detection with a fast response. Nevertheless, these materials have shown poor selectivity against other VOCs such as acetone and ethanol, except for high operating temperatures [10,191]. On the other hand, metal oxide materials show an important sensitivity to water vapour that highly reduce their sensitivity towards VOCs [192].

Finally, organic polymers represent a very competitive class of materials for VOCs detection, for instance polyisobutylene (PIB) and polybutadiene (PBD), or organosilicon (SiOCH) polymers like polydimethylsiloxane (PDMS) and poly(methylphenylsiloxane) [193–195]. Organosilicon polymers present a high affinity to VOCs and especially to benzene, toluene, ethylbenzene and xylene denoted as BTEX. These polymers are widely used in chromatographic columns for VOCs detection. They have received a remarkable attention for VOCs sensing applications due to their swelling effect upon VOCs absorption [196,197]. In addition, they are non-toxic [99], thermally and chemically stable [73] with high surface hydrophobicity, which is important for the detection of non-polar molecules such as BTEX [135]. More particularly, organosilicon materials prepared by Plasma-Enhanced Chemical Vapour Deposition (PECVD) are currently used in NEMS (Nano Electro Mechanical Devices) devices for organic vapour detection not only because of their high affinity towards the target molecules, but also because they equilibrate more rapidly and reversibly with the sorbed species

than bulk polymers due to their micrometric thickness [198]. Sabahy et al. [5] have studied PECVD-deposited SiOCH thin films for BTEX sensing application. By varying the precursors and plasma deposition conditions i.e. plasma power, monomer flux and O₂ flow rate, different SiOCH chemical compositions have been synthesized and the effects of the chemical bonds on toluene sorption (as BTEX representative) has been investigated. The authors have shown that SiOSi bonds play the major role in toluene adsorption due to the free volumes created by these bonds in the films, either issued from the SiOSi chains flexibility or directly related to the high methyl bonds proportion. In addition, they have concluded that Si-OH bonds are detrimental to toluene sorption. This result can be related to water vapour adsorption on the films surface after deposition favoured by the polarity of the Si-OH bonds preventing toluene adsorption. The impact of Si-(CH₃) bonds has also been studied. High concentration of Si-(CH₃) bonds is detrimental to toluene adsorption, however a compromise between low Si-(CH₃) concentration and films hydrophobicity is necessary. An optimized composition of the plasma-SiOCH thin film could be obtained with a higher affinity towards BTEX than conventional polymers. Finally, Boutamine et al. [6] have elaborated plasma polymerized thin films from HMDSO and investigated VOCs sorption using a quartz crystal microbalance (QCM). The affinity toward VOCs such as ethanol, methanol and chloroform has been correlated to the material surface hydrophobicity, the molecules size and to the free volumes within the films network.

In the present work, we aim at elaborating performant materials for VOCs detection that can be used in the manufacturing of portable gravimetric sensors being competitive in term of compactness when compared to gas chromatograph system (GC). As previously mentioned, due to their well-known low thickness, hydrophobicity, non-toxicity, thermal stability, and high affinity to VOCs, plasma polymerized organosilicon thin films appear as perfect candidates for the targeted application.

In a recent paper [199] we have thoroughly investigated morphological and structural characterizations of plasma polymerized (PP-) organosilicon materials prepared in a microwave plasma discharge from HMDSO. The characterization of the bulk chemical composition studied by FTIR spectroscopy and quantitative ²⁹Si solid state NMR has revealed a high amount of SiOC₃ termination in the films deposited under soft plasma conditions (low plasma energy) due to the low monomer fragmentation. Moreover, linear SiO₂C₂ chains that are close to PDMS chains were present in the material bulk deposited under soft plasma conditions. However, under hard plasma conditions (high plasma energy), the high monomer fragmentation has reduced the amount of SiOC₃ terminations and favoured the introduction of carbon/hydrogen

atoms into the material bulk leading to the formation of new chemical bonds such as Si-O-C, Si-CH₂-Si and Si-H. Furthermore, the amount of the linear SiO₂C₂ chains has decreased in the material bulk at hard plasma conditions. These major evolutions have introduced chemical and structural disorder in the bulk of the elaborated films. The surface chemical composition detected using a combination between X-ray photoelectron spectroscopy (XPS) and density functional theory (DFT) calculations has shown also a chemical modification while increasing the plasma energy. In fact, the number of SiOC₃ unit have increased and the amount of the SiO₂C₂ units have decreased. In addition, the formation of new chemical bonds on the surface such as Si-CH₂-Si, Si-H, Si-O-C and Si-OH, has been confirmed leading to some disorder in the chains formation. Furthermore, the hydrophobicity of the films has been investigated; the PP-HMDSO films have shown a hydrophobic character especially at low plasma energy (close to 103°). As a conclusion of this previous paper, the films deposited under soft plasma conditions have shown a quite similarity to conventional PDMS. On the contrary, the films elaborated under hard plasma conditions have lost their PDMS-like character and changed to more hybrid structures due to the new bond formation and enhancement of the structural disorder in the films.

In the present study, some selected films among the previously prepared SiOCH plasma polymerized thin films are more deeply characterized by Energy dispersive X-ray spectroscopy (EDX) for the elemental composition, X-ray reflectometry (XRR) for the density, and ellipsometry for the film thickness and refractive index. We have decided to select films synthesized in a finer W/F range (5 W/sccm to 20 W/sccm) for which the influence of the chemical composition modification on sorption properties is more pronounced. The deposition conditions of the three samples WF5, WF10 and WF20 are reproduced from [199] and presented in Table 17. The thicknesses of the samples are different from those presented in the previous work due to a different deposition duration. In order to study the affinity of the synthesized films towards VOCs, quartz crystal microbalance (QCM) and ellipsometry, both coupled with gas sorption techniques, are used. Finally, the impact of the chemical composition on the affinity towards VOCs is analysed leading to the identification of an optimized SiOCH film for VOCs gravimetric sensing applications.

Table 17: MW-PECVD thin films deposition parameters issued from [199].

Sample	Plasma power (W)	HMDSO flux (sccm)	W/F	Deposition pressure ($\times 10^{-3}$ mBar)	Average thickness (nm)	Average growth rate (nm/min)
WF5	20	4	5	10.5	332	109
WF10	20	2	10	7.5	344	63
WF20	20	1	20	5.9	296	30

Materials and methods

Characterization methods:

EDX (Silicon Drift Detector (SDD), X-MaxN, Oxford Instrument) analyses were performed in order to obtain the elemental composition of the PP-HMDSO films.

X-ray reflectometry analysis (XRR) were carried out using a Bruker D8 diffractometer with Cu $K\alpha 1$ ($\lambda = 0.154056$ nm) radiation. Standard θ – 2θ scans for the data collections were taken from $2\theta = 0$ to 4° with an angular resolution of 0.002° . XRR measurements allowed the determination of the electronic density (ρ_e) from the limit angle of total reflection (critical angle) Θ_c , using equation (34):

$$\Theta_c = \sqrt{\frac{\lambda^2 r_0}{\pi} \rho_e} \quad (34)$$

Where λ is the wavenumber and r_0 is the electron radius.

The elemental composition determined by EDX and the electronic density calculated by XRR analyses lead to the mass density (ρ_m) of the PP-HMDSO films using equation (35):

$$\rho_m = \rho_e \frac{\sum C_j A_j}{N_A \sum C_j Z_j} \quad (35)$$

Where C_j is the percentage of an element j in the PP-HMDSO chemical composition, Z_j its atomic number, A_j its atomic mass and N_A represents the Avogadro number. The error on the density value is estimated to be ± 0.03 g/cm³. This error is due to the zero-point error (sample height and/or goniometer) and the unknown hydrogen content which is needed to convert the electron density to the mass density.

Thin films refractive indexes and thicknesses were determined by spectroscopic ellipsometry (Semilab GES5E) at atmospheric pressure. The angle of incidence was fixed at 70° and the

collected data range was from 1.2 to 4.5 eV. In the article, the refractive index was given at 633 nm but the data were fitted in the full light range using a composition of Cauchy transparent dispersion law and a Lorentz absorption term towards the UV range. The fit quality exceeds 0.99 in the full range for all depositions.

In situ ellipsometry coupled to sorption (EP) measurements [148] were carried out by exposing PP-HMDSO thin films to toluene or ethanol at controlled vapour pressures. Samples were placed in a homemade optical cell equipped with pressure and temperature control systems. The cell was initially pumped under primary vacuum before any adsorbate introduction down to 0.05 mbar. Afterwards, toluene or ethanol gas vapours were introduced into the pumped cell gradually up to its saturation pressure.

QCM measurements for gas sorption and desorption were performed using an Inficon STM2 thin film oscillator monitor driven by a lab-made data collection software in order to get mass uptake sorption isotherms. PP-HMDSO thin films were deposited on an AT-cut gold-covered quartz (6 MHz). The coated quartz was placed in a chamber under vacuum in which gas vapours were introduced systematically up to its saturated vapour pressure value at room temperature. During measurements, the quartz was thermally stabilized using a water circulation at 25°C. The frequency variation (Δf) between the coated quartz frequency at time t and t_0 was measured in MHz. Δf is proportionally linked to the mass variation (Δm) due to gas vapour sorption or desorption according to Sauerbrey's equation [151] (36):

$$\Delta m = - \frac{\sqrt{\rho_q \mu_q}}{2f_0^2} S \Delta f \quad (36)$$

Where ρ_q and μ_q are the density ($\rho_q = 2.65 \text{ g.cm}^{-3}$) and the shear modulus ($\mu_q = 2.947 \times 10^{11} \text{ g.cm}^{-1}.\text{s}^{-2}$) of the quartz respectively, S is the surface area of the deposited film (0.5 cm^2) while f_0 represents the resonant frequency (6 MHz). The mass density of the deposited film can be neglected compared to the mass density of the quartz. Thus, we have considered that the density of the coated quartz is equal to the density of the pristine quartz (ρ_q). Since the mass of both the quartz and the films are constant, Δm corresponds to the sorbed vapour mass uptake m_{sorbed} by the thin films. Therefore, the mass uptake (m_{sorbed}) of the deposited thin films was determined using equation

(37):

$$m_{sorbed}(P/P_0) = \frac{-\Delta f}{f_q^2} 1.67 \times 10^5 \times \rho_q \times S \quad (37)$$

The collected data were converted into mass uptake using equation (37) and isotherms of m_{sorbed} as a function of relative pressure (P/P_0) were collected and plotted.

Results

In this section, the elemental composition and physical properties such as density and refractive index of the PP-HMDSO thin films as well as their response towards several VOCs vapours separately are presented.

The elemental composition determined by EDX reveals a quite similar composition of the three films. The carbon, oxygen and silicon percentages are 52.2%, 22.4% and 25.4% respectively, revealing a composition close to conventional PDMS (table S18 in SI annex 2).

The calculated density and the refractive index of the PP-HMDSO thin films are presented in Figure 33. The film deposited at 5 W/sccm reveals a low density (1.35 g/cm^3) compared to the films deposited at 10 W/sccm and 20 W/sccm (values close to 1.45 g/cm^3). In addition, the refractive index of the SiOCH films increases from 1.52 for the films deposited at 5 W/sccm to values close to 1.57 for the films deposited at 10 W/sccm and 20 W/sccm. In fact, the variation of the films density generates a variation of the deposited films refractive index while increasing the W/F parameter. Indeed, the well-known Clausius-Mosotti equation

(38) reveals the influence of the material density to the dielectric constant or the refractive index (n), since $\epsilon = n^2$ in the visible optical range:

$$\frac{\epsilon - 1}{\epsilon + 2} = \frac{\rho_m}{3\epsilon_0} \sum_{i=1}^k N_i \alpha_i \quad (38)$$

Where ρ_m is the density of the elaborated SiOCH films, ϵ_0 is the vacuum permittivity, ϵ is the dielectric constant, N_i is the number of atoms i per cm^3 , and α_i is the polarizability of atom i .

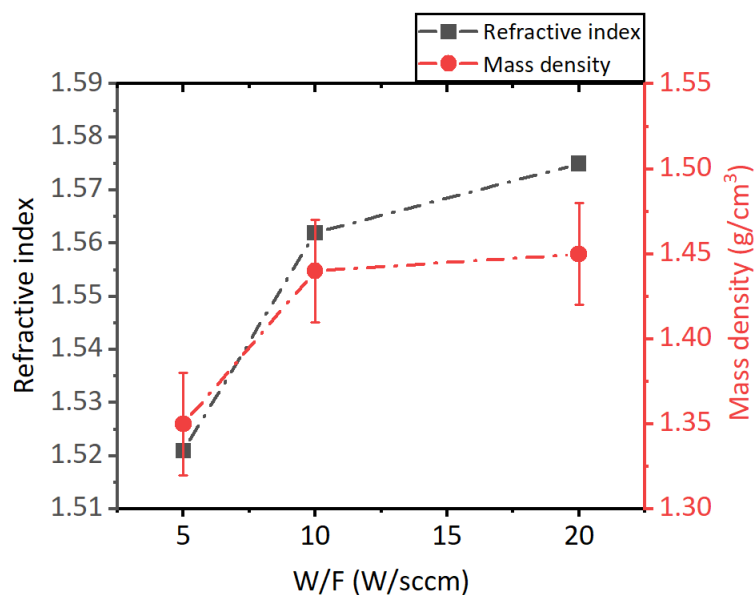


Figure 33: The refractive index and the calculated density of the deposited films

The responses of the PP-HMDSO thin films towards hydrocarbons and ethanol vapours sorption studied using QCM are presented in Figure 34. In this study, heptane and ethanol vapours were used as representatives for COVs and toluene vapour as representative for BTEX gases. Ethanol vapour was used as reference in order to compare its sorption to hydrocarbons. The calculated mass uptake value represents the mass of the vapour sorbed by the thin film. The effect of the films thickness on the toluene vapour sorption was studied (Figure S37 in SI annex 2). As a result, the mass uptake increases proportionally with the film thickness. Thus, it can be concluded that the molecules are not only adsorbed on the film surface but are absorbed in the bulk also. Therefore, the mass uptake was simply divided by the film thickness value to get the concentration of absorbed molecules per material volume unity even if no conclusion can be written on how the absorbed molecules are diluted in the material matrix, homogeneously or in a gradient concentration from the surface to the bulk. The uncertainty on the mass uptake value is taken as the standard deviation over three repeated QCM measurements.

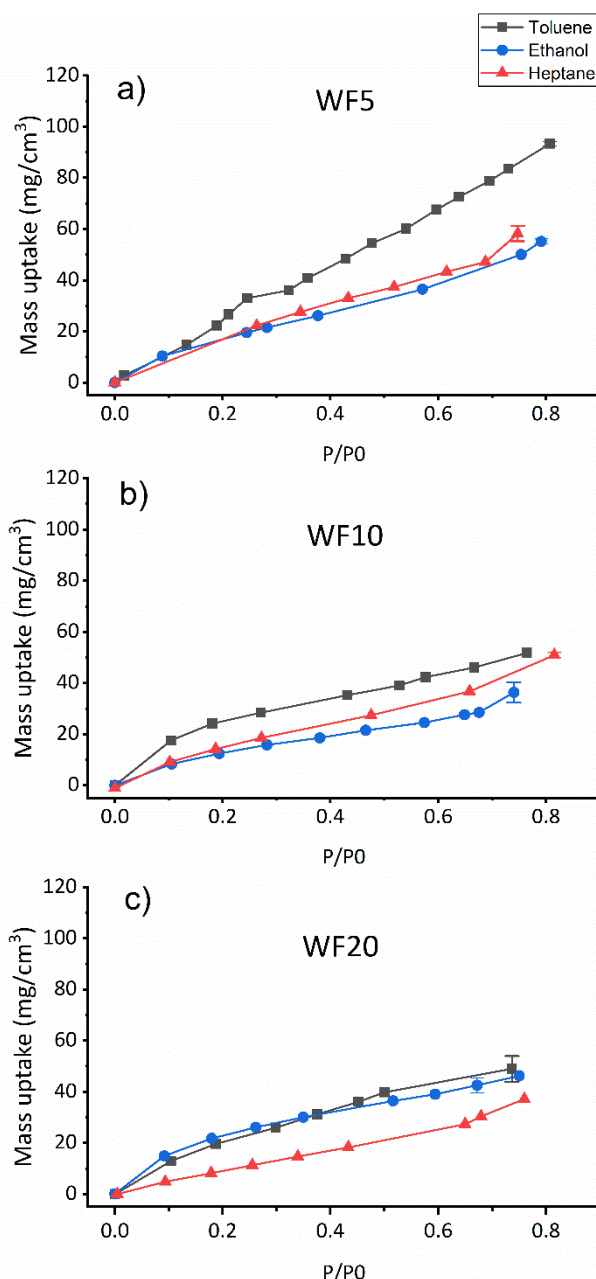


Figure 34: QCM sorption isotherms (25°C) showing the evolution of ethanol, heptane and toluene vapour mass uptake with P/P_0 for a) WF5, b) WF10 and c) WF20.

As observed in Figure 34, the mass uptake of the gas vapours increases with increasing the relative pressure P/P_0 for all the PP-HMDSO thin films, P_0 being the saturated vapour pressure at the temperature of the quartz, stabilized at 25°C. The WF5 film shows a linear increase of the toluene uptake mass up to 100 mg/cm³ at a relative pressure equal to 0.8. Moreover, heptane and ethanol uptake masses reveal also a linear increase but to lower values (close to 60 mg/cm³) compared to toluene. Thus, the WF5 deposit shows a better affinity to toluene vapour than the two other vapours. The WF10 deposit shown in Figure 34b illustrates weaker responses to the three vapours compared to the WF5 deposit especially to toluene vapour. Besides, the toluene isotherm of the WF10 film shows a non-linear increase. However, the final mass uptake for

toluene vapour is higher than the two other vapours masses especially than ethanol uptake mass indicating a better affinity for WF10 towards toluene vapour. Besides, WF5 and WF10 deposits reveal a slightly better affinity towards heptane vapour compared to ethanol vapour. On the other hand, the deposit with the higher W/F (WF20) shows similar isotherms for toluene and ethanol. The toluene and ethanol isotherms shows a non-linear uptake mass increase showing a fast sorption between 0 and 0.2 P/P_0 followed by a slower sorption between 0.2 and 0.8 P/P_0 . Furthermore, heptane vapour isotherm reveal uptake masses lower than toluene and ethanol suggesting a weaker affinity towards heptane vapour compared to toluene and ethanol vapours.

Figure 35 focuses on the comparison between the toluene sorption isotherms of the three PP-HMDSO thin films. A remarkable change in the sorption isotherms is shown while increasing W/F from 5 W/sccm to 10 W/sccm. However, identical isotherms are observed for the films elaborated at 10 W/sccm and 20 W/sccm.

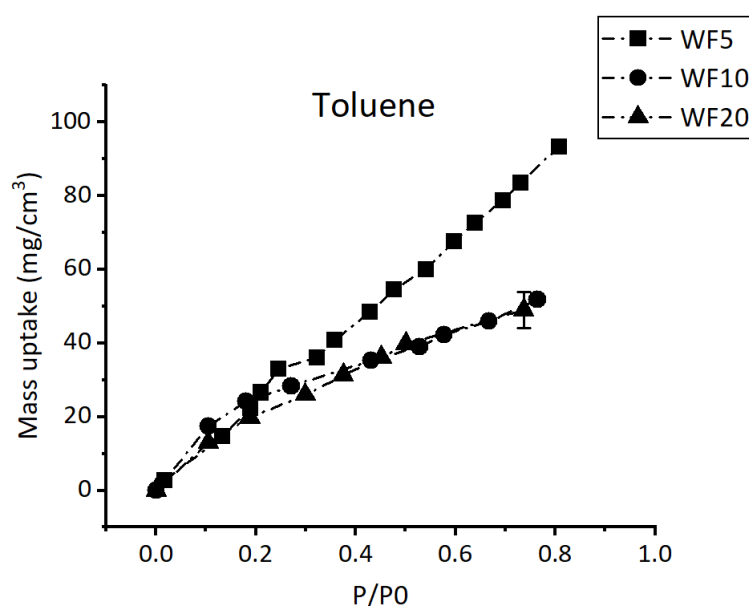


Figure 35: QCM toluene sorption isotherm (25°C) of films synthesized at different W/F values.

In fact, the toluene isotherm loses its linearity while increasing W/F from 5 W/sccm to 10 W/sccm and the final uptake mass value decreases from 100 mg/cm^3 to 50 mg/cm^3 approximately. These variations indicates a slower sorption process especially at lower P/P_0 values (between 0 and 0.2) and a weaker affinity for WF10 and WF20 deposits towards toluene compared to WF5.

The responses of the PP-HMDSO thin films towards toluene and ethanol vapours was also studied using ellipsometry coupled to vapour sorption. Figure 36 shows the swelling of the PP-HMDSO thin films along the normal to the film when exposed to toluene or ethanol vapours.

We assume in this study that the swelling is homogenous despite the mechanical constraints present between the film and the silicon support. This model induces that the COVs concentration should vary along the depth of the film from the surface. d_0 is the thickness measured under vacuum and d is the thickness measured as a function of the stabilized environment pressure, i.e. after enough time to attend the equilibrium between the gaseous molecules pressure and the absorbed molecules pressure inside the material bulk.

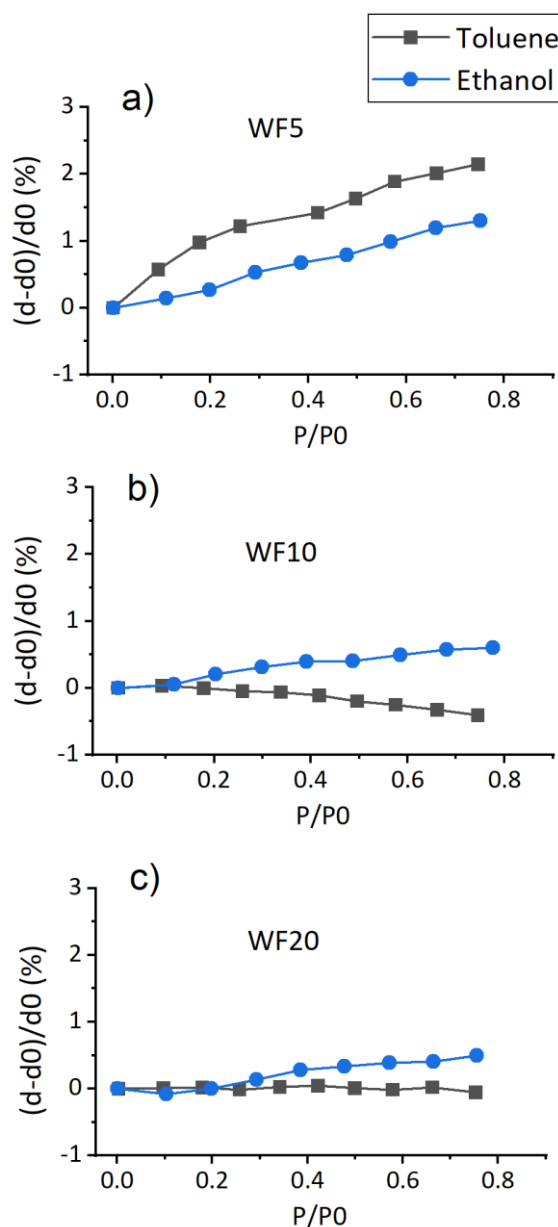


Figure 36: Swelling of the elaborated PP-HMDSO thin films while exposed to toluene or ethanol atmospheres.

The swelling phenomenon of the SiOCH films when exposed to VOCs is due to the penetration of the gas vapours into the material bulk through the free volumes present in the polymer network. Figure 36 reveals that the thickness of WF5 thin film increases while increasing

toluene or ethanol vapour relative pressure. However, WF5 reveals a higher swelling rate for toluene compared to ethanol. Therefore, WF5 shows a better absorption of toluene molecules compared to ethanol molecules. On the other hand, WF10 and WF20 isotherms indicate a low film-swelling rate while exposed to both vapours. Nevertheless, WF10 swelling rate is slightly better when exposed to ethanol compared to the swelling rate in the presence of toluene for which a slight film contraction is observed.

Discussions

Density and refractive index

The density change shown in Figure 33 while increasing W/F from 5 W/sccm to 10 W/sccm and 20 W/sccm is probably the result of the introduction of carbon atoms into the film skeleton to replace the oxygen atom in the Si-O-Si chains creating new bonds such as Si-O-C and Si-CH₂-Si. In fact, the Si-O-Si chains that form the material skeleton of organosilicon films are responsible of creating free volumes in the material network and decreasing the density [200]. However, the replacement of these bonds by Si-O-C and Si-CH₂-Si bonds and the disorder introduced in the films network at higher W/F values shown in our previous work [199] reduce the proportion of free volumes in the material bulk causing the increase of the films density. Furthermore, the refractive index enhancement with W/F can be demonstrated by the films density increase (equation (38). due to the reduction of the free volume proportion. In addition, the refractive index increase can be a result of another factor, which is the electronic polarizability increase due to the incorporation of carbon atoms into the material bulk. In fact, the incorporation of carbon atoms can generate variations on chemical bond angles in the SiOCH films leading to reduce the number of dipole moments in the system, hence, increasing the polarizability [117,118,201]. Accordingly, the remarkable differences in the densities and refractive indexes between WF5 on the one hand and WF10/WF20 on the other hand confirms the division of the soft plasma range into two groups. In fact, the weak variation in the energetic plasma character between WF5 and WF10 enhances the PP-HMDSO films density and refractive index by changing the film composition and reducing the proportion of free volumes in the SiOCH film.

Gas sorption performance

The SiOCH films performance towards VOCs vapours sorption depends strongly on the chemical composition and the structure of the films. In the WF5 material, the sorption

selectivity between toluene and ethanol is due to the hydrophobicity difference of the films surface shown previously [199] that gives a higher affinity towards the non-polar toluene. In addition, the better response for toluene compared to heptane can be assigned to the molecule size and chain length for linear hydrocarbons. We assume that the absorption of toluene into the films is greater than the absorption of heptane, which mainly remains adsorbed on the surface. In fact, Zheng Yang et al. concluded that alkanes lie flat on silica surface and the molecules adsorption on the surface increases with chain length [202]. We have also studied butane vapour sorption on WF5 sample (Figure S38 in SI annex 2). Butane vapour showed good affinity towards WF5. The butane sorbed mass was 36 mg/cm^3 at $P/P_0 = 0.34$ greater than heptane sorbed mass (27 mg/cm^3) at the same P/P_0 value. Thus, WF5 thin film revealed a better affinity towards butane vapour than heptane because of its shorter chain length. This result is consistent with the work of Zheng Yang et al [202].

The decrease in the toluene uptake mass and the loss of linearity of the isotherm, i.e. slower sorption process, while increasing W/F to 10 W/sccm and 20 W/sccm suggest a toluene sensitivity decrease for the materials elaborated at higher plasma energy. In fact, the reduction of the free volumes proportion detected in the density section weakens the toluene sorption process. In addition, the formation of Si-OH bonds on the surface at higher W/F favours a rapid water adsorption on the surface and can be detrimental for toluene sorption [5]. These chemical and physical modifications can explain also the loss of the selectivity between toluene and ethanol vapours shown especially in the WF20 deposit. Furthermore, the weak hydrophobicity of WF20 compared to the two other samples and the large size of heptane molecule result in lower sorbed masses compared to ethanol and toluene. As mentioned before, alkanes lie flat on the silica surface [202]; this conclusion can explain the low penetrated masses of heptane compared to toluene in all the PP-HMDSO thin films.

Similarly, the ellipsometry coupled to sorption results reveal a loss of the swelling rate during toluene sorption for WF10 and WF20 indicating a weak affinity towards toluene vapour. In fact, the material density increase and the chemical composition modifications observed in WF10 and WF20 prevents the film swelling leading to a decrease in the gas vapours penetration into the material. In addition, the swelling phenomenon can be linked to the crosslinking degree of the films and the bonds chemical composition. In fact, a low crosslinking rate induces the swelling of the polymeric chains [197]. Furthermore, the flexibility of the Si-O-Si chains facilitates the penetration ability of VOCs, unlike Si-O-C chains that are less flexible. Hence, the low films swelling rate can suggest an improvement in the WF10 and WF20 hardness

provoked by the structural and chemical deformation of the films network shown in Dakroub et al.[197,199,201]. On the other hand, we assume that the decrease in the WF10 film thickness while exposed to toluene vapour is due to the absence of the free volume that prevents toluene vapour absorption and a less rigidity of the WF10 film compared to WF20. Finally, the ellipsometry coupled to sorption results are in accordance with QCM results showing a better affinity for WF5 towards toluene vapour compared to ethanol vapour.

Conclusion

In a previous work, we determined the effect of the plasma energy on the chemical composition and structure of the PP-HMDSO thin films. In the present article, physical properties such as refractive index and density of the films were presented. In addition, the effects of the materials chemical composition and the physical properties on the sorption of VOCs vapours were also investigated.

In conclusion, the plasma energy governs the density of the films. In fact, the films free volumes proportion decreases while increasing the plasma energy leading to a denser material due to the formation new bonds such as Si-CH₂-Si and Si-O-C in the film structure. The chemical composition modification shown previously and the density variation with the plasma energy affect both the sensitivity and the sorption selectivity of the materials towards the VOCs. In fact, the PP-HMDSO thin films elaborated in this study, showed different responses towards tested VOCs vapours (ethanol, heptane, toluene) despite the small plasma conditions variation between WF5, WF10 and W20 (5 W/sccm to 20 W/sccm). The WF5 showed good sensitivity towards toluene and good sorption selectivity between toluene and the other tested VOCs compared to the WF10 and WF20 deposits. This is due to a low density and high hydrophobicity ($\approx 103^\circ$ detected previously in [199]) of the WF5 material as well as a high SiOSi bonds amount in the PP-HMDSO network.

Finally, chemical and physical properties play important roles in the vapours sorption into the organosilicon films. A combination of surface hydrophobicity and free volumes size (density) should be optimized in order to achieve a good sensitivity/selectivity to toluene (BTEX) vapour compared to other VOCs.

Appendix A. Supporting Information

Elemental composition of the thin films.

Film thickness effect on sorbed masses.

Butane vapor sorption into PP-HMDSO thin films.

Corresponding Author

*Corresponding Author Email: vincent.rouessac@umontpellier.fr, Tel. +33. (0) 4 67 14 91 45

Acknowledgements

We warmly thank the French Carnot Institute *Chimie Balard Cirimat* (PhD grant #ENSCM2018.2021-IEM/PETAB/2018-030) for supporting this work and Bertrand Rebière from IEM for the EDX analyses.

Annex 2: Supplementary Information of article 2 (chapter 4)

Plasma polymerized organosilicon thin films for Volatile Organic Compounds (VOCs) detection

Ghadi Dakroub^{1,2}, Thomas Duguet¹, Corinne Lacaze-Dufaure¹, Stéphanie Roualdes², Arie Van der Lee², Diane Rebiscoul³, Vincent Rouessac^{2}.*

¹ CIRIMAT, Université de Toulouse, CNRS, INP- ENSIACET 4 allée Emile Monso - BP44362, 31030 Toulouse cedex 4 - France.

² Institut Européen de Membranes, IEM UMR 5635, Univ Montpellier, ENSCM, CNRS, Montpellier, France

³ ICSM-UMR 5257 CEA-CNRS-UM- ENSCM, CEA, Bagnols-sur-Cèze, France

Elemental composition:

Table S18 illustrates the elemental compositions of the PP-HMDSO thin films determined by EDX. WF5, WF10 and WF20 reveal a very close elemental composition. Indeed, these deposits were elaborated in soft/intermediate plasma energy [199]. Accordingly, the mean value of the elements percentages was calculated and presented in Table S18. The mean elemental composition shows a composition close to conventional PDMS on the contrary of the film elaborated in high plasma energy (reported from [1]) which illustrates a replacement of some oxygen atoms by carbon atoms in the material bulk. These EDX results are consistent with the chemical characterization results obtained previously [199].

Table S18: Elemental composition of the PP-HMDSO deposits

	Conventional PDMS	WF5	WF10	WF20	Mean values	WF130 (Hard conditions)
% C	50	52.9	51.0	52.6	52.2 ± 0.8	58.2
% O	25	21.1	23.0	23.0	22.4 ± 0.8	16.4
% Si	25	26.0	26.0	24.4	25.4 ± 0.7	25.4

Gas sorption performance

Film thickness effect on toluene sorption:

Figure S37 shows the responses of three WF5 films elaborated at different thicknesses (120 nm, 220 nm and 345 nm) towards toluene vapor studied by QCM. The obtained uptake mass values of each sample are divided by its film thickness. The three isotherms reveal a quite similar evolution while increasing P/P_0 . Thus, we can assume that the uptake mass increases linearly with film thickness indicating that the toluene vapor is not only adsorbed on the surface but it is also absorbed by the whole film thickness. However, the distribution of the toluene molecules into the film matrix remains unknown, it can be diluted homogeneously or in a gradient concentration from the surface to the bulk.

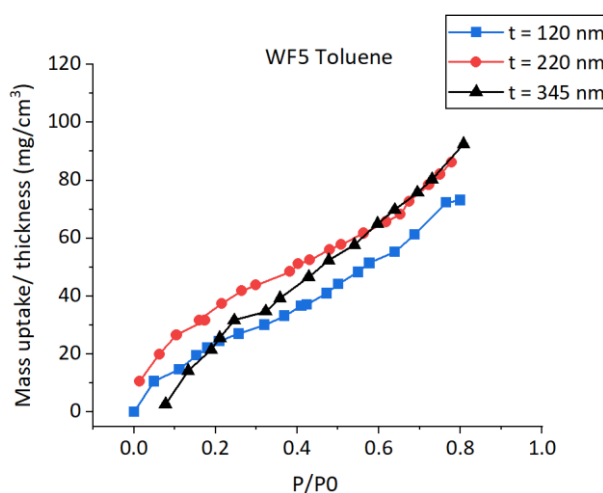


Figure S37: QCM Toluene sorption isotherms (25°C) for the WF5 deposit elaborated at different thicknesses 100 nm, 200 nm and 300 nm.

Butane vapour sorption:

Figure S38 shows the QCM isotherms of heptane and butane vapours sorbed in the WF5 deposit. The butane vapour isotherm reveals a maximum value of P/P_0 equal to 0.34. In fact, the butane absolute pressure was fixed at 1 bar for security reasons because the room in which was installed the gas-tight QCM setup under vacuum was not adapted to over pressures of explosive gases. Despite the short range from vacuum up to $P/P_0 = 0.4$, the butane isotherm shows higher sorbed masses than the heptane isotherm indicating a better sensitivity for WF5 to butane vapour than to heptane vapour. This affinity is due to the size of the butane molecule which is shorter than the heptane one, allowing a better penetration of the butane molecules into the material bulk.

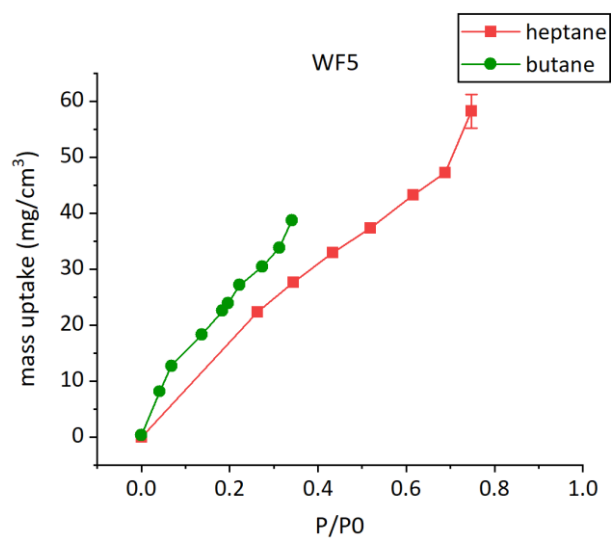


Figure S38: QCM sorption isotherms (25°C) showing the evolution of heptane and butane vapours mass uptake with P/P_0 for WF5

In Chapter 3, we have determined the plasma energetic character (Yasuda parameter) effect on the PP-HMDSO chemical composition and structure. In chapter 4, we have completed the PP-HMDSO chemical structure investigation by some physical properties such as density and refractive index. In addition, the main objective of this work was to reveal the effects of the materials chemical composition and physical properties on the VOCs sorption for gas sensing applications. As a result, the plasma energy affect the density of the films. In fact, at high plasma energy, the elaborated materials are densified due to a reduction in the materials free volumes proportion. Furthermore, the VOCs sensitivity and selectivity are strongly dependent on materials chemical composition and physical properties. The WF5 deposit elaborated in the softest plasma showed the best sorption performances towards the VOCs with a good sensitivity and toluene selectivity compared to other VOCs. Therefore, this work allowed us to outline among a wide range of PP-HMDSO membranes, the one with the best sorption performances.

The objective of the next chapter is to improve the response of the chosen material towards the BTEX vapors in order to achieve a better sensitivity/selectivity compared to other VOCs. The chosen material will be thermally treated under different atmosphere conditions in order to enhance its sorption performance. The sorption results will be studied function of the annealing atmosphere using QCM and ellipsometry coupled to sorption. In addition, this work will aim to understand the vapors sorption mechanism into the whole PP-HMDSO film. In other words, the objective of this work is to optimize the PP-HMDSO membrane for potential application in a portable BTEX gravimetric sensor.

Chapter 5 (3rd article)

Potentiel corrections and complements could be added before being submitted in sensors and actuators B: chemical

Plasma polymerized organosilicon thin films for BTEX sensors applications

Ghadi Dakroub^{1,2}, Thomas Duguet¹, Corinne Lacaze-Dufaure¹, Stéphanie Roualdes², Arie Van der lee², Diane Rebiscoul³, Vincent Rouessac^{2}.*

¹ CIRIMAT, Université de Toulouse, CNRS, INP- ENSIACET 4 allée Emile Monso - BP44362, 31030 Toulouse cedex 4 - France.

² Institut Européen de Membranes, IEM UMR 5635, Univ Montpellier, ENSCM, CNRS, Montpellier, France

³ ICSM-UMR 5257 CEA-CNRS-UM- ENSCM, CEA, Bagnols-sur-Cèze, France

Abstract: Plasma polymerized Hexamethyldisiloxane (PP-HMDSO) thin films deposited at soft plasma energy were developed as sensor for the detection of Benzene, Toluene, Ethylbenzene and p-Xylene (BTEX) vapors. Thermogravimetric analyses (TGA) were performed to study the films thermal stability. Accordingly, thermal treatments under air and nitrogen were carried out in order to increase the free volumes in the PP-HMDSO network. FTIR spectroscopy and Energy dispersive X-ray spectroscopy (EDX) were used to determine the thermal treatment effect on the films chemical composition. Spectroscopic ellipsometry measurements were performed to determine the films refractive index. Quartz crystal microbalance (QCM) and ellipsometry coupled to vapor sorption were used to investigate the sorption mechanism of the BTEX vapors into the films as a function of the thermal treatment atmosphere. The chemical composition characterization showed the formation of Si-OH bonds and loss of the Si-C and Si-H bonds after thermal treatment under air. However, the chemical composition revealed slight modifications after treatment under nitrogen. The films refractive index decreased after annealing due to a different chemical composition and free volumes distribution and size. The PP-HMDSO film showed a better sensitivity to all BTEX vapors after thermal treatment and a better selectivity compared to ethanol especially after a thermal treatment under nitrogen.

KEYWORDS: Organosilicon, BTEX, sorption, thin films, QCM, ellipsometry

Introduction:

Air pollution becomes one of the most severe problems nowadays due to the uncontrolled pollutant emissions derived from human activities, transport and industries sectors [1,2]. Several studies concerning the influence of the pollutant emissions on the environmental and human health has pushed many countries to apply serious laws in order to reduce the pollutant quantities in air or water. Volatile Organic Compounds (VOCs), especially BTEX (Benzene, Toluene, Ethylbenzene and Xylene) are known as dangerous air and water pollutants, because of their carcinogen and mutagenic effects [3]. In addition, they provoke hazardous threats to human health even at low concentrations by causing diseases, harm to the liver and the nervous system [17,19,203].

These severe problems made France in 2016 to set a limit value of 0.6 ppb for benzene in public buildings [4]. Similarly, the Guidelines for Canadian Drinking Water quality specifies that the maximum acceptable concentration in drinking water for benzene, toluene, ethylbenzene and for all xylenes are 0.005 mg/L, 0.06 mg/L, 0.14 mg/L and 0.09 mg/L respectively [204]. Therefore, the necessity of high and on site BTEX sensing devices for air and/or water quality control as well as human health monitoring.

The existent most powerful technique for BTEX detection is the gas chromatography (GC), permitting a very low BTEX detection limits down to ppt levels. However, this technique reveals problems such as high cost, huge size and high-energy consumption that limits its utilization for in-situ detections by samples collecting and off-line analysis. Other techniques such as optical sensors have gained interests recently for gas detection applications due to their high sensibility, sensitivity and stability. In addition, these techniques have showed a real time detection ability due to their relatively short time response. However, the gas detection application of the optical sensors can be seriously restricted due to their high cost and the difficulty of miniaturization. Furthermore, for hydrocarbon gases detection, the use of a broadband source in the mid-IR can reduce the selectivity between hydrocarbons, and thus the selective detection of BTEX. In fact, some hydrocarbons gases have absorption bands in the same spectral region and the use of a mid-IR system will often detect other hydrocarbons [205–207]. Several other technologies have been studied in order to detect and monitor BTEX vapours on a real time basis such as metal oxide semiconductors and gravimetric sensors [55,208]. Metal oxides semiconductor sensors are good devices for VOCs and BTEX detection. The detection principle of these devices is based on the conductivity change during the

interaction with the targeted molecules. These devices type presents many advantages such as high sensitivity, low detection limits, real-time detection and low power consumption [53,190,191,209]. However, despite all the cited advantages, these devices based on metal oxides show poor selectivity between the VOCs. In addition, these devices require high operating temperatures due to the water adsorption on the surface especially in humid atmosphere [10].

Gravimetric or mass sensitive sensors are other promising techniques for gas detection due to their high sensitivity and selectivity. These devices are electromechanical systems and their detection principle is based on measuring the frequency shift caused by a mass increase due to the sorption of the targeted analytes. In this context, the most widely used electromechanical device is the quartz crystal microbalance (QCM). This system is widely used in VOCs detection applications due to its low cost and its capacity of measuring small mass variations on the nanogram scale [210–212].

In a previous work, we have characterized, using a gravimetric sensing technique (QCM), toluene and ethanol sorption on different organosilicons thin films [article 2] that had been previously elaborated by Plasma-Enhanced Chemical Vapor Deposition (PECVD) and morphologically and structurally characterized [199]. The film deposited in the softest plasma conditions had revealed the higher sensitivity to toluene and a good selectivity to toluene compared to ethanol.

In this paper, the previously optimized deposit has been thermally treated under air and nitrogen in order to improve its response towards all BTEX vapours. Fourier transform infrared (FTIR) and Energy-dispersive X-ray spectroscopy (EDX) characterizations are carried out in order to determine the chemical composition before and after annealing. Ellipsometry measurements are performed to determine the refractive index change after annealing. Furthermore, the films responses towards the targeted analytes and the sorption mechanism are investigated using QCM and ellipsometry coupled to sorption. In addition, a comparison between the different BTEX vapours sorption is illustrated. More globally, this work illustrates an optimized and promising organosilicon material for BTEX gravimetric sensing applications.

Materials and methods

Thermal treatment:

Two samples of plasma-polymerized thin film, synthesized in a microwave PECVD discharge at 20 W input power and 4 sccm Hexamethyldisiloxane (HMDSO) flow rate [referenced WF5 in article 1 and 2], were annealed at 300°C under air or nitrogen atmospheres. The temperature heating rate was constant at 5 °C.min⁻¹ from room temperature up to 300°C where a plateau of 15 minutes was maintained before cooling.

Characterization methods:

Thermogravimetric analyses (TGA) of annealed WF5 films were carried out on a TGA-STD Q600 apparatus in order to display the optimal atmosphere and annealing temperature. The samples were purged with nitrogen or air flow rate of 100 ml.min⁻¹. The temperature heating rate was constant at 5 °C.min⁻¹ from room temperature up to 1000 °C. The samples weights were 5 mg for the sample purged with nitrogen flow and 10 mg for the sample purged with air flow.

The FTIR spectra were registered at room temperature in transmission mode between 400 and 4000 cm⁻¹ using a Nicolet NEXUS spectrometer with a scanning velocity of 0.4747 cm/sec. The background signal of the silicon wafer (support) was subtracted from all the spectra.

Energy dispersive X-ray spectroscopy (EDX) analysis were carried out on a Silicon Drift Detector (SDD), (X-MaxN, Oxford Instrument) in order to determine the samples elemental composition. A dispersion on the results was estimated by the analyses of 4 different areas on the film. This dispersion was close to 0.1%.

X-ray reflectometry analysis (XRR) was carried out using a Bruker D8 diffractometer with Cu Kα1 ($\lambda = 0.154056$ nm) radiation. Standard θ – 2θ scans for the data collections were taken from $2\theta = 0$ to 4° with an angular resolution of 0.002° . XRR measurements determine the calculated limit angle of total reflection (critical angle) θ_c leading to the calculation of the electronic density (ρ_e) using (39):

$$\theta_c = \sqrt{\frac{\lambda^2 r_0}{\pi} \rho_e} \quad (39)$$

Where λ is the wavenumber and r_0 is the electron radius.

The mass density (ρ_m) of the samples was deduced from equation (40) using the elemental composition obtained by the EDX measurements and the electronic density (ρ_e) calculated in equation (1).

$$\rho_m = \rho_e \frac{\sum C_j A_j}{N_A \sum C_j Z_j} \quad (40)$$

Where C_j is the number of an element j in the chemical formula (deducted from the elemental composition analysis), A_j its atomic mass, Z_j its atomic number and N_A is the Avogadro number. The estimated error of the density value is $\pm 0.03 \text{ g/cm}^3$. This error is due to the zero-point error (sample height and/or goniometer) and the unknown hydrogen content which is needed to convert the electron density to the mass density.

QCM measurements for gas sorption and desorption were performed on an Maxtek TM-400 apparatus. WF5 thin films were deposited on an AT-cut gold covered quartz (6 MHz). The quartz temperature was fixed at 25°C during the measurements using a water circulation system. The Frequency variation (Δf) of the coated quartz between t and t_0 was measured in MHz. Δf was linked proportionally to the mass variation (Δm) due to gas vapour sorption or desorption according to Sauerbrey equation (41):

$$\Delta m = - \frac{\sqrt{\rho_q \mu_q}}{2f_0^2} S \Delta f \quad (41)$$

Where ρ_q and μ_q are the density ($\rho_q = 2.65 \text{ g.cm}^{-3}$) and the shear modulus ($\mu_q = 2.947 \times 10^{11} \text{ g.cm}^{-1}.\text{s}^{-2}$) of the quartz respectively, S is the surface area of the deposited film (0.5 cm^2) while f_0 represents the resonant frequency (6 MHz). The thin film mass density can be neglected compared to the quartz mass density. Therefore, we have considered that the density of the coated quartz is equal to the density of the pristine quartz (ρ_q). Δm corresponds to the sorbed vapour mass uptake m_{sorbed} by the thin films since the mass of both the quartz and the films are constant. Therefore, the mass uptake (m_{sorbed}) of the deposited thin films was measured using equation (42):

$$m_{\text{sorbed}} (P/P_0) = \frac{-\Delta f}{f_q^2} 1.67 \times 10^5 \times \rho_e \times S \quad (42)$$

The coated quartz was placed in a chamber under vacuum in which gas vapours were introduced systematically up to their saturated vapour pressure value at room temperature. The collected

data were converted into mass uptake using equation (42) and $m_{\text{sorbed}}(P/P_0)$ isotherms were drawn.

Thin films refractive index and thickness were determined by spectroscopic ellipsometry (Semilab GES5E) at atmospheric pressure. The angle of incidence was fixed at 70° and the collected data range was from 1.2 to 4.5 eV. The refractive index was measured at 633 nm. The data were fitted using a composition of Cauchy transparent dispersion law and a Lorentz absorption term towards the UV range. The fit quality exceeds 0.99 in the full range for all the depositions. In situ Ellipsometry coupled to vapours sorption measurements [150] were performed by exposing the WF5 thin films to toluene or ethanol vapour pressure. These measurements allow determining the evolution of the films refractive index and thickness during vapours sorption.

The samples were placed in a homemade optical cell equipped with a pressure and temperature control systems. The cell was initially pumped under primary vacuum before the introduction of any adsorbate. Toluene or ethanol gas vapours were introduced into the pumped cell gradually up to its saturation pressure.

Results and discussion:

Thermal analysis:

The TGA of WF5 deposits under both air and nitrogen flows are shown in Figure 39. Comparison of thermal degradation of the film in the presence of air or nitrogen provide some highlights on effects of each degradation condition.

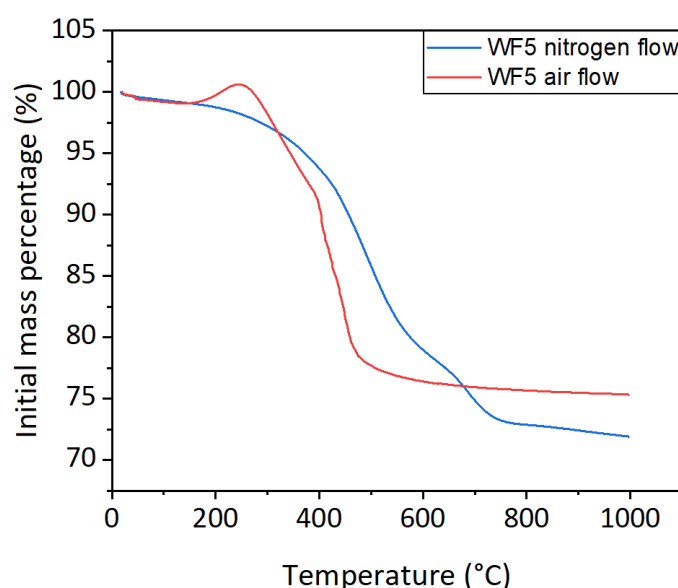


Figure 39: TGA of WF5 films under nitrogen flow (blue line) and under airflow (red line).

The TGA curve under air flow shows a slight mass gain that begins near 221°C which is absent in the TGA curve under nitrogen flow. We assume that this mass gain is due to the replacement of carbon and hydrogen atoms by oxygen atoms consecutive to Si-C and Si-H bonds cleavage (i.e. oxidation of some Si atoms). In fact, the IR spectrum of WF5 annealed at 250°C in the presence of air (Figure S46 in SI annex 3) reveals the rise of a broad absorption band between 3300 cm⁻¹ and 3800 cm⁻¹ that is assimilated to Si-OH bonds as well as a decrease in the intensity of the Si-H and Si-C bonds. The absence of this mass gain in the TGA curve under nitrogen is simply due to the absence of oxygen in the nitrogen atmosphere. The major mass loss appearing at 300-350°C in the both TGA curves can be attributed to the cleavage of the Si-H and Si-C bonds. Since the Si-O-Si bonds form the backbone chains of the films, the residue left at 500°C can be assimilated to silica as shown also in the TGA curve of PDMS [213]. However, the TGA curve under nitrogen flow reveals a shift to higher temperatures for the beginning of this major mass loss compared to the TGA curve under airflow. This is due to the presence of oxygen under airflow that accelerates the degradation of the WF5 film causing a faster weight loss. Based on the TGA analyses, the annealing temperature was chosen in the interval between 250°C and 350°C. After several attempts, the optimal annealing temperature was selected at 300°C for both atmospheres.

Chemical composition:

Figure 40 shows the FTIR spectra of WF5 films before and after thermal annealing. As shown in our previous work, the FTIR spectrum of non-annealed WF5 shows strong absorption bands at 2960 cm⁻¹, 2900 cm⁻¹ (Figure 40c) 2140 cm⁻¹ (Figure 40b), 1257 cm⁻¹, 1010-1090 cm⁻¹, 840 cm⁻¹ and 795 cm⁻¹ (Figure 40a). The absorption bands at 2960 cm⁻¹, 2900 cm⁻¹ and at 2140 cm⁻¹ correspond to CH₃, CH₂ and Si-H stretching vibrations, respectively. The sharp absorption band located at 1257 cm⁻¹ represents the CH₃ symmetric bending in SiMe_x (Me used as abbreviation for the methyl bond CH₃). In addition, the wide absorption band shown in Figure 40a represents the Si-O-Si stretching vibrations and it is composed of two bands present near 1030 cm⁻¹ and 1090 cm⁻¹. This wide absorption band can also envelope the Si-O-C asymmetric stretching present near 945 cm⁻¹. Moreover, the Si-CH₂-Si absorption band is usually observed between 1080-1040 cm⁻¹, but for organosilicon coatings this peak is probably masked by the Si-O-Si band [119,172]. The peak centred at 900 cm⁻¹ (Figure 40a) can be referred to O-Si-H bonds [214]. The absorption bands located at 840 cm⁻¹ and 795 cm⁻¹ are attributed to CH₃ rocking vibrations in SiMe₃ and to CH₃ rocking vibrations in SiMe₂ respectively.

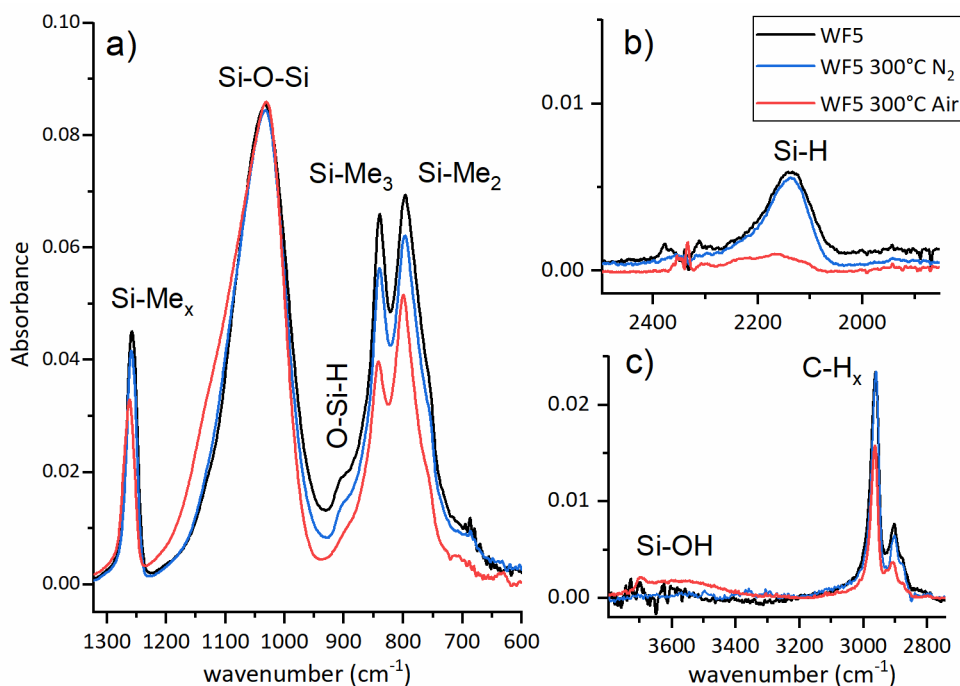


Figure 40: FTIR spectra of WF5, WF5 annealed under air and WF5 annealed under nitrogen flow in the a) 600-1320 cm^{-1} b) 1850-2500 cm^{-1} c) 2750-3800 cm^{-1} ranges

Figure 40 also presents the FTIR spectra of the annealed films. The WF5 annealed under nitrogen spectrum reveals slight modifications compared to the non-annealed material. The intensity decrease of the Si-Me_x, Si-Me₂ and Si-Me₃ absorption bands can be explained by the cleavage of some Si-C bonds after annealing. In addition, the slight modification in the Si-H peak and the decrease in the O-Si-H absorption band intensity suggests a cleavage of some Si-H bonds after thermal treatment. However, the FTIR spectrum of the WF5 annealed under air illustrates remarkable modifications compared to the non-annealed WF5 and the WF5 annealed under nitrogen flow. The important intensity decrease of the Si-Me_x, Si-Me₂, Si-Me₃ and C-H_x absorption bands and the drop in the Si-H and O-Si-H intensities are due to the Si-C and Si-H bonds cleavages respectively. Furthermore, the shift and the broadening shown of the Si-O-Si absorption band is probably due to the decrease in the Si-O-C peak intensity present near 945 cm^{-1} and the appearance of a Si-O-Si band at 1100 cm^{-1} that can be assimilated to a SiO_x structure. In addition, the new flat absorption band appeared between 3300 cm^{-1} and 3800 cm^{-1} is attributed to Si-OH bonds. In fact, the important carbon amount elimination and the introduction of oxygen atoms observed in the WF5 annealed under air are due to the presence of the oxygen atoms in the air that favours the cleavage of Si-C/Si-H bonds and the formation of Si-O bonds. These variations are not shown in the WF5 sample annealed under nitrogen due to the absence of oxygen atoms in the nitrogen atmosphere.

Figure 41 represents the elemental composition of the WF5 without and after annealing. The carbon percentage decreases slightly after annealing under nitrogen and strongly after annealing under air. Parallel, the oxygen percentage increases simultaneously with the carbon percentage decrease especially after a thermal treatment under air. However, the silicon percentage remains constant in the three samples. These modifications insure the oxidation of the material after thermal treatment under air by replacing some carbon atoms with oxygen atoms, which is consistent with the TGA and FTIR observations.

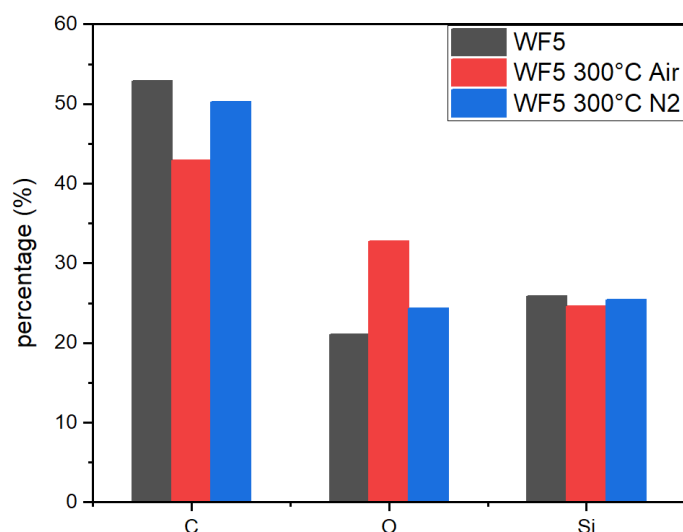


Figure 41: Elemental composition of the PP-HMDSO films without and after annealing

Refractive index:

The refractive index of the WF5 films without annealing, after annealing under nitrogen flow and air flow are presented in Figure 42. The films refractive index decreases from 1.53 for the as-deposited film to reach 1.50 and 1.47 for the deposits treated under nitrogen flow and airflow, respectively.

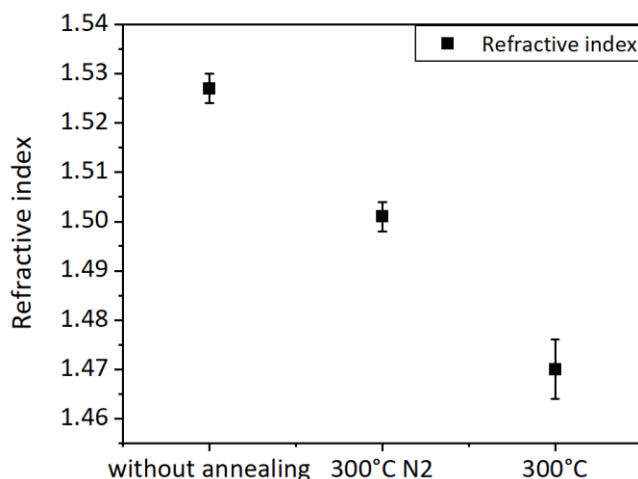


Figure 42: The refractive index of the non-annealed and annealed PP-HMDSO films

This refractive index decrease is probably due to the physical properties and/or chemical composition change after annealing. In fact, the thermal treatment under nitrogen can enhance the free volumes proportion leading to an increase of the chains spacing. Besides, the chains spacing increase can generate a refractive index decrease, since it is directly related to the dielectric constant of the film i.e. refractive index ($\epsilon=n^2$ in the visible optical range, n being the refractive index and ϵ is the dielectric constant). This phenomenon can be explained by the slight film swelling after annealing (around 3%) that was detected by ellipsometry (Figure S47 in SI, annex 3).

Furthermore, the important refractive index reduction observed after thermal treatment under air is also due to the incorporation of oxygen atoms shown in the chemical composition section. In fact, the oxygen atom incorporation into the films decreases the electronic polarizability due to bonds angle variations [117,118,201] leading to a decrease of the refractive index value.

Parallel to the refractive index decrease after annealing, one could expect a decrease of the films mass density with annealing. Now, the mass density values calculated are 1.38 g/cm^3 , 1.40 g/cm^3 and 1.45 g/cm^3 for the as-deposited, nitrogen-annealed and air-annealed respectively (almost falling within the estimated error range $\pm 0.03 \text{ g/cm}^3$) do not reveal a noticeable effect of annealing on this textural parameter. However, we can depict a tendency of density increase after annealing under airflow. In fact, even if the annealing makes globally increase chains spacing, the introduction of voluminous oxygen atoms is detrimental to the films density. Consequently, both effects compensate explaining the weak density variation.

Gas sorption:

Figure 43 shows the response of the WF5 thin films towards BTEX and ethanol vapours measured by Quartz crystal microbalance (QCM). The mass uptake value is obtained from the frequency shift measured by QCM using equation (41) and it represents the sorbed vapour mass by the thin films. The mass uptake error shown on each isotherm was taken as the standard deviation over three repeated measurements. As observed in Figure 43, the gas vapours mass uptake increases with the increase of the relative pressure P/P_0 for all the samples, P_0 being the saturated vapour pressure at the temperature of the quartz which is stabilized at 25°C. Figure 43 reveals fewer modifications after air annealing than after nitrogen annealing which explains the order of analysis followed.

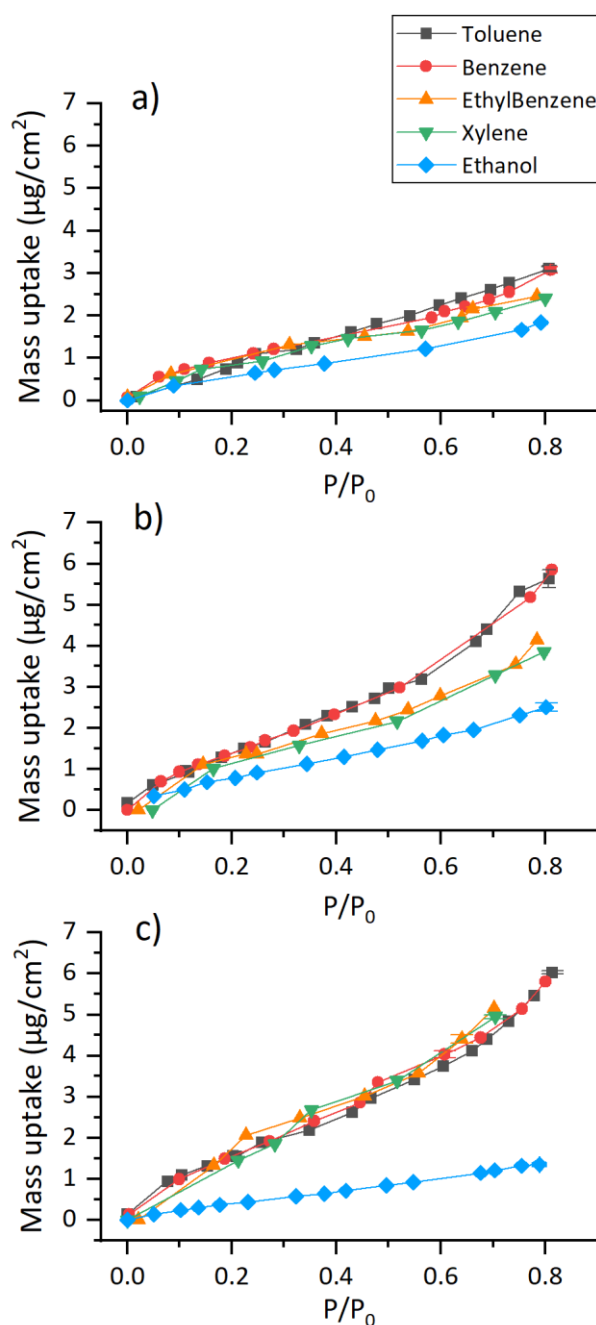


Figure 43: QCM measurements at 25°C showing the evolution of BTEX and ethanol vapour mass uptake for a) WF5 without annealing b) WF5 annealed at 300°C under air c) WF5 annealed at 300°C under N2 flow

Figure 43a illustrates the QCM results for the as-deposited film. A better sensitivity towards BTEX vapours is shown, compared to the sensitivity towards ethanol vapour. Indeed, this selectivity is explained by the hydrophobicity of organosilicon materials [199] surface that gives the films a higher affinity towards non-polar molecules (such as BTEX) compared to polar molecules (such as ethanol). Furthermore, the non-annealed WF5 sample shows a noticeable better affinity for benzene and toluene than for ethylbenzene and xylene. We assume that this selectivity is due to the difference in the BTEX molecules sizes. Therefore, we have

simulated all the BTEX molecules using DFT calculations (calculation details shown in SI, annex 3). After the geometry optimization, we have depicted the molecules size by measuring the distance between the most two distant atoms in each molecule (Figure S48 in SI annex 3). The measurements show that the molecules lengths for benzene, toluene, ethylbenzene and xylene are 4.95 Å, 5.89 Å, 7.21 Å and 6.95 Å respectively (estimated error between 0.01 and 0.02 Å). Thus, the size of the xylene and ethylbenzene molecules is quite similar and slightly larger than benzene and toluene molecules size. We can conclude that the penetration of the smaller molecules (benzene and toluene) is easier than the larger ones (ethylbenzene and xylene) despite the small differences between their size (all molecules are based on a single benzene ring). In fact, this difference can be significant since the free volume of polymer membranes such as PDMS is considered to be close to 5 Å [197].

The responses of the deposited films annealed at 300°C under air towards BTEX and ethanol vapours are shown in Figure 43b. The mass uptake at 0.8 P/P₀ for toluene/benzene increases from 3.1 µg/cm² to 5.8 µg/cm² and for ethylbenzene/xylene from 2.4 µg/cm² to 4.1 µg/cm², when compared to the non-annealed film. We assume that this remarkable increase in the sensitivity of the annealed materials towards BTEX vapours is due to the slight expansion of the material network after annealing (swelling of 2% after annealing detected by ellipsometry) that can increase the free volumes size in the material resulting in higher BTEX sorbed masses. Moreover, the selectivity between toluene/benzene and xylene/ethylbenzene is preserved after annealing. This selectivity preservation proposes a slight free volumes size expansion after annealing in such a way that the toluene/benzene molecules penetration in the films remains more favourable than the xylene/ethylbenzene molecules one. Furthermore, the ethanol sorbed mass also increases from 1.8 µg/cm² to 2.5 µg/cm² after annealing under air. This ethanol sensibility improvement can be explained by the incorporation of oxygen atoms in the material bulk shown in the chemical composition section (especially the SiOSi band shift and enlargement) and a consecutive increase in the polarity of the material.

Figure 43c presents the QCM results for the deposited film annealed at 300°C under nitrogen flow. Similarly, the mass uptake value of toluene/benzene vapours at 0.8 P/P₀ increases after annealing to attend 6 µg/cm². In addition, the mass uptake of xylene/ethylbenzene improves to attend 5 µg/cm² at 0.7 P/P₀. Beside the material network expansion mentioned above, this sensitivity improvement could be a result of the cleavage of some Si-(CH₃) bonds after annealing under nitrogen. In fact, several works showed that the high presence of methyl bonds

does not favour the sorption of BTEX vapour, thus a compromise between these bonds amount and the surface hydrophobicity should be taken into account [5,6,169].

However, the selectivity between BTEX vapours is lost i.e. identical isotherms are observed for all BTEX vapours. This selectivity loss is probably due to the obtaining of a more expanded material after annealing under nitrogen leading to an easier penetration of the larger BTEX molecules (ethylbenzene and xylene). In fact, the free volumes size enlargement is stronger at a thermal treatment under nitrogen than a thermal treatment under air because of the oxygen atoms absence in nitrogen atmosphere. In other words, the presence of the voluminous oxygen atoms (such as Si-OH bonds) in the material annealed under air can reduce the free volumes size compared to a material annealed under nitrogen.

Table 19 illustrates the selectivity ratio between BTEX and ethanol vapours for each sample. The selectivity ratio being the ratio between the BTEX vapours uptake mass and the ethanol vapour uptake mass at a fixed P/P_0 (0.7). Since the QCM results divided the sorption behaviour of the BTEX vapours into two groups, we have chosen toluene vapour as representative of toluene/benzene group and ethylbenzene as representative of ethylbenzene/xylene group in Table 19.

Table 19: Vapours selectivity calculated by the ratio of the mass uptakes at a same P/P_0

	$\Delta M_{\text{Toluene}} / \Delta M_{\text{Ethanol}}$ at $P/P_0 = 0.70$	$\Delta M_{\text{Ethylbenzene}} / \Delta M_{\text{Ethanol}}$ at $P/P_0 = 0.70$
WF5	1.7	1.38
WF5 300°C Air	2.09	1.56
WF5 300°C N ₂	4	4.2

The selectivity ratios between BTEX and ethanol increase after annealing especially under nitrogen. In fact, the thermal treatment under air ameliorates the BTEX sorption due to a less compact material after thermal treating. However, the replacement of some carbon atoms by oxygen atoms into the material network can improve the ethanol vapour sensitivity due to a change in the material hydrophobic behaviour. Thus, the selectivity ratio increase is limited after annealing under air. On the other hand, the selectivity ratios between BTEX and ethanol vapours rise strongly after a thermal treatment under nitrogen flow. In fact, this selectivity improvement is due to a less compact material and to the absence of the oxygen atoms incorporation in the film.

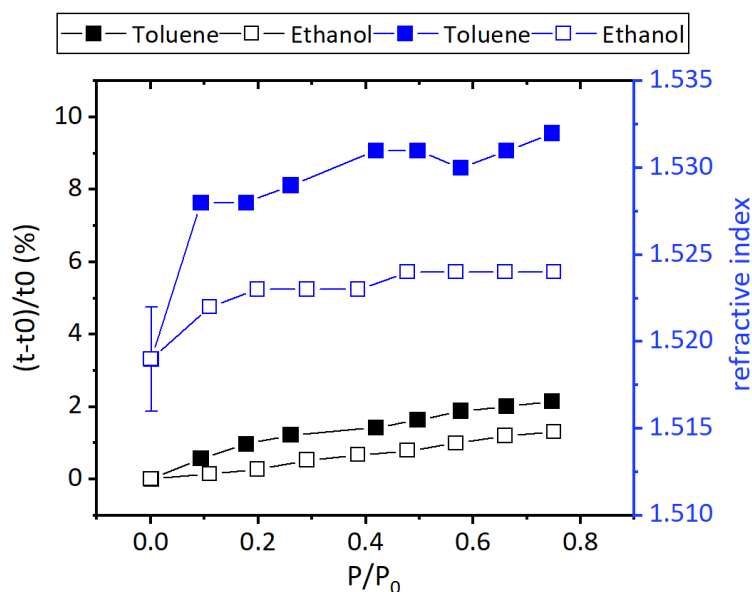


Figure 44: Thickness (black lines) and refractive index (blue lines) evolution of the non-annealed WF5 deposit while exposed to toluene (filled square) and ethanol (empty square) vapours

The film swelling (considered as the thickness increase occurred in the perpendicular direction to the substrate) and the refractive index change of the WF5 deposit without annealing when exposed to toluene and ethanol vapours are shown in Figure 44. The film thickness increases with P/P_0 during the sorption of both ethanol and toluene vapours. However, the swelling of the WF5 film is slightly higher when exposed to toluene vapour compared to the ethanol vapour. Thus, the toluene molecules sorption into the film is better than ethanol molecules sorption for all the P/P_0 values. Indeed, as shown in the QCM section (Figure 43), the WF5 deposit shows a higher affinity to toluene compared to ethanol due to the hydrophobic character of the WF5 film. The remarkable refractive index increase between 0.0 and 0.2 P/P_0 shown in Figure 44 is due to the free volumes (\sim microporosity, type I isotherm according to IUPAC) filling by toluene molecules during sorption. Whereas, the slight refractive index increase during ethanol vapour sorption (compared to toluene) can be explained by a weak free volumes filling i.e. weak affinity (due to material hydrophobicity), which is confirmed by the low film swelling when exposed to ethanol vapour.

Figure 45a and Figure 45b illustrates the thickness evolutions of WF5 annealed under air and WF5 annealed under nitrogen respectively during toluene and ethanol sorption. Both samples reveal a noticeable swelling (thickness enhancement) during toluene sorption up to 10% for WF5 annealed under air and 9% for WF5 annealed under nitrogen. This remarkable increase compared to the non-annealed deposit reveals a better penetration of toluene molecules into the material bulk due to the expansion of the film network after annealing. In addition, both samples reveal also a film swelling when exposed to ethanol vapour. However, WF5 annealed under air

illustrates a higher swelling rate during ethanol vapour sorption (around 6.5%) compared to WF5 non-annealed and WF5 annealed under nitrogen flow as shown in Figure 45a. Thus, WF5 annealed under air shows a better sensitivity towards ethanol vapour compared to the two other samples due to the incorporation of oxygen atoms in the material that improves its affinity towards ethanol molecules. As a result, the two annealed samples indicates a better affinity to toluene vapour compared to ethanol vapour due to their hydrophobic behaviour ($\text{WCA} \approx 95^\circ$). Whereas, WF5 annealed under nitrogen indicates the higher selectivity between toluene and ethanol vapours due to its larger free volume size and its weak affinity towards ethanol vapour, which is consistent with the QCM results.

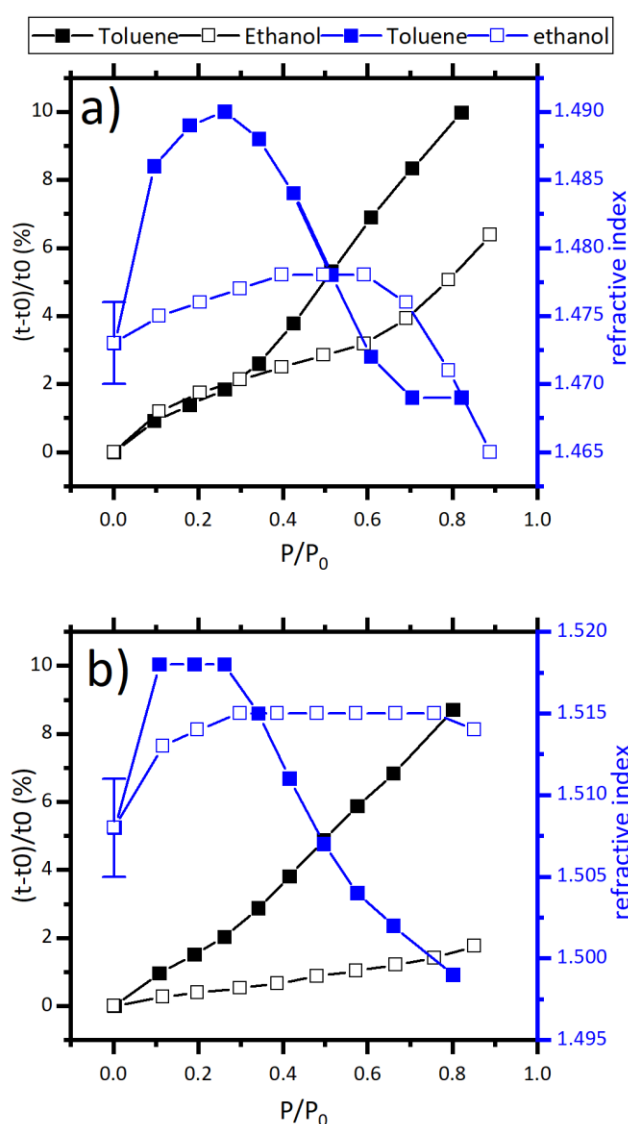


Figure 45: Thickness (black lines) and refractive index (blue lines) evolution of the a) WF5 annealed under air b) WF5 annealed under nitrogen flow, while exposed to toluene (filled square) and ethanol (empty square) vapours

Figure 45 also presents the variation of the refractive index during toluene and ethanol vapours sorption. At small P/P_0 , the refractive index rises when exposed to both vapours knowing that it is higher during toluene sorption. We should mention that during toluene sorption, the brutal refractive index increase between 0.0 and 0.25 P/P_0 is probably due to the filling of the free volumes sites occurred in this domain, which can be assimilated to the filling of microporosity shown in [151]. However, this phenomenon is visible in ellipsometry coupled to sorption because the sample was efficiently desorbed (turbo-molecular pump) compared to the QCM measurements (primary pump, less efficiency). As observed, this free volume filling is accompanied with a moderate swelling between 0.0 and 0.25 P/P_0 . Once the sites are filled with toluene (near 0.25 P/P_0), the swelling becomes more severe to attend higher percentages. Thus, the important films swelling generates a decrease in the global density of the films impregnated with the probe, which causes a decrease in the refractive index as shown in Figure 45. This phenomenon is not visible in the WF5 non-annealed sample (Figure 44) due to the weak film swelling. We assume that the toluene absorption is poor in the non-annealed sample. On the contrary, after annealing toluene molecules penetrates better in the whole film. The refractive index variation phenomenon is also shown in the WF5 annealed under air sample when exposed to ethanol vapor. In fact, this sample shows a high affinity to ethanol compared to the other samples. Therefore, the ethanol penetration in the material bulk is stronger. However, the refractive index decrease begins at higher P/P_0 values compared to toluene. This is due to the faster filling of toluene molecules into the free volumes sites compared to ethanol. In fact, the toluene fast filling is due to the film better affinity towards toluene compared to ethanol and due to the high toluene molecular volume compared to the ethanol molecular volume. However, the refractive index of the sample annealed under nitrogen increases between 0.0 and 0.25 P/P_0 and remains constant during ethanol sorption. This is due to the low film swelling that signifies a weak ethanol molecules penetration, thus a poor affinity. The global refractive index measured is a combination of the material and the penetrated probe refractive indexes, which explains the lower final global refractive index during ethanol sorption compared to toluene sorption (Figure 45a). This result is not observed in the WF5 annealed under nitrogen sample due to the slight ethanol penetration into this material.

Finally, we can describe the sorption mechanism of toluene in the annealed films by three steps: First, the brutal refractive index increase indicates the rapid adsorption of toluene molecules on the material surface (between 0.0 and 0.1). The second step, where the refractive index increases very slowly or remain constant (Figure 45b) corresponds to the required time for the toluene

molecules to cross the surface layer towards the bulk of the film (between 0.1 and 0.25). Finally, the third and last step, where the refractive index decreases corresponds to the film swelling allowing the penetration of additional probe mass.

Conclusion

In a previous work, we have determined the effect of the chemical composition and structure of the PP-HMDSO thin films on the sorption of VOCs vapors. In the present article, the deposit elaborated in the softest plasma conditions was thermally treated under air and nitrogen atmospheres in order to investigate its sorption of BTEX vapors in comparison to as-deposited films. A thermal study was carried out for the PP-HMDSO film to determine the optimal annealing temperature. Furthermore, the chemical composition of the treated samples was investigated and compared to the non-treated one. Physical properties such as refractive index and density of the films were also presented. In addition, the sorption mechanism of the PP-HMDSO films and the effects of the thermal treatment on the sorption of BTEX vapors were also investigated.

In conclusion, the thermal treatment modifies the chemical composition of the films especially under air flow. In fact, the percentage of oxygen atoms increases in the sample treated under air due to the formation of Si-OH bonds and the cleavage of some Si-C and Si-H bonds. However, the sample treated under nitrogen did not show important chemical composition modifications. The refractive index of the films decreased after thermal treatment due to the chemical composition change. Also, it can be linked to the modifications of the free volumes size and distribution after treatment. The chemical composition modification shown previously and the probable density variation after treatment affect both the sensitivity and the selectivity of the materials towards BTEX vapors. In fact, the PP-HMDSO thin films showed good sensitivity to all BTEX vapors compared to ethanol. After thermal treatment, the material sensitivity towards all BTEX increased strongly. As well, the material sorption selectivity to BTEX vapors compared to ethanol increased after treatment especially under nitrogen flow. This is due to a probable material density increase and to the oxidation of the material occurred after annealing under air that reduces its hydrophobicity. Finally, the selectivity ratio of sorption BTEX/ethanol is over 4 after the thermal treatment under nitrogen whereas the ration is only 1.5-2 depending on the BTEX vapor after the thermal treatment under air

Obviously, chemical and physical properties play important roles in the sorption of BTEX vapors into the organosilicon films. The sensitivity and the selectivity of the material were

improved after treatment due to an optimization of chemical composition, surface hydrophobicity and free volumes proportion/size. This work can be step forward towards the manufacturing of a novel BTEX gravimetric sensor.

Annex 3: Supplementary Information of article 3 (chapter 5)

Plasma polymerized organosilicon thin films for BTEX sensors applications

Ghadi Dakroub^{1,2}, Thomas Duguet¹, Corinne Lacaze-Dufaure¹, Stéphanie Roualdes², Arie Van der lee², Diane Rebiscoul³, Vincent Rouessac^{2}.*

¹ CIRIMAT, Université de Toulouse, CNRS, INP- ENSIACET 4 allée Emile Monso - BP44362, 31030 Toulouse cedex 4 - France.

² Institut Européen de Membranes, IEM UMR 5635, Univ Montpellier, ENSCM, CNRS, Montpellier, France

³ ICSM-UMR 5257 CEA-CNRS-UM- ENSCM, CEA, Bagnols-sur-Cèze, France

Thermal treatment at 250°C under air

Figure S46 show the FTIR spectra of the WF5 deposit without annealing and the WF5 after annealing at 250°C under air. The results show an intensity increase of the broad peak between 3200 cm⁻¹ and 3800 cm⁻¹ assimilated to the Si-OH absorption band. In addition, the C-H_x, Si-H and the chain terminations Si-Me₃ absorption bands reveal a decrease in the intensity after the thermal treatment. These modifications indicate an oxidation of the deposit by the cleavage of some hydrocarbon and Si-H bonds, and the formation of Si-OH bonds. Furthermore, the increase and the broadening of the Si-O-Si absorption band after annealing indicate the possible formation of thermal Si-O-Si chains.

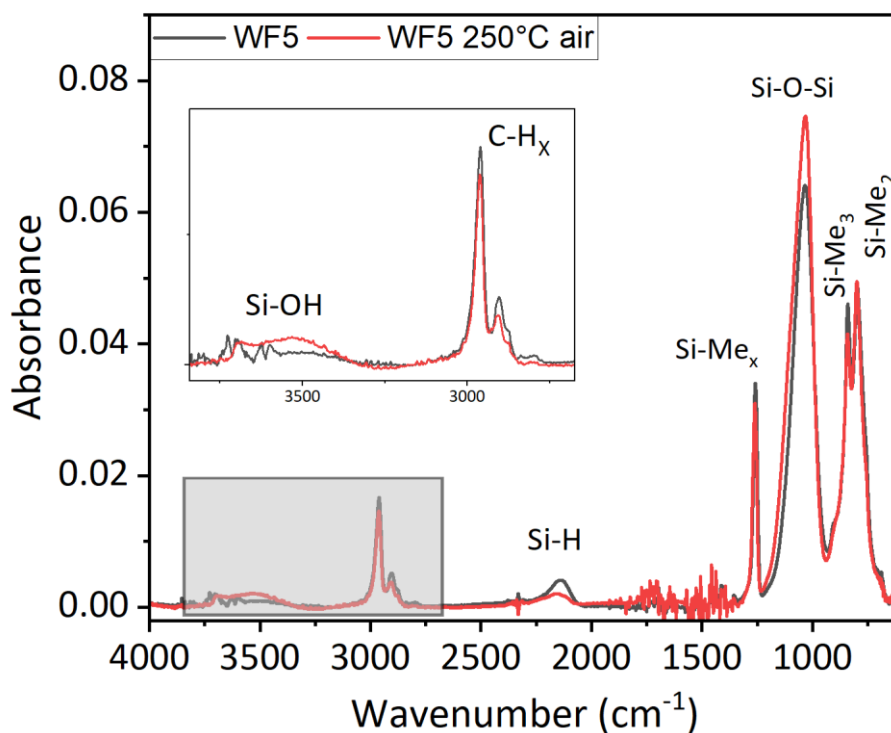


Figure S46: FTIR spectra of the WF5 as-deposited (black line) and annealed at 250°C under air.

Film swelling after annealing

Figure S47 represents the WF5 film swelling after annealing under nitrogen and air. In order to measure accurately the film thickness variation, the measurements were done before and after annealing on the same area on the sample. The results show an increase of 3% in the film thickness after annealing under both atmospheres. This thickness increase is probably a result of the film free volumes expansion after annealing.

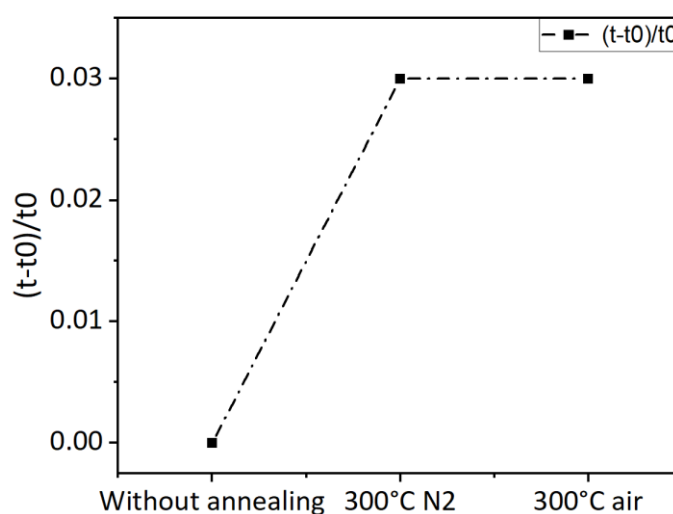


Figure S47: WF5 film swelling after thermal treatment

BTEX molecules calculations

The BTEX molecules geometry optimization was done by DFT calculations in Gaussian 09 package [156]. The B3LYP hybrid functional [215,216] was used with the def2TZVP basis set [152,153]. The NBO population analysis was chosen to determine the atomic charges [157]. After the geometry optimization the molecules size was determined by measuring the most two distant atom in the molecule. Figure S48 shows an example on how the p-xylene molecule size was measured after the geometrical optimization.

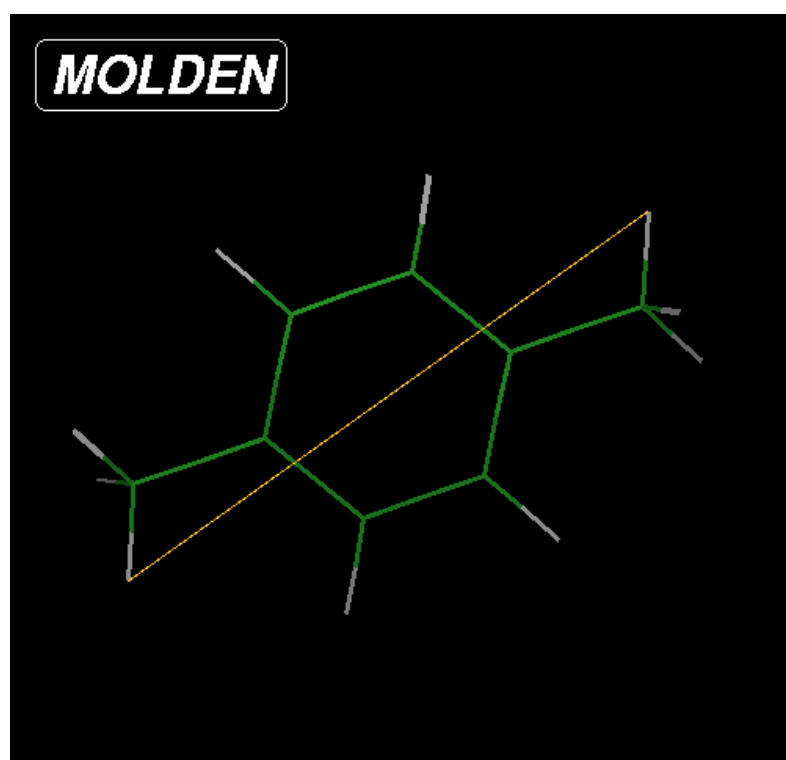


Figure S48: p-Xylene molecule size measurement

General conclusion

The objective of this work was to elaborate plasma organosilicon thin films for the detection of BTEX toxic vapours. This project aims to obtain an optimized thin film that could be integrated in the manufacturing of an on-site portable BTEX sensor.

The general notions and the bibliography discussed in the generalities chapter led us to draw up this problematic. In fact, based on the understanding of the concept of gas/solid interaction and thanks to the literature concerning the different types of gas sensors as well as the materials used for sensing applications, the organosilicon thin films elaborated by plasma deposition processes, notably PECVD, seems to be the most promising candidates for our objective. These materials are characterized by their flexible Si-O-Si chains that facilitates the molecules penetration. As well, their hydrophobicity favours the BTEX adsorption on the surface and their free volumes ensures the absorption and diffusion of analytes in the polymer network at room temperature. The great versatility of the PECVD technique for obtaining high quality materials, notably adherent, stable and uniform polymer-like thin films with a controllable chemical structure was also demonstrated. The interest of PECVD organosilicon deposits for detection of VOCs mainly BTEX has been confirmed by a state of the art on gas permeation and sensing membranes produced by this process, with a focus on the results obtained previously by our group. In addition, thanks to the literature review concerning the organosilicon physicochemical properties and the state of the art about the DFT-based simulation of XPS spectra a fine characterization methodology of the plasma organosilicon materials was built.

Experimentally speaking, a wide range of PP-HMDSO films at different plasma energy was first synthesized in order to investigate their bulk and surface chemical compositions. The films were elaborated using a MW-PECVD under different plasma conditions. Powerful techniques were used to determine the bulk chemical composition such as ^{29}Si quantitative solid-state NMR and FTIR spectroscopy. A combination between experimental XPS and DFT calculations was applied in order to investigate the PP-HMDSO surface chemical composition. It is noticeable that this work is one of very few attempts that combine DFT calculations with experimental XPS to characterize the surface of an organosilicon complex network.

The results have shown that the plasma energy plays a major role in the chemical composition of the films. Under soft plasma conditions (low plasma energy), the elaborated thin films are close to the conventional PDMS with a high concentration of SiOC_3 and linear SiO_2C_2 chains in the material bulk, while on the surface, the amount of the SiO_2C_2 chains is higher than the number of the SiOC_3 chain terminations. On the contrary, under hard plasma conditions (high plasma energy), the elaborated materials show a disorder in the bonds formation by the increase of the amount of Si-H and $\text{Si-CH}_2\text{-Si}$ bonds in the material bulk. Moreover, the number of the linear SiO_2C_2 chains that are close to PDMS decreases, while on the surface, the SiOC_3 concentration increases and the SiO_2C_2 decreases. The physical characterizations of films have shown that the plasma energy strongly affects the films free volumes proportion in the material and thus the value of the mass density. With the plasma energy increase, a denser material can be elaborated due to the disorder occurred in the bond formation, in particular, the introduction of carbon atoms in the material skeleton (formation $\text{Si-CH}_2\text{-Si}$ and Si-O-C). This fine characterization of the PP-HMDSO chemical compositions and structure/texture, has allowed us to investigate accurately the bulk and surface physico-chemical properties for a better understanding of the sorption phenomena of BTEX vapours into organosilicon membranes.

The second step of the experimental study has focused on the effects of the materials chemical composition and its physical properties on the sorption of VOCs vapours. Concerning the VOCs sorption, the chemical composition modification and the density variation with the plasma energy governs both the materials sensitivity and sorption selectivity towards the VOCs. In fact, and despite the small differences in the plasma conditions between the tested PP-HMDSO thin films (WF5, WF10 and WF20), these films have shown different sorption performances towards three VOCs vapours (ethanol, heptane, and toluene). The film elaborated with the lowest plasma energy (WF5) has shown the best sensitivity towards toluene with a good selectivity to other tested VOCs. In correlation with the physico-chemical characterizations, this is due to the low WF5 density and high hydrophobicity as well as the PDMS-like character of this deposit (high Si-O-Si bonds and $\text{Si-O}_2\text{C}_2$ amounts). As a partial conclusion, chemical composition, network structure and physical properties of the thin films play the key role in the vapours sorption into the organosilicon films. A combination of optimized free volumes size and surface hydrophobicity has enabled to depict, among a wide

range of PP-HMDSO, the film ensuring the best sensitivity/selectivity to toluene (BTEX) vapour compared to other VOCs.

Finally, the last step of the experimental study has aimed to improve the sorption efficiency of the previously optimized PP-HMDSO film towards the BTEX vapours and to understand its sorption mechanism. Thus, the optimized deposit (WF5) was thermally treated under air and nitrogen atmospheres. Physico-chemical properties of the annealed samples were determined and compared to the non-treated one. As well, the sorption mechanism of the PP-HMDSO film and the thermal treatment effects on its performance towards BTEX sorption were also investigated. After thermal treatment, modifications in the chemical composition of the films especially under airflow have been observed inherent to the material oxidation. Modifications of the free volumes size and distribution have also been induced by the thermal treatment. Consequently, the refractive index of the film has decreased. The comparison of sorption performances of the as-deposited film and the annealed ones have proved that the physico-chemical modifications implied by the thermal treatment affect both the sensitivity and the selectivity of the materials towards BTEX vapours. In fact, after annealing under air or nitrogen atmospheres, the sensitivity towards all BTEX vapors as well as the BTEX/ethanol selectivity have strongly increased. However, the BTEX/ethanol selectivity is higher for the material annealed under nitrogen. This is probably due to the material oxidation occurred after annealing under air that reduces its hydrophobicity.

Furthermore, the sorption mechanism of the BTEX vapours was analyzed by the variation of the film thickness and refractive index during the sorption. As a result, we can describe the BTEX sorption by a rapid adsorption on the surface in a first step. Then, in a second and last step, the adsorbed molecules penetrate moderately into the material bulk. This penetration leads to a film swelling allowing the absorption of additional BTEX molecules.

As a general conclusion, this work has attended its objective: plasma organosilicon thin films could be elaborated, accurately characterized and validated for gas sensing applications. Indeed, the optimization of the free volumes size and proportion as well as the chemical composition has led to the identification of the optimized material having the best sorption performance being suitable for BTEX detection. As well, the BTEX sorption mechanism into the whole material could be investigated. Thus, this work opens a path towards the manufacturing of a BTEX gas sensor by incorporating the studied material into miniaturized

gravimetric sensors such as Nano/Micro Electromechanical Systems (NEMS/MEMS), which strongly interests the industries working in the field of air quality control.

As perspectives, QCM measurements have to be completed by time detection of BTEX mixed with air at ambient pressure. In addition, other precursors than HMDSO (with in situ free volume such as cyclic siloxanes) or other preparation approaches (such as UV annealing or the porogen approach) could be investigated in order to enhance the materials porosity which could improve the sorption allowing phenomenon. Concerning the characterization of the materials, based on the refractive index variation, *i.e.* the dielectric constant variation, electrical sensing techniques could be tested in order to measure the dielectric constant variation during the vapours sorption and as a function of the working temperature. In fact, the BTEX detection should be achieved in all climatic conditions (temperature and humidity). Finally, basic lab-made QCM system should be replaced by miniaturized and more sensitive gravimetric sensors such as Nano/Mirco electromechanical systems (NEMS/MEMS).

References

- [1] N. Bruce, R. Perez-Padilla, R. Albalak, The health effects of indoor air pollution exposure in developing countries, *Geneva World Heal. Organ.* 11 (2002).
- [2] M. Kampa, E. Castanas, Human health effects of air pollution, *Environ. Pollut.* 151 (2008) 362–367.
- [3] Y. Ueno, T. Horiuchi, T. Morimoto, O. Niwa, Microfluidic device for airborne BTEX detection, *Anal. Chem.* 73 (2001) 4688–4693.
- [4] I. Lara-Lbeas, A. Rodríguez-Cuevas, C. Andrikopoulou, V. Person, L. Baldas, S. Colin, S. Le Calvé, Sub-ppb level detection of BTEX gaseous mixtures with a compact prototype GC equipped with a preconcentration unit, *Micromachines.* 10 (2019) 187.
- [5] J. El Sabahy, J. Berthier, F. Ricoul, V. Jousseau, Toward optimized SiOCH films for BTEX detection: Impact of chemical composition on toluene adsorption, *Sensors Actuators B Chem.* 258 (2018) 628–636.
- [6] M. Boutamine, A. Bellel, S. Sahli, Y. Segui, P. Raynaud, Hexamethyldisiloxane thin films as sensitive coating for quartz crystal microbalance based volatile organic compounds sensors, *Thin Solid Films.* 552 (2014) 196–203.
- [7] A. Bougharouat, A. Bellel, S. Sahli, Y. Ségui, P. Raynaud, Plasma polymerization of TEOS for QCM-based VOC vapor sensing, *Eur. Phys. Journal-Applied Phys.* 56 (2011).
- [8] M. Meyyappan, L. Delzeit, A. Cassell, D. Hash, Carbon nanotube growth by PECVD: a review, *Plasma Sources Sci. Technol.* 12 (2003) 205.
- [9] C.A. Lasorsa, P.M. Perillo, P.J. Morando, Protective SixOyCz coatings on steel prepared by plasma activated chemical vapour deposition, *Surf. Coatings Technol.* 204 (2010) 2813–2816.
- [10] B.T. Raut, P.R. Godse, S.G. Pawar, M.A. Chougule, D.K. Bandgar, V.B. Patil, Novel method for fabrication of polyaniline–CdS sensor for H₂S gas detection, *Measurement.* 45 (2012) 94–100.
- [11] I. Buka, S. Koranteng, A.R. Osornio-Vargas, The effects of air pollution on the health of children, *Paediatr. Child Health.* 11 (2006) 513–516.
- [12] W.H. Organization, Ambient air pollution: a global assessment of exposure and burden of disease, World Health Organization, Geneva PP - Geneva, n.d. <https://apps.who.int/iris/handle/10665/250141>.
- [13] J. El Sabahy, Couches minces organo-siliciées déposées par PECVD pour la fonctionnalisation de capteurs de gaz, Université Grenoble Alpes, 2015.
- [14] K. Badjagbo, S. Loranger, S. Moore, R. Tardif, S. Sauve, BTEX exposures among automobile mechanics and painters and their associated health risks, *Hum. Ecol. Risk Assess. An Int. J.* 16 (2010) 301–316.
- [15] N. Baimatova, B. Kenessov, J.A. Koziel, L. Carlsen, M. Bektassov, O.P. Demyanenko, Simple and accurate quantification of BTEX in ambient air by SPME and GC–MS, *Talanta.* 154 (2016) 46–52.
- [16] P. Irigaray, J.A. Newby, R. Clapp, L. Hardell, V. Howard, L. Montagnier, S. Epstein, D. Belpomme, Lifestyle-related factors and environmental agents causing cancer: an overview, *Biomed. Pharmacother.* 61 (2007) 640–658.
- [17] S. Hazrati, R. Rostami, M. Farjaminezhad, M. Fazlzadeh, Preliminary assessment of BTEX concentrations in indoor air of residential buildings and atmospheric ambient air in Ardabil, Iran, *Atmos. Environ.* 132 (2016) 91–97.
- [18] F. Leusch, M. Bartkow, A Short Primer on Benzene, Toluene, Ethylbenzene and Xylenes (BTEX) in the Environment and in Hydraulic Fracturing Fluids, *Smart Water Res Cent.*

- 189 (2010) 1–8.
- [19] R. Kandyala, S.P.C. Raghavendra, S.T. Rajasekharan, Xylene: An overview of its health hazards and preventive measures, *J. Oral Maxillofac. Pathol. JOMFP*. 14 (2010) 1.
 - [20] A. Favard, *Multicapteurs intégrés pour la détection des BTEX*, Aix-Marseille, 2018.
 - [21] J. Rouquerol, F. Rouquerol, P. Llewellyn, G. Maurin, K.S.W. Sing, *Adsorption by powders and porous solids: principles, methodology and applications*, Academic press, 2013.
 - [22] W.C. Martin, W.L. Wiese, *Atomic, Molecular, and Optical Physics Handbook*, 1996.
 - [23] R.I. Masel, *Principles of adsorption and reaction on solid surfaces*, John Wiley & Sons, 1996.
 - [24] R. Kecili, C.M. Hussain, Mechanism of adsorption on nanomaterials, in: *Nanomater. Chromatogr.*, Elsevier, 2018: pp. 89–115.
 - [25] A. Dąbrowski, Adsorption—from theory to practice, *Adv. Colloid Interface Sci.* 93 (2001) 135–224.
 - [26] G. Limousin, J.-P. Gaudet, L. Charlet, S. Szenknect, V. Barthes, M. Krimissa, Sorption isotherms: A review on physical bases, modeling and measurement, *Appl. Geochemistry*. 22 (2007) 249–275.
 - [27] M.D. Donohue, G.L. Aranovich, Classification of Gibbs adsorption isotherms, *Adv. Colloid Interface Sci.* 76 (1998) 137–152.
 - [28] M. Thommes, K. Kaneko, A. V Neimark, J.P. Olivier, F. Rodriguez-Reinoso, J. Rouquerol, K.S.W. Sing, Physisorption of gases, with special reference to the evaluation of surface area and pore size distribution (IUPAC Technical Report), *Pure Appl. Chem.* 87 (2015) 1051–1069.
 - [29] L.-M. Sun, F. Meunier, Adsorption: aspects théoriques, *Tech. l'ingénieur. Technol. l'eau*. 2 (2003).
 - [30] I. Langmuir, The adsorption of gases on plane surfaces of glass, mica and platinum., *J. Am. Chem. Soc.* 40 (1918) 1361–1403.
 - [31] G.A. Somorjai, The evolution of surface chemistry. A personal view of building the future on past and present accomplishments, (2002).
 - [32] I. Langmuir, The constitution and fundamental properties of solids and liquids. Part I. Solids., *J. Am. Chem. Soc.* 38 (1916) 2221–2295.
 - [33] G. Maurin, *Modelling of Physisorption in Porous Solids*, Academic Press, 2013.
 - [34] F. Rouquerol, J. Rouquerol, P. Llewellyn, R. Denoyel, Texture des matériaux divisés-aire spécifique des matériaux pulvérulents ou nanoporeux, *Tech. l'Ingénieur*. (2017) 50–54.
 - [35] S. Brunauer, P.H. Emmett, E. Teller, Adsorption of gases in multimolecular layers, *J. Am. Chem. Soc.* 60 (1938) 309–319.
 - [36] K.S.W. Sing, F. Rouquerol, J. Rouquerol, Classical interpretation of physisorption isotherms at the gas-solid interface, *Adsorpt. by Powders Porous Solids Princ. Methodol. Appl.* 2 (2013) 159–189.
 - [37] M. Doi, *Introduction to polymer physics*, Oxford university press, 1996.
 - [38] P.J. Flory, *Principles of polymer chemistry*, Cornell University Press, 1953.
 - [39] G. Korotcenkov, *Handbook of gas sensor materials*, Springer, 2013.
 - [40] G. Korotcenkov, S. Do Han, J.R. Stetter, Review of electrochemical hydrogen sensors, *Chem. Rev.* 109 (2009) 1402–1433.
 - [41] J.R. Stetter, G. Korotcenkov, X. Zeng, Y. Tang, Y. Liu, Electrochemical gas sensors: fundamentals, fabrication and parameters, *Chem. Sensors Compr. Sens. Technol.* 5 (2011) 1–89.
 - [42] S. Karthikeyan, H.M. Pandya, M.U. Sharma, K. Gopal, Gas sensors-a review, *J. Environ. Nanotechnol.* 4 (2015) 1–14.

- [43] H. Weingärtner, *An Introduction to Aqueous Electrolyte Solutions*. By Margaret Robson Wright., (2008).
- [44] M.T. Carter, J.R. Stetter, M.W. Findlay, V. Patel, Printed amperometric gas sensors, *ECS Trans.* 50 (2013) 211.
- [45] T. Aldhafeeri, M.-K. Tran, R. Vrolyk, M. Pope, M. Fowler, A review of methane gas detection sensors: Recent developments and future perspectives, *Inventions*. 5 (2020) 28.
- [46] T. Seiyama, A. Kato, K. Fujiishi, M. Nagatani, A new detector for gaseous components using semiconductive thin films., *Anal. Chem.* 34 (1962) 1502–1503.
- [47] P. Shailesh, C. Manik, P. Sanjay, R. Bharat, D. Dhanaji, P. Pramod, S. Shashwati, J. Pradeep, P. Vikas, Fabrication of nanocrystalline TiO₂ thin film ammonia vapor sensor, *J. Sens. Technol.* 2011 (2011).
- [48] V. Patil, S. Pawar, M. Chougule, B. Raut, R. Mulik, S. Sen, New Method for Fabrication of Co³⁺ O⁴⁻ Thin Film Sensors: Structural, Morphological and Optoelectronic Properties, *Sensors & Transducers*. 128 (2011) 100.
- [49] Y. Wu, B. Yao, C. Yu, Y. Rao, Optical graphene gas sensors based on microfibers: a review, *Sensors*. 18 (2018) 941.
- [50] C.K. Ho, M.T. Itamura, M. Kelley, R.C. Hughes, Review of chemical sensors for in-situ monitoring of volatile contaminants, *Sandia Rep.* 28 (2001).
- [51] J.H. Lee, C.L. Tsai, C.S. Fann, S.H. Wang, Design of an acousto-magnetic oxygen sensor, *J. Med. Biol. Eng.* 22 (2002) 193–198.
- [52] P.T. Meriläinen, A differential paramagnetic sensor for breath-by-breath oximetry, *J. Clin. Monit.* 6 (1990) 65–73.
- [53] R. Jaaniso, O.K. Tan, *Semiconductor gas sensors*, Elsevier, 2013.
- [54] E. Spain, A. Venkatanarayanan, Review of physical principles of sensing and types of sensing materials, (2014).
- [55] S. Fanget, S. Hentz, P. Puget, J. Arcamone, M. Matheron, E.D. Colinet, P. Andreucci, L. Duraffourg, E. Myers, M.L. Roukes, Gas sensors based on gravimetric detection—A review, *Sensors Actuators B Chem.* 160 (2011) 804–821.
- [56] F.M. Battiston, J.-P. Ramseyer, H.P. Lang, M.K. Baller, C. Gerber, J.K. Gimzewski, E. Meyer, H.-J. Güntherodt, A chemical sensor based on a microfabricated cantilever array with simultaneous resonance-frequency and bending readout, *Sensors Actuators B Chem.* 77 (2001) 122–131.
- [57] W.H. King, Piezoelectric sorption detector., *Anal. Chem.* 36 (1964) 1735–1739.
- [58] C.K. McGinn, Z.A. Lamport, I. Kymissis, Review of gravimetric sensing of volatile organic compounds, *ACS Sensors*. 5 (2020) 1514–1534.
- [59] A. Mirzaei, S.G. Leonardi, G. Neri, Detection of hazardous volatile organic compounds (VOCs) by metal oxide nanostructures-based gas sensors: A review, *Ceram. Int.* 42 (2016) 15119–15141.
- [60] J.M. Walker, S.A. Akbar, P.A. Morris, Synergistic effects in gas sensing semiconducting oxide nano-heterostructures: A review, *Sensors Actuators B Chem.* 286 (2019) 624–640.
- [61] P.T. Moseley, Progress in the development of semiconducting metal oxide gas sensors: a review, *Meas. Sci. Technol.* 28 (2017) 82001.
- [62] X. Wang, F. Cui, J. Lin, B. Ding, J. Yu, S.S. Al-Deyab, Functionalized nanoporous TiO₂ fibers on quartz crystal microbalance platform for formaldehyde sensor, *Sensors Actuators B Chem.* 171 (2012) 658–665.
- [63] N. Kilinc, O. Cakmak, A. Kosemen, E. Ermek, S. Ozturk, Y. Yerli, Z.Z. Ozturk, H. Urey, Fabrication of 1D ZnO nanostructures on MEMS cantilever for VOC sensor application, *Sensors Actuators B Chem.* 202 (2014) 357–364.
- [64] S.E. Diltemiz, K. Ecevit, High-performance formaldehyde adsorption on CuO/ZnO composite nanofiber coated QCM sensors, *J. Alloys Compd.* 783 (2019) 608–616.

- [65] J. Xie, H. Wang, M. Duan, QCM chemical sensor based on ZnO colloid spheres for the alcohols, *Sensors Actuators B Chem.* 203 (2014) 239–244.
- [66] C. Wang, L. Yin, L. Zhang, D. Xiang, R. Gao, Metal oxide gas sensors: sensitivity and influencing factors, *Sensors.* 10 (2010) 2088–2106.
- [67] S.J. Ippolito, A. Ponzoni, K. Kalantar-Zadeh, W. Wlodarski, E. Comini, G. Faglia, G. Sberveglieri, Layered WO₃/ZnO/36° LiTaO₃ SAW gas sensor sensitive towards ethanol vapour and humidity, *Sensors Actuators B Chem.* 117 (2006) 442–450.
- [68] X. Xu, J. Wang, Y. Long, Zeolite-based materials for gas sensors, *Sensors.* 6 (2006) 1751–1764.
- [69] S. Brosillon, M.-H. Manero, J.-N. Foussard, Adsorption of acetone/heptane gaseous mixtures on zeolite co-adsorption equilibria and selectivities, *Environ. Technol.* 21 (2000) 457–465.
- [70] X. Ji, W. Yao, J. Peng, N. Ren, J. Zhou, Y. Huang, Evaluation of Cu-ZSM-5 zeolites as QCM sensor coatings for DMMP detection, *Sensors Actuators B Chem.* 166 (2012) 50–55.
- [71] Z. Liron, N. Kaushansky, G. Frishman, D. Kaplan, J. Greenblatt, The polymer-coated SAW sensor as a gravimetric sensor, *Anal. Chem.* 69 (1997) 2848–2854.
- [72] D.S. Ballantine Jr, R.M. White, S.J. Martin, A.J. Ricco, E.T. Zellers, G.C. Frye, H. Wohltjen, *Acoustic wave sensors: theory, design and physico-chemical applications*, Elsevier, 1996.
- [73] L. Zajíčková, V. Buršíková, Z. Kučerová, J. Franclova, P. Šťáhel, V. Peřina, A. Mackova, Organosilicon thin films deposited by plasma enhanced CVD: Thermal changes of chemical structure and mechanical properties, *J. Phys. Chem. Solids.* 68 (2007) 1255–1259.
- [74] H.O. Finklea, M.A. Phillippi, E. Lompert, J.W. Grate, Highly sorbent films derived from Ni (SCN) 2 (4-picoline) 4 for the detection of chlorinated and aromatic hydrocarbons with quartz crystal microbalance sensors, *Anal. Chem.* 70 (1998) 1268–1276.
- [75] Y. Fu, H.O. Finklea, Quartz crystal microbalance sensor for organic vapor detection based on molecularly imprinted polymers, *Anal. Chem.* 75 (2003) 5387–5393.
- [76] J.W. Grate, A. Snow, D.S. Ballantine, H. Wohltjen, M.H. Abraham, R.A. McGill, P. Sasson, Determination of partition coefficients from surface acoustic wave vapor sensor responses and correlation with gas-liquid chromatographic partition coefficients, *Anal. Chem.* 60 (1988) 869–875.
- [77] A. Mirmohseni, V. Hassanzadeh, Application of polymer-coated quartz crystal microbalance (QCM) as a sensor for BTEX compounds vapors, *J. Appl. Polym. Sci.* 79 (2001) 1062–1066.
- [78] M. Maute, S. Raible, F.E. Prins, D.P. Kern, U. Weimar, W. Göpel, Fabrication and application of polymer coated cantilevers as gas sensors, *Microelectron. Eng.* 46 (1999) 439–442.
- [79] K.D. Schierbaum, A. Hierlemann, W. Göpel, Modified polymers for reliable detection of organic solvents: thermodynamically controlled selectivities and sensitivities, *Sensors Actuators B Chem.* 19 (1994) 448–452.
- [80] M. Konuma, *Film deposition by plasma techniques*, Springer Science & Business Media, 2012.
- [81] A. Szekeres, K. Kirov, S. Alexandrova, Plasma photoresist stripping in a planar reactor, *Phys. Status Solidi. A, Appl. Res.* 63 (1981) 371–374.
- [82] C. Wang, G. Hsiue, Oxidation of polyethylene surface by glow discharge and subsequent graft copolymerization of acrylic acid, *J. Polym. Sci. Part A Polym. Chem.* 31 (1993) 1307–1314.
- [83] D. Hegemann, H. Brunner, C. Oehr, Plasma treatment of polymers for surface and

- adhesion improvement, *Nucl. Instruments Methods Phys. Res. Sect. B Beam Interact. with Mater. Atoms.* 208 (2003) 281–286.
- [84] H. Yasuda, Glow discharge polymerization, *J. Polym. Sci. Macromol. Rev.* 16 (1981) 199–293.
- [85] V. Rouessac, Contribution à l'étude microstructurale des couches minces supportées a-SiOXY: H et autres membranes poreuses, (2007).
- [86] F. Delachat, M. Carrada, G. Ferblantier, J.J. Grob, A. Slaoui, Properties of silicon nanoparticles embedded in SiN_x deposited by microwave-PECVD, *Nanotechnology.* 20 (2009) 415608.
- [87] M.R. Wertheimer, M. Moisan, Processing of electronic materials by microwave plasma, *Pure Appl. Chem.* 66 (1994) 1343–1352.
- [88] W.J. Soppe, A.C.W. Biebericher, C. Devilee, H. Donker, H. Schlemm, High rate growth of micro-crystalline silicon by microwave-PECVD, in: 3rd World Conf. On Photovoltaic Energy Conversion, 2003. Proc., IEEE, 2003: pp. 1655–1658.
- [89] H. Yasuda, T. Hsu, Some aspects of plasma polymerization investigated by pulsed RF discharge, *J. Polym. Sci. Polym. Chem. Ed.* 15 (1977) 81–97.
- [90] A. Colas, Silicones: preparation, properties and performance, Dow Corning, Life Sci. (2005).
- [91] F. Benitez, E. Martinez, J. Esteve, Improvement of hardness in plasma polymerized hexamethyldisiloxane coatings by silica-like surface modification, *Thin Solid Films.* 377 (2000) 109–114.
- [92] D.S. Wavhal, J. Zhang, M.L. Steen, E.R. Fisher, Investigation of gas phase species and deposition of SiO₂ films from HMDSO/O₂ plasmas, *Plasma Process. Polym.* 3 (2006) 276–287.
- [93] S.E. Alexandrov, N. McSporran, M.L. Hitchman, Remote AP-PECVD of Silicon Dioxide Films from Hexamethyldisiloxane (HMDSO), *Chem. Vap. Depos.* 11 (2005) 481–490.
- [94] G. Borvon, A. Goulet, A. Granier, G. Turban, Analysis of low-k organosilicon and low-density silica films deposited in HMDSO plasmas, *Plasma Polym.* 7 (2002) 341–352.
- [95] S. Roualdes, Elaboration par PECVD et caractérisation de membranes polysiloxanes plasma pour la perméation gazeuse, (2000).
- [96] C. Saulou, B. Despax, P. Raynaud, S. Zanna, P. Marcus, M. Mercier-Bonin, Plasma deposition of organosilicon polymer thin films with embedded nanosilver for prevention of microbial adhesion, *Appl. Surf. Sci.* 256 (2009) S35–S39.
- [97] S. Asadollahi, J. Profili, M. Farzaneh, L. Stafford, Development of organosilicon-based superhydrophobic coatings through atmospheric pressure plasma polymerization of HMDSO in nitrogen plasma, *Materials (Basel).* 12 (2019) 219.
- [98] S. Roualdes, A. Van der Lee, R. Berjoan, J. Sanchez, J. Durand, Gas separation properties of organosilicon plasma polymerized membranes, *AIChE J.* 45 (1999) 1566–1575.
- [99] J. Perrin, O. Leroy, M.C. Bordage, Cross-Sections, Rate Constants and Transport Coefficients in Silane Plasma Chemistry, *Contrib. to Plasma Phys.* 36 (1996) 3–49.
- [100] A.S.M. de Freitas, C.C. Maciel, J.S. Rodrigues, R.P. Ribeiro, A.O. Delgado-Silva, E.C. Rangel, Organosilicon films deposited in low-pressure plasma from hexamethyldisiloxane—A review, *Vacuum.* (2021) 110556.
- [101] P. Dimitrakellis, E. Gogolides, Hydrophobic and superhydrophobic surfaces fabricated using atmospheric pressure cold plasma technology: A review, *Adv. Colloid Interface Sci.* 254 (2018) 1–21.
- [102] N. Benissad, C. Boisse-Laporte, C. Vallée, A. Granier, A. Goulet, Silicon dioxide deposition in a microwave plasma reactor, *Surf. Coatings Technol.* 116 (1999) 868–873.

- [103] M.R. Alexander, F.R. Jones, R.D. Short, Mass spectral investigation of the radio-frequency plasma deposition of hexamethyldisiloxane, *J. Phys. Chem. B.* 101 (1997) 3614–3619.
- [104] M.R. Alexander, F.R. Jones, R.D. Short, Radio-frequency hexamethyldisiloxane plasma deposition: a comparison of plasma-and deposit-chemistry, *Plasmas Polym.* 2 (1997) 277–300.
- [105] K. Aumaille, C. Vallée, A. Granier, A. Goullet, F. Gaboriau, G. Turban, A comparative study of oxygen/organosilicon plasmas and thin SiO_xCyHz films deposited in a helicon reactor, *Thin Solid Films.* 359 (2000) 188–196.
- [106] P. Raynaud, B. Despax, Y. Segui, H. Caquineau, FTIR plasma phase analysis of hexamethyldisiloxane discharge in microwave multipolar plasma at different electrical powers, *Plasma Process. Polym.* 2 (2005) 45–52.
- [107] M.R. Alexander, R.D. Short, F.R. Jones, W. Michaeli, C.J. Blomfield, A study of HMDSO/O₂ plasma deposits using a high-sensitivity and-energy resolution XPS instrument: curve fitting of the Si 2p core level, *Appl. Surf. Sci.* 137 (1999) 179–183.
- [108] G. Socrates, *Infrared and Raman characteristic group frequencies: tables and charts*, John Wiley & Sons, 2004.
- [109] C.J. Hall, T. Ponnusamy, P.J. Murphy, M. Lindberg, O.N. Antzutkin, H.J. Griesser, A solid-state nuclear magnetic resonance study of post-plasma reactions in organosilicone microwave plasma-enhanced chemical vapor deposition (PECVD) coatings, *ACS Appl. Mater. Interfaces.* 6 (2014) 8353–8362.
- [110] P.-Y. Mabboux, K.K. Gleason, Chemical bonding structure of low dielectric constant Si: O: C: H films characterized by solid-state NMR, *J. Electrochem. Soc.* 152 (2005) F7–F13.
- [111] J. Petersen, R. Bechara, J. Bardon, T. Fouquet, F. Ziarelli, L. Daheron, V. Ball, V. Toniazzo, M. Michel, A. Dinia, Atmospheric Plasma Deposition Process: A Versatile Tool for the Design of Tunable Siloxanes-Based Plasma Polymer Films, *Plasma Process. Polym.* 8 (2011) 895–903.
- [112] M.R. Alexander, R.D. Short, F.R. Jones, M. Stollenwerk, J. Zabold, W. Michaeli, An X-ray photoelectron spectroscopic investigation into the chemical structure of deposits formed from hexamethyldisiloxane/oxygen plasmas, *J. Mater. Sci.* 31 (1996) 1879–1885.
- [113] S. Roualdes, R. Berjoan, J. Durand, ²⁹Si NMR and Si2p XPS correlation in polysiloxane membranes prepared by plasma enhanced chemical vapor deposition, *Sep. Purif. Technol.* 25 (2001) 391–397.
- [114] L. O'Hare, B. Parbhoo, S.R. Leadley, Development of a methodology for XPS curve-fitting of the Si 2p core level of siloxane materials, *Surf. Interface Anal. An Int. J. Devoted to Dev. Appl. Tech. Anal. Surfaces, Interfaces Thin Film.* 36 (2004) 1427–1434.
- [115] S. Roualdes, J. Sanchez, J. Durand, Gas diffusion and sorption properties of polysiloxane membranes prepared by PECVD, *J. Memb. Sci.* 198 (2002) 299–310.
- [116] M. Branecky, N. Aboualigaedari, V. Cech, Plasma nanotechnology for controlling chemical and physical properties of organosilicon nanocoatings, *Mater. Today Commun.* 24 (2020) 101234.
- [117] S. Gallis, V. Nikas, M. Huang, E. Eisenbraun, A.E. Kaloyeros, Comparative study of the effects of thermal treatment on the optical properties of hydrogenated amorphous silicon-oxy-carbide, *J. Appl. Phys.* 102 (2007) 24302.
- [118] C.S. Yang, K.S. Oh, C.K. Choi, H.J. Lee, K.M. Lee, A study on the dielectric components of SiOC (-H) composite films deposited by using BTMSM/O 2-ICPCVD, *J. Korean Phys. Soc.* 44 (2004) 1102–1107.
- [119] Y. Liu, F. Elam, E. Zoethout, S. Starostin, R. Van de Sanden, H. De Vries, Atmospheric-

- pressure silica-like thin film deposition using 200 kHz/13.56 MHz dual frequency excitation, *J. Phys. D. Appl. Phys.* (2019).
- [120] D. Mitev, E. Radeva, D. Peshev, M. Cook, L. Peeva, PECVD polymerised coatings on thermo-sensitive plastic support, in: *J. Phys. Conf. Ser.*, IOP Publishing, 2016: p. 12014.
- [121] R. Morent, N. De Geyter, S. Van Vlierberghe, P. Dubruel, C. Leys, E. Schacht, Organic–inorganic behaviour of HMDSO films plasma-polymerized at atmospheric pressure, *Surf. Coatings Technol.* 203 (2009) 1366–1372.
- [122] N. De Geyter, R. Morent, S. Van Vlierberghe, P. Dubruel, C. Leys, E. Schacht, Plasma polymerisation of siloxanes at atmospheric pressure, *Surf. Eng.* 27 (2011) 627–633.
- [123] M. Bashir, S. Bashir, Hydrophobic–hydrophilic character of hexamethyldisiloxane films polymerized by atmospheric pressure plasma jet, *Plasma Chem. Plasma Process.* 35 (2015) 739–755.
- [124] S. Kurosawa, B.-G. Choi, J.-W. Park, H. Aizawa, K.-B. Shim, K. Yamamoto, Synthesis and characterization of plasma-polymerized hexamethyldisiloxane films, *Thin Solid Films.* 506 (2006) 176–179.
- [125] J.A. Theil, J.G. Brace, R.W. Knoll, Carbon content of silicon oxide films deposited by room temperature plasma enhanced chemical vapor deposition of hexamethyldisiloxane and oxygen, *J. Vac. Sci. Technol. A Vacuum, Surfaces, Film.* 12 (1994) 1365–1370.
- [126] C. Brunon, E. Chadeau, N. Oulahal, C. Grossiord, L. Dubost, F. Simon, F. Bessueille, P. Degraeve, D. Leonard, Antimicrobial finishing of textiles intended for food processing industry by plasma enhanced chemical vapor deposition–physical vapor deposition of Ag-SiOCH composites coated with Al_xO_y or SiOCH encapsulation layers, *Thin Solid Films.* 628 (2017) 132–141.
- [127] J.G.S. Souza, M. Bertolini, R.C. Costa, J.M. Cordeiro, B.E. Nagay, A.B. De Almeida, B. Retamal-Valdes, F.H. Nociti, M. Feres, E.C. Rangel, Targeting pathogenic biofilms: newly developed superhydrophobic coating favors a host-compatible microbial profile on the titanium surface, *ACS Appl. Mater. Interfaces.* 12 (2020) 10118–10129.
- [128] D. Li, S. Elisabeth, A. Granier, M. Carette, A. Goulet, J. Landesman, Structural and optical properties of PECVD TiO₂–SiO₂ mixed oxide films for optical applications, *Plasma Process. Polym.* 13 (2016) 918–928.
- [129] R. Amri, S. Sahel, C. Manaa, L. Bouaziz, D. Gamra, M. Lejeune, M. Clin, K. Zellama, H. Bouchriha, Experimental evidence of the photonic band gap in hybrid one-dimensional photonic crystal based on a mixture of (HMDSO, O₂), *Superlattices Microstruct.* 96 (2016) 273–281.
- [130] R.C.C. Rangel, N.C. Cruz, E.C. Rangel, Role of the plasma activation degree on densification of organosilicon films, *Materials (Basel).* 13 (2020) 25.
- [131] P. Goyal, J. Hong, F. Haddad, J.-L. Maurice, P.R. i Cabarrocas, E. Johnson, Use of hexamethyldisiloxane for p-type microcrystalline silicon oxycarbide layers, *EPJ Photovoltaics.* 7 (2016) 70301.
- [132] R. Charifou, E. Espuche, F. Gouanvé, L. Dubost, B. Monaco, SiO_x and SiO_xCzHw mono-and multi-layer deposits for improved polymer oxygen and water vapor barrier properties, *J. Memb. Sci.* 500 (2016) 245–254.
- [133] F. Bosc, J. Sanchez, V. Rouessac, J. Durand, Sorption and permeation characteristics of hybrid organosilicon thin films deposited by PECVD, *Sep. Purif. Technol.* 32 (2003) 371–376.
- [134] V. Rouessac, P. Tuluc, J. Durand, Composite plasma-polymerized organosiloxane-based material for hydrocarbon vapor selectivity, *J. Memb. Sci.* 230 (2004) 49–59.
- [135] N. Andreeva, T. Ishizaki, P. Baroch, N. Saito, High sensitive detection of volatile organic compounds using superhydrophobic quartz crystal microbalance, *Sensors Actuators B Chem.* 164 (2012) 15–21.

- [136] P. Hohenberg, W. Kohn, Inhomogeneous electron gas, *Phys. Rev.* 136 (1964) B864.
- [137] W. Kohn, L.J. Sham, Self-consistent equations including exchange and correlation effects, *Phys. Rev.* 140 (1965) A1133.
- [138] J.P. Perdew, K. Burke, M. Ernzerhof, Generalized gradient approximation made simple, *Phys. Rev. Lett.* 77 (1996) 3865.
- [139] A. Gavrielides, T. Duguet, J. Esvan, C. Lacaze-Dufaure, P.S. Bagus, A poly-epoxy surface explored by Hartree-Fock Δ SCF simulations of C1s XPS spectra, *J. Chem. Phys.* 145 (2016) 74703.
- [140] T. Duguet, A. Gavrielides, J. Esvan, T. Mineva, C. Lacaze-Dufaure, DFT simulation of XPS reveals Cu/epoxy polymer interfacial bonding, *J. Phys. Chem. C.* 123 (2019) 30917–30925.
- [141] P.S. Bagus, E.S. Ilton, C.J. Nelin, The interpretation of XPS spectra: Insights into materials properties, *Surf. Sci. Rep.* 68 (2013) 273–304.
- [142] K. Anand, T. Duguet, J. Esvan, C. Lacaze-Dufaure, Chemical Interactions at the Al/Poly-Epoxy Interface Rationalized by DFT Calculations and a Comparative XPS Analysis, *ACS Appl. Mater. Interfaces.* 12 (2020) 57649–57665.
- [143] M. Giesbers, A.T.M. Marcelis, H. Zuilhof, Simulation of XPS C1s spectra of organic monolayers by quantum chemical methods, *Langmuir.* 29 (2013) 4782–4788.
- [144] M. Smith, L. Scudiero, J. Espinal, J.-S. McEwen, M. Garcia-Perez, Improving the deconvolution and interpretation of XPS spectra from chars by ab initio calculations, *Carbon N. Y.* 110 (2016) 155–171.
- [145] T. Duguet, C. Bessaguet, M. Aufray, J. Esvan, C. Charvillat, C. Vahlas, C. Lacaze-Dufaure, Toward a computational and experimental model of a poly-epoxy surface, *Appl. Surf. Sci.* 324 (2015) 605–611.
- [146] T. Otsuka, K. Endo, M. Suhara, D.P. Chong, Theoretical X-ray photoelectron spectra of polymers by deMon DFT calculations using the model dimers, *J. Mol. Struct.* 522 (2000) 47–60.
- [147] W. Motozaki, T. Otsuka, K. Endo, D.P. Chong, Electron binding energies of Si 2p and S 2p for Si- and S-containing substances by DFT calculations using the model molecules, *Polym. J.* 36 (2004) 600–606.
- [148] M. Haacké, R. Coustel, V. Rouessac, S. Roualdès, A. Julbe, Microwave PECVD silicon carbonitride thin films: A FTIR and ellipsoporosimetry study, *Plasma Process. Polym.* 13 (2016) 258–265.
- [149] A. Gavrielides, Modelling the DGEBA-EDA poly-epoxy reactivity towards copper experimental and numerical approach, (2017).
- [150] b M.R. Baklanov, K.P. Mogilnikov, V.G. Polovinkin, F.N. Dultsev, Determination of pore size distribution in thin films by ellipsometric porosimetry, *J. Vac. Sci. Technol. B Microelectron. Nanom. Struct. Process. Meas. Phenom.* 18 (2000) 1385–1391.
- [151] V. Rouessac, A. Van Der Lee, F. Bosc, J. Durand, A. Ayrat, Three characterization techniques coupled with adsorption for studying the nanoporosity of supported films and membranes, *Microporous Mesoporous Mater.* 111 (2008) 417–428.
- [152] F. Weigend, R. Ahlrichs, Balanced basis sets of split valence, triple zeta valence and quadruple zeta valence quality for H to Rn: Design and assessment of accuracy, *Phys. Chem. Chem. Phys.* 7 (2005) 3297–3305.
- [153] F. Weigend, Accurate Coulomb-fitting basis sets for H to Rn, *Phys. Chem. Chem. Phys.* 8 (2006) 1057–1065.
- [154] S. Grimme, Semiempirical GGA-type density functional constructed with a long-range dispersion correction, *J. Comput. Chem.* 27 (2006) 1787–1799.
- [155] S. Grimme, J. Antony, S. Ehrlich, H. Krieg, A consistent and accurate ab initio parametrization of density functional dispersion correction (DFT-D) for the 94 elements

- H-Pu, J. Chem. Phys. 132 (2010) 154104.
- [156] M. Frisch, G.W. Trucks, H.B. Schlegel, G.E. Scuseria, M.A. Robb, J.R. Cheeseman, G. Scalmani, V. Barone, B. Mennucci, G.A. ea Petersson, Gaussian~ 09 Revision D. 01, (2014).
- [157] E.D. Glendening, A.E. Reed, J.E. Carpenter, F. Weinhold, NBO Version 3.1, There Is No Corresp. Rec. This Ref. Sch. (1998).
- [158] G. Geudtner, P. Calaminici, J. Carmona-Espíndola, J.M. del Campo, V.D. Domínguez-Soria, R.F. Moreno, G.U. Gamboa, A. Gourso, A.M. Köster, J.U. Reveles, DeMon2k, Wiley Interdiscip. Rev. Comput. Mol. Sci. 2 (2012) 548–555.
- [159] P. Calaminici, F. Janetzko, A.M. Köster, R. Mejia-Olvera, B. Zuniga-Gutierrez, Density functional theory optimized basis sets for gradient corrected functionals: 3 d transition metal systems, J. Chem. Phys. 126 (2007) 44108.
- [160] T.H. Dunning Jr, Gaussian basis sets for use in correlated molecular calculations. I. The atoms boron through neon and hydrogen, J. Chem. Phys. 90 (1989) 1007–1023.
- [161] R. Flores-Moreno, R.J. Alvarez-Mendez, A. Vela, A.M. Köster, Half-numerical evaluation of pseudopotential integrals, J. Comput. Chem. 27 (2006) 1009–1019.
- [162] P. Bringmann, O. Rohr, F.J. Gammel, I. Jansen, Atmospheric pressure plasma deposition of adhesion promotion layers on aluminium, Plasma Process. Polym. 6 (2009) S496–S502.
- [163] C.E. Nwankire, G. Favaro, Q. Duong, D.P. Dowling, Enhancing the mechanical properties of superhydrophobic atmospheric pressure plasma deposited siloxane coatings, Plasma Process. Polym. 8 (2011) 305–315.
- [164] R. Förch, A.N. Chifen, A. Bousquet, H.L. Khor, M. Jungblut, L. Chu, Z. Zhang, I. Osey-Mensah, E. Sinner, W. Knoll, Recent and expected roles of plasma-polymerized films for biomedical applications, Chem. Vap. Depos. 13 (2007) 280–294.
- [165] R.P. Mota, D. Galvão, S.F. Durrant, M.A.B. De Moraes, S. de Oliveira Dantas, M. Cantão, HMDSO plasma polymerization and thin film optical properties, Thin Solid Films. 270 (1995) 109–113.
- [166] U. Lommatzsch, J. Ihde, Plasma polymerization of HMDSO with an atmospheric pressure plasma jet for corrosion protection of aluminum and low-adhesion surfaces, Plasma Process. Polym. 6 (2009) 642–648.
- [167] S.J. Kim, E. Song, K. Jo, T. Yun, M.-W. Moon, K.-R. Lee, Composite oxygen-barrier coating on a polypropylene food container, Thin Solid Films. 540 (2013) 112–117.
- [168] Y.-H. Kim, S.-K. Lee, H.J. Kim, Low-k Si–O–C–H composite films prepared by plasma-enhanced chemical vapor deposition using bis-trimethylsilylmethane precursor, J. Vac. Sci. Technol. A Vacuum, Surfaces, Film. 18 (2000) 1216–1219.
- [169] M. Lépinay, L. Broussous, C. Licitra, F. Bertin, V. Rouessac, A. Ayral, B. Coasne, Predicting adsorption on bare and modified silica surfaces, J. Phys. Chem. C. 119 (2015) 6009–6017.
- [170] E. Kedroňová, L. Zajíčková, D. Hegemann, M. Klíma, M. Michlíček, A. Manakhov, Plasma enhanced CVD of organosilicon thin films on electrospun polymer nanofibers, Plasma Process. Polym. 12 (2015) 1231–1243.
- [171] C. Chaiwong, P. Rachtanapun, S. Sarapirom, D. Boonyawan, Plasma polymerization of hexamethyldisiloxane: Investigation of the effect of carrier gas related to the film properties, Surf. Coatings Technol. 229 (2013) 12–17.
- [172] T. Brenner, K. Vissing, New insight into organosilicon plasma-enhanced chemical vapor deposition layers and their crosslinking behavior by calculating the degree of Si-networking, Plasma Process. Polym. (n.d.) e1900202 (2020).
- [173] M.A. Gilliam, S.A. Farhat, G.E. Garner, B.P. Stubbs, B.B. Peterson, Characterization of the deposition behavior and changes in bonding structures of hexamethyldisiloxane and

- decamethylcyclopentasiloxane atmospheric plasma-deposited films, *Plasma Process. Polym.* 16 (2019) e1900024. <https://doi.org/10.1002/ppap.201900024>.
- [174] A. Sonnenfeld, T.M. Tun, L. Zajíčková, K. V Kozlov, H.-E. Wagner, J.F. Behnke, R. Hippler, Deposition process based on organosilicon precursors in dielectric barrier discharges at atmospheric pressure—a comparison, *Plasma Polym.* 6 (2001) 237–266.
- [175] H. Nagasawa, T. Minamizawa, M. Kanezashi, T. Yoshioka, T. Tsuru, Microporous organosilica membranes for gas separation prepared via PECVD using different O/Si ratio precursors, *J. Memb. Sci.* 489 (2015) 11–19.
- [176] M.G.M. Van der Vis, R.J.M. Konings, A. Oskam, T.L. Snoeck, The vibrational spectra of gaseous and liquid tetraethoxysilane, *J. Mol. Struct.* 274 (1992) 47–57.
- [177] M.T. Tribble, N.L. Allinger, Conformational analysis—LXXXIII: Calculation of the structures and energies of silanes by the method of molecular mechanics, *Tetrahedron.* 28 (1972) 2147–2156.
- [178] G. Beamson, D. Briggs, The scienta ESCA 300 database, *High Resolut. XPS Org. Polym.* (1992).
- [179] A. Allouche, Gabedit—A graphical user interface for computational chemistry softwares, *J. Comput. Chem.* 32 (2011) 174–182.
- [180] M.J. Barrow, E.A. V Ebsworth, M.M. Harding, The crystal and molecular structures of disiloxane (at 108 K) and hexamethyldisiloxane (at 148 K), *Acta Crystallogr. Sect. B Struct. Crystallogr. Cryst. Chem.* 35 (1979) 2093–2099.
- [181] H. Steinfink, B. Post, I. Fankuchen, The crystal structure of octamethyl cyclotetrasiloxane, *Acta Crystallogr.* 8 (1955) 420–424.
- [182] H.K. Son, S. Sivakumar, M.J. Rood, B.J. Kim, Electrothermal adsorption and desorption of volatile organic compounds on activated carbon fiber cloth, *J. Hazard. Mater.* 301 (2016) 27–34.
- [183] C. Megias-Sayago, I. Lara-Ibeas, Q. Wang, S. Le Calve, B. Louis, Volatile organic compounds (VOCs) removal capacity of ZSM-5 zeolite adsorbents for near real-time BTEX detection, *J. Environ. Chem. Eng.* 8 (2020) 103724.
- [184] J. Choma, M. Marszewski, L. Osuchowski, J. Jagiello, A. Dziura, M. Jaroniec, Adsorption properties of activated carbons prepared from waste CDs and DVDs, *ACS Sustain. Chem. Eng.* 3 (2015) 733–742.
- [185] L. Zhang, Y. Peng, J. Zhang, L. Chen, X. Meng, F.-S. Xiao, Adsorptive and catalytic properties in the removal of volatile organic compounds over zeolite-based materials, *Chinese J. Catal.* 37 (2016) 800–809.
- [186] B. Dragoi, V. Rakic, E. Dumitriu, A. Auroux, Adsorption of organic pollutants over microporous solids investigated by microcalorimetry techniques, *J. Therm. Anal. Calorim.* 99 (2010) 733–740.
- [187] K.-J. Kim, H.-G. Ahn, The effect of pore structure of zeolite on the adsorption of VOCs and their desorption properties by microwave heating, *Microporous Mesoporous Mater.* 152 (2012) 78–83.
- [188] A.-F. Cosseron, T.J. Daou, L. Tzanis, H. Nouali, I. Deroche, B. Coasne, V. Tchamber, Adsorption of volatile organic compounds in pure silica CHA,* BEA, MFI and STT-type zeolites, *Microporous Mesoporous Mater.* 173 (2013) 147–154.
- [189] T. Kawai, K. Tsutsumi, Evaluation of hydrophilic-hydrophobic character of zeolites by measurements of their immersional heats in water, *Colloid Polym. Sci.* 270 (1992) 711–715.
- [190] V. Balouria, A. Kumar, S. Samanta, A. Singh, A.K. Debnath, A. Mahajan, R.K. Bedi, D.K. Aswal, S.K. Gupta, Nano-crystalline Fe₂O₃ thin films for ppm level detection of H₂S, *Sensors Actuators B Chem.* 181 (2013) 471–478.
- [191] Z. Zhu, C.-T. Kao, R.-J. Wu, A highly sensitive ethanol sensor based on Ag@ TiO₂

- nanoparticles at room temperature, *Appl. Surf. Sci.* 320 (2014) 348–355.
- [192] J. Gong, Q. Chen, M.-R. Lian, N.-C. Liu, R.G. Stevenson, F. Adami, Micromachined nanocrystalline silver doped SnO₂ H₂S sensor, *Sensors Actuators B Chem.* 114 (2006) 32–39.
- [193] J.W. Grate, S.N. Kaganove, V.R. Bhethanabotla, Comparisons of polymer/gas partition coefficients calculated from responses of thickness shear mode and surface acoustic wave vapor sensors, *Anal. Chem.* 70 (1998) 199–203.
- [194] S.J. Patrash, E.T. Zellers, Characterization of polymeric surface acoustic wave sensor coatings and semiempirical models of sensor responses to organic vapors, *Anal. Chem.* 65 (1993) 2055–2066.
- [195] A. Hierlemann, A.J. Ricco, K. Bodenhöfer, A. Dominik, W. Göpel, Conferring selectivity to chemical sensors via polymer side-chain selection: thermodynamics of vapor sorption by a set of polysiloxanes on thickness-shear mode resonators, *Anal. Chem.* 72 (2000) 3696–3708.
- [196] C. Park, Y. Han, K.-I. Joo, Y.W. Lee, S.-W. Kang, H.-R. Kim, Optical detection of volatile organic compounds using selective tensile effects of a polymer-coated fiber Bragg grating, *Opt. Express.* 18 (2010) 24753–24761.
- [197] W. Ogieglo, H. van der Werf, K. Tempelman, H. Wormeester, M. Wessling, A. Nijmeijer, N.E. Benes, n-Hexane induced swelling of thin PDMS films under non-equilibrium nanofiltration permeation conditions, resolved by spectroscopic ellipsometry, *J. Memb. Sci.* 437 (2013) 313–323.
- [198] V. Jousseume, C. Yeromonahos, J. El Sabahy, B. Altemus, C. Ladner, K. Benedetto, E. Ollier, J. Faguet, Filament Assisted Chemical Vapor Deposited organosilicate as chemical layer for nanometric hydrocarbon gas sensors, *Sensors Actuators B Chem.* 271 (2018) 271–279.
- [199] G. Dakroub, T. Duguet, J. Esvan, C. Lacaze-Dufaure, S. Roualdes, V. Rouessac, Comparative study of bulk and surface compositions of plasma polymerized organosilicon thin films, *Surfaces and Interfaces.* (2021) 101256.
- [200] L.M. Han, J.-S. Pan, S.-M. Chen, N. Balasubramanian, J. Shi, L.S. Wong, P.D. Foo, Characterization of carbon-doped SiO₂ low k thin films: Preparation by plasma-enhanced chemical vapor deposition from tetramethylsilane, *J. Electrochem. Soc.* 148 (2001) F148.
- [201] D. Shamiryan, K. Weidner, W.D. Gray, M.R. Baklanov, S. Vanhaelemeersch, K. Maex, Comparative study of PECVD SiOCH low-k films obtained at different deposition conditions, *Microelectron. Eng.* 64 (2002) 361–366.
- [202] Z. Yang, Q. Li, R. Hua, M.R. Gray, K.C. Chou, Competitive adsorption of toluene and n-alkanes at binary solution/silica interfaces, *J. Phys. Chem. C.* 113 (2009) 20355–20359.
- [203] R.A. Rinsky, A.B. Smith, R. Hornung, T.G. Filloon, R.J. Young, A.H. Okun, P.J. Landrigan, Benzene and leukemia, *N. Engl. J. Med.* 316 (1987) 1044–1050.
- [204] Health Canada. 2014a. Guideline technical document. Guidelines for Canadian drinking water quality: guideline technical document — toluene, ethylbenzene and xylenes. Water and Air Quality Bureau, Healthy Environments and Consumer Safety Branch, Health Can, (n.d.). <https://www.canada.ca/content/dam/canada/health-canada/migration/healthy-canadians/publications/healthy-living-vie-saine/water-toluene-eau/alt/water-toluene-eau-eng.pdf>.
- [205] C. Massie, G. Stewart, G. McGregor, J.R. Gilchrist, Design of a portable optical sensor for methane gas detection, *Sensors Actuators B Chem.* 113 (2006) 830–836.
- [206] X. Liu, S. Cheng, H. Liu, S. Hu, D. Zhang, H. Ning, A survey on gas sensing technology, *Sensors.* 12 (2012) 9635–9665.

- [207] S. Khan, S. Le Calvé, D. Newport, A review of optical interferometry techniques for VOC detection, *Sensors Actuators A Phys.* 302 (2020) 111782.
- [208] F. Ren, L. Gao, Y. Yuan, Y. Zhang, A. Alqrni, O.M. Al-Dossary, J. Xu, Enhanced BTEX gas-sensing performance of CuO/SnO₂ composite, *Sensors Actuators B Chem.* 223 (2016) 914–920.
- [209] N. Yamazoe, K. Shimano, New perspectives of gas sensor technology, *Sensors Actuators B Chem.* 138 (2009) 100–107.
- [210] L.R. Khot, S. Panigrahi, D. Lin, Development and evaluation of piezoelectric-polymer thin film sensors for low concentration detection of volatile organic compounds related to food safety applications, *Sensors Actuators B Chem.* 153 (2011) 1–10. <https://doi.org/https://doi.org/10.1016/j.snb.2010.05.043>.
- [211] J. Huang, Y. Jiang, X. Du, J. Bi, A new siloxane polymer for chemical vapor sensor, *Sensors Actuators B Chem.* 146 (2010) 388–394. <https://doi.org/https://doi.org/10.1016/j.snb.2010.02.010>.
- [212] Y. Acikbas, R. Capan, M. Erdogan, F. Yukruk, Thin film characterization and vapor sensing properties of a novel perylenediimide material, *Sensors Actuators B Chem.* 160 (2011) 65–71. <https://doi.org/https://doi.org/10.1016/j.snb.2011.07.013>.
- [213] G. Camino, S.M. Lomakin, M. Lazzari, Polydimethylsiloxane thermal degradation Part 1. Kinetic aspects, *Polymer (Guildf)*. 42 (2001) 2395–2402.
- [214] A. Grill, D.A. Neumayer, Structure of low dielectric constant to extreme low dielectric constant SiCOH films: Fourier transform infrared spectroscopy characterization, *J. Appl. Phys.* 94 (2003) 6697–6707.
- [215] A.D. Becke, Density-functional exchange-energy approximation with correct asymptotic behavior, *Phys. Rev. A*. 38 (1988) 3098.
- [216] C. Lee, W. Yang, R.G. Parr, Development of the Colle-Salvetti correlation-energy formula into a functional of the electron density, *Phys. Rev. B*. 37 (1988) 785.

Volatile organic compounds (VOCs) mainly BTEX (Benzene, Toluene, Ethylbenzene, Xylenes) vapors emissions is one of the most serious problems due to their high toxicity to human health and environment as well as their contribution in air pollution. One of the well-known solutions for gas detection is the gravimetric sensing technique. However, this technique requires a functionalized thin layer to select the analytes.

The aim of this work is to study and understand the sorption mechanism of BTEX vapours into plasma polymerized organosilicon thin films, on the surface (adsorption) and inside the material bulk (absorption, diffusion) for gas sensing applications.

First, a large panel of organosilicon thin films were prepared by microwave Plasma Enhanced Chemical Vapor Deposition (MW-PECVD) under various plasma conditions, using hexamethyldisiloxane (HMDSO) as precursor. A fine investigation of the chemical composition was carried out in order to compare the bulk and surface compositions of organosilicon films prepared by PECVD using a methodology that combines experiments, chemical characterization and DFT calculations. With these aims, organosilicon films were characterized by Fourier transform-infrared (FTIR) and ^{29}Si Solid-state NMR spectroscopies to figure out the bulk composition. X-ray photoelectron spectroscopy combined with DFT calculations led us to determine the surface composition of PECVD organosilicon films. Furthermore other characterization techniques such as ellipsometry, water contact angle (WCA), XRR, EDX were performed in order to refine the investigation of the structure and physical properties.

Second, the sorption of VOCs and BTEX gases was studied by Quartz Crystal Microbalance (QCM) and ellipsometry coupled with vapor sorption. The effect of the plasma parameters, such as plasma power (W) and the HMDSO flow rate (F), on the sorption of BTEX gases was studied and the ideal PP-HMDSO deposit with the best performance towards BTEX was identified.

Finally, a thermal treatment on the optimized deposit was carried out in order to improve its response towards the detected gases. Accordingly, different characterization techniques were carried out on the annealed deposit such as FTIR, EDX, ellipsometry. In addition, the affinity of the deposit after treatment towards VOCs was analyzed and compared to the non-annealed one.

As main striking results, this work has allowed to figure out the ideal plasma conditions to elaborate organosilicon films for BTEX sensors applications. In optimized plasma conditions and after a thermal post-treatment, a good BTEX sensitivity could be achieved with a good selectivity between BTEX and ethanol.

Les composés organiques volatils (COV) en particulier les BTEX (Benzène, Toluène, Ethylbenzène, Xylènes), vapeurs très toxiques pour l'homme et l'environnement, doivent être détectées et éliminées. L'une des solutions bien connues pour la détection des gaz est la technique gravimétrique. Cependant, cette technique nécessite une couche mince fonctionnalisée pour sélectionner les analytes.

L'objectif de ce travail est d'étudier et de comprendre le mécanisme de sorption des vapeurs de BTEX dans des films minces d'organosiliciés polymérisés par plasma, en surface (adsorption) et à l'intérieur du matériau (absorption, diffusion) pour des applications de détection de gaz.

Tout d'abord, une large gamme de films minces d'organosiliciés a été préparée par dépôt chimique en phase vapeur assisté par plasma en décharge micro-ondes (MW-PECVD) dans diverses conditions de plasma, en utilisant l'hexaméthylsiloxane (HMDSO) comme précurseur. Une étude fine de la composition chimique a été réalisée afin de comparer les compositions du massif et de la surface des films en utilisant une méthodologie qui combine expériences, caractérisations chimiques et calculs DFT. Dans ce but, les films d'organosiliciés PECVD (PP-HMDSO) ont été caractérisés par FTIR et par RMN ^{29}Si du solide pour déterminer la composition globale. L'analyse de la surface par XPS combinée à des calculs DFT a permis de déterminer la composition de surface des films. De plus, d'autres techniques de caractérisation telles que l'ellipsométrie spectroscopique, l'angle de contact à l'eau (WCA) et les analyses XRR et EDX ont été réalisées afin d'affiner l'étude de la structure et des propriétés physiques.

Dans un second temps, la sorption des vapeurs de COV et BTEX a été étudiée par microgravimétrie par cristal de quartz (QCM) et ellipsométrie spectroscopique couplée à la sorption de vapeur. L'effet des paramètres du plasma, tels que la puissance du plasma (W) et le débit d'HMDSO (F), sur la sorption des BTEX a été étudié et le dépôt de PP-HMDSO ayant les meilleures performances vis-à-vis du BTEX a été identifié.

Enfin, un traitement thermique optimal a été trouvé afin d'améliorer la réponse du matériau précédemment identifié vis-à-vis des gaz détectés. Ainsi, les techniques FTIR, EDX et ellipsométrie spectroscopique ont été utilisées pour caractériser le dépôt recuit. Ces analyses du matériau ont été complétées par l'analyse de l'affinité du dépôt avant et après traitement thermique vis-à-vis des COV.

Comme principaux résultats marquants, ce travail nous a permis de déterminer les conditions optimales de plasma pour élaborer des films d'organosiliciés pour détecter les BTEX. Dans des conditions de plasma optimales après post-traitement thermique, une bonne sensibilité aux BTEX a été obtenue et une sélectivité remarquable entre les BTEX et d'autres COV a été mise en évidence.